Ph.D. Program in Civil, Chemical and Environmental Engineering

Curriculum in Structural and Geotechnical Engineering, Mechanics and Materials

Department of Civil, Chemical and Environmental Engineering
Polytechnic School, University of Genoa, Italy.

Full-scale monitoring of the wind-induced response of vertical slender structures, with fixed and rotating masses

Andrea Orlando

FULL-SCALE MONITORING OF THE WIND-INDUCED RESPONSE OF VERTICAL SLENDER STRUCTURES, WITH FIXED AND ROTATING MASSES

BY

ANDREA ORLANDO

Dissertation discussed in partial fulfillment of
the requirements for the Degree of

DOCTOR OF PHILOSOPHY

Civil, Chemical and Environmental Engineering
curriculum in Structural and Geotechnical Engineering Mechanics and Materials,
Department of Civil, Chemical and Environmental Engineering, University of Genoa, Italy

July, 2021

Adviser(s):

Luisa Carlotta Pagnini – Department of Civil, Chemical and Environmental Engineering, University of Genoa, Italy

Maria Pia Repetto – Department of Civil, Chemical and Environmental Engineering, University of Genoa, Italy

External Reviewers:

Luca Caracoglia – Department of Civil and Environmental Engineering, Northeastern University, Boston, Massachusetts, USA

Francesco Castellani – Department of Engineering, University of Perugia, Italy

Ph.D. program in Civil, Chemical and Environmental Engineering

Curriculum in Structural and Geotechnical Engineering, Mechanics and Materials

Cycle XXXIII

Index

1. Introduction

Slender structures and structural elements are strongly sensitive to wind action that induces vibrations in the longitudinal (along-wind), lateral (cross-wind) and torsional directions. The atmospheric turbulence causes forced excitations, whereas aeroelastic phenomena, including vortex shedding and galloping, can overlap gust actions for certain values of the wind velocity. Towers, chimneys and harbor cranes constitute relevant examples where wind is the leading design loading due to high slenderness and aerodynamic peculiarities (Figure 1.1).

Literature provides several methods for the evaluation of wind loading and relevant structural response. The main calculation models are then included in current codes and standards (e.g., CNR, 2018, EN, 1991-1-4, 2005) for the most common structural types.

The investigation of the wind-induced response of structures started in the 1960s thanks to the pioneering contribution of Davenport (1961, 1964, 1967), who developed a calculation method to evaluate the along-wind displacement of vertical cantilever structures vibrating on their first natural mode.

In successive formulations, efforts have been directed towards the generalization of the method developed by Davenport, in order to define a univocal calculation procedure to take into account all the possible wind-induced excitations.

From one hand, several methods were developed for the estimation of structural effects different from displacements (ESDU, 1976, ECCS, 1978, Kasperski, 1992, Holmes, 1994). From the other, the concepts introduced by Davenport were extended from the along-wind response to the cross-wind and torsional responses (Piccardo and Solari, 1998, 2000).

The junction point between 3-D response and effect calculation was introduced by Piccardo and Solari (2002). This method was initially limited to cantilever vertical slender structures (Piccardo and Solari, 2002, Repetto and Solari, 2004) and then extended to general slender structures, variously inclined and constrained, also taking into account aeroelastic effects (Pagnini and Piccardo, 2017).

In addition to wind-induced response, several methods have been developed over the years to deal with wind-induced fatigue loading (Wirsching and Light, 1980, Holmes, 2002, Xu et al., 2009, Jang et al., 2015). In particular, Repetto and Solari (2009, 2012) developed an analytical closed-form solution to evaluate the wind-induced fatigue damage suitable for engineering verifications.

However, despite the calculation methods developed over the years seem to cover every aspect of wind action on standard slender structures, the practical application of such models involves uncertainties that can strongly affect the final calculation. Indeed, the implementation of these methods in the design stage requires the knowledge of several parameters characterizing the structure, whose evaluation is very delicate and awkward.

For example, as far as the aerodynamic parameters are concerned, the structural variety is so wide that the available information can be scanty even for the most common structural types, despite the abundance of extensive experimental campaigns.

With the regard to the modal parameters of structures, while frequencies and mode shapes usually can be predicted with a good approximation from analytical expressions (for the simplest structural types) or numerical simulations, the singularity of damping and the sensitivity of its experimental estimations spread uncertainties in the generalization of the values available in literature.

Figure 1.1. Examples of slender structures: chimneys, harbor cranes and wind turbines.

All the described parameters, besides affecting the classical gust buffeting, are also fundamental to predict possible non-linear aeroelastic effects like galloping or vortex shedding, which can recur in slender and lightweight structures.

On the other hand, for some complex structural types there are no specific calculation models. The design of wind turbines, for example, is carried out using numerical methods that combine finite element modeling and CFD analysis. Small wind turbines, given the limited dimensions of the rotor and the supporting shaft, are usually designed with simplified methods, omitting an appropriate survey of the complex dynamic phenomena involved and the turbulent action of the wind. In addition, the experimental studies are focused mainly on the structural performance of the blades, disregarding the effects of the rotation on the supporting tower.

As a consequence, many structural collapses of slender structures are observed (Caracoglia and Jones, 2006, Repetto and Pagnini, 2017, Ma et al., 2019). Experimentation is therefore a fundamental tool for the application, the validation and the development of the models. The use of in-field measurements is a valuable resource for many reasons: from one hand, full-scale data supply direct information on structural response that can be used as input in the calculation methods; from the other, they represent a benchmark against which loading and response models can be compared and calibrated.

Several monitoring campaigns of structures have been launched to obtain robust full-scale measurements of the structural behavior under different loading conditions (Tamura et al., 1996, Satake et al., 2003, Li et al., 2004, 2008, Kijewski-Correa et al., 2006, 2013). However, it is timely to highlight that documented long-term monitoring activities are almost entirely dedicated to high-rise buildings. Structures of minor importance, like towers and wind turbines, are often monitored by the stakeholders; however, results from such activities are rarely reported.

The wind engineering research group at the University of Genoa has already carried out monitoring activities of slender structures. In the past years, they have concerned steel tubular towers in order to estimate their structural damping and frequency (Pagnini and Solari, 2001). A monitoring campaign over small size wind turbines started in 2015 and it is still under way. In a first phase, the wind field and the energy production of two wind turbines with the same power (20kW) but different technology (vertical and horizontal axis) were studied (Pagnini et al., 2015). Subsequently, the monitoring equipment has been enhanced with accelerometers and strain gauges for the investigation of the structural behavior (Pagnini et al., 2018).

Starting from these premises, the present work develops and applies a comprehensive structural-monitoring procedure tailored for the validation and investigation in full-scale of the wind-induced response of vertical slender structures, with fixed and rotating masses.

The main goals of the thesis are here summarized:

a) development of a systematic procedure to handle the long-term monitoring of vertical slender structures;
b) design and realization of the monitoring system of a vertical slender structure;
c) experimental investigation of the structural properties necessary for the calculation of wind action and wind effects;
d) full-scale validation of the current calculation models of wind-induced response for slender structures with fixed masses;
e) investigation of the dynamic behavior of slender structures with rotating masses to develop simplified models of the structural response.

Starting from a detailed review of the state of the art in the field of structural monitoring, the present work operates a synthesis of the current monitoring practices to develop a systematic and coded structural monitoring procedure suitable for the investigation of wind effects on vertical slender structures (point a).

The procedure finds application in two monitoring campaigns launched by the Wind Engineering group at the University of Genoa. The investigation of slender structures with fixed masses is accomplished by monitoring a light tower installed in the harbor of La Spezia, Northern Italy (Figure 1.2 a). Due to its structural simplicity, this structure is very attractive for a comparison between full-scale measurements and analytical predictions. The preliminary study, the design and the realization of the monitoring system of the tower has been carried out completely during the Ph.D. activity, and it is included in the present work (point b).

The experimental study of slender structures with rotating masses is pursued by exploiting the outcomes from the monitoring of the small wind turbine in the harbor of Savona, Northern Italy (Figure 1.2 b). In this case, the developed monitoring procedure has been applied from the post-processing phase.

The identification from experimental surveys of the parameters describing the structural behavior represents a very important topic, both for the definition of parameters involved in the calculation models (point c), and for the generalization of the results to structures of the same typology. In this respect, to address the lacking of information about polygonal cross-sections, which are typical of poles and supporting towers, an extensive experimental campaign has been undertaken in the wind tunnel facility of the University of Genoa.

Outcomes of the monitoring activity are used to assess the capability of simplified calculation models from literature of predicting the actual wind-induced response of vertical slender structures with fixed masses, and to evaluate the propagation of uncertainties due to the parameters involved in the calculation (point d). In particular, a reference calculation model providing the wind-induced response of poles and monotubular towers is chosen (Solari and Pagnini, 1999) and devoted to comparisons with full-scale measurements from both the light tower and the wind turbine in parked conditions.

Figure 1.2. The monitored structures: light tower in La Spezia (a), small wind turbine in Savona (b).

Full-scale data from the operative wind turbine are used to investigate the dynamic behavior of slender structures with rotating masses, with the perspective of developing simplified models that take into account the dynamic interaction of fixed and rotating parts (point e). With respect to small wind turbines, experimentation constitutes a fundamental premise to generalize the calculation models of monotubular towers to the considered typology. With regard to the rotating wind turbine, particular attention has been devoted to fatigue calculation, which becomes a dominant design loading for structures subjected to additional cyclic excitation besides the wind.

The Ph.D. thesis is divided in six chapters. After this introduction, which provides an overview of the research activity, Chapter 2 describes the development of the systematic structural monitoring procedure. All the main aspects of the monitoring practice are discussed, regarding the number, location and type of the sensors, the acquisition and the transmission of the full-scale data, as well as the management of the experimental database by following an encoded scheme. In addition, it highlights a number of issues typical of the monitoring activity that are not addressed in literature, providing inspiration to solve them.

After a brief literature review, Chapter 3 introduces the analytical calculation model that is used in the present work to evaluate the wind-induced response of vertical slender structures. The modelling of wind loading and wind-induced effects is described in detail, as well as the role of the main parameters involved in the calculation.

Chapter 4 describes the experimental activity on the light tower in La Spezia. First, it reports the design and the construction of the monitoring system. Then, it deals with the investigation of the parameters needed for the calculation of the wind-induced response. In this respect, the wind tunnel test campaign plays a major role in the chapter for the significance of the results, despite being functional to the calculation. The dynamic identification of the tower is accomplished by intersecting experimental techniques with outcomes of a finite element model. Finally, the calculation model is validated in full-scale and relevant uncertainties are quantified.

Chapter 5 is dedicated to the monitoring of the small wind turbine in Savona. In this case, both the monitoring chain and the input parameters were already defined. The calculation model is applied to assess its suitability for parked wind turbines. Then, the effects of rotation on the modal properties are investigated, with the final aim (that remains as a perspective of the present work) of generalizing

the calculation model to rotating-masses structures. The last part of the chapter deals with the fatigue assessment of the turbine. In particular, the study addresses issues related to stationary and non-stationary excitations, which are rarely dealt in literature on the basis of full-scale data.

Lastly, Chapter 6 draws the main conclusions of the work and the perspectives for further research.

References

Caracoglia, L., Jones, N.P. (2006). Wind-induced failures of highway light poles during winter storms, ASME Pressure Vessels and Piping Division (Publication) PVP 9, 197-206.

CNR (2018). Guide for the assessment of wind actions and effects on structures - CNR-DT 207 R1/2018. Roma: National Research Council of Italy.

Davenport, A.G. (1961). The application of statistical concepts to the wind loading of structures. Proc. Inst. Civ. Eng. London 19, 449–472.

Davenport, A.G. (1964). Note on the distribution of the largest value of a random function with application to gust loading. Proc. Inst. Civ. Eng. London 24, 187–196.

Davenport A.G. (1967). Gust loading factors. J. Struct. Div. ASCE 93, 11–34.

EN 1991-1-4, 2005. Eurocode 1: Actions on Structures – Part 1.4: General Actions – Wind Actions. CEN, European Commitee for Standardization, Brussels, Belgium.

ESDU 76001 (1976). The response of flexible structures to atmospheric turbulence. London, UK.

ECCS (1978). Recommendations for the calculation of wind effects on buildings and structures. Brussels, Belgium.

Holmes, J.D. (1996). Along-wind response of lattice towers—III. Effective load distributions. Eng. Struct. 18, 489–494.

Holmes, J.D. (2002). Fatigue under along-wind loading - closed-form solutions. Eng. Struct. 24, 109–114.

Jang, Y.J., Choi, C.W., Lee, J.H., Kang, K.W. (2015). Development of fatigue life prediction method and effect of 10-minute mean wind speed distribution on fatigue life of small wind turbine composite blade. Renew. Energy 79, 187–98.

Kasperski, M. (1992). Extreme wind load distributions for linear and nonlinear design. Eng. Struct. 14, 27–34.

Kijewski-Correa, T., et al. (2006). Validating the wind-induced response of tall buildings: A synopsis of the Chicago full-scale monitoring program. J. Struct. Eng. 132(10), 1509–1523.

Kijewski-Correa, T., Kwon, D.K., Kareem, A., Bentz, A., Guo, Y., Bobby, S., Abdelrazaq, A. (2013). SmartSync: An integrated real-time structural health monitoring and structural identification system for tall buildings. J. Struct. Eng. 139(10), 1675-1687.

Li, Q. S., Xiao, Y. Q., Wong, C. K., and Jeary, A. P. (2004). Field measurements of typhoon effects on a super tall building. Eng. Struct. 26(2), 233–244.

Li, Q.S., Xiao, Y.Q., Wu, J.R., Fu, J.Y, Li, Z.N. (2008). Typhoon effects on super tall buildings. J. Sound Vib., 313, 581–602.

Ma, Y., Martinez-Vazquez, P., Baniotopoulos, C. Wind turbine tower collapse cases: a historical overview. Proceedings of the Institution of Civil Engineers – Structures and Buildings, 2018.

Pagnini L.C., Solari G. (2001). Damping measurements of steel poles and tubular towers. Eng. Struct. 23, 1085–1095.

Pagnini L.C., Burlando M., Repetto M.P. (2015). Experimental power curve of small-size wind turbines in turbulent urban environment. Appl. Energy 154, 112-121.

Pagnini, L.C., Piccardo, G. (2017). A generalized gust factor technique for evaluating the wind–induced response of aeroelastic structures sensitive to vortex-induced vibrations. J. Fluids Struct. 70, 181-200.

Pagnini, L.C., Piccardo, G., Repetto, M.P. (2018). Full-scale behavior of a small size vertical axis wind turbine. Renew Energy 127, 41–55.

Piccardo, G., Solari, G. (1998). Closed form prediction of 3-D wind-excited response of slender structures. J. Wind Eng. Ind. Aerodyn. 74–76, 697–708.

Piccardo, G., Solari, G. (2000). 3-D wind-excited response of slender structures: closed form solution. J. Struct. Eng. ASCE 126, 936–943.

Piccardo, G., Solari, G. (2002). 3-D gust effect factor for slender vertical structures. Prob. Eng. Mech. 17, 143–155.

Repetto, M.P., Solari, G. (2004). Equivalent static wind actions on vertical structures. J. Wind Eng. Ind. Aerodyn 92, 335-357.

Repetto, M.P., Solari, G. (2009). Closed form solution of the alongwind-induced fatigue damage to structures. Eng. Struct. 31, 2414–2425.

Repetto, M.P., Solari, G. (2012). Closed form prediction of the alongwind-induced fatigue of structures. J. Struct. Eng, ASCE 2012, 138(9), 1149–60.

Repetto, M.P., Pagnini, L.C. (2017). Fatigue life assessment of a vertical axis wind turbine. Proc. Int. Conf. on Wind Energy Harvesting, Winercost17, Coimbra, 2017.

Satake, N., Suda, K., Arakawa, T., Sasaki, A., Tamura, Y. (2003). Damping evaluation using full-scale data of buildings in Japan. J. Struct. Eng. 129(4), 470–477.

Solari, G., Pagnini, L.C., 1999. Gust buffeting and aeroelastic behaviour of poles and monotubolar towers. J. of Fluids Struct. 13(7-8), 877-905.

Tamura, Y., Suganuma, S. (1996). Evaluation of amplitude-dependent damping and natural frequency of building during strong winds. J. Wind Eng. Ind. Aerodyn. 59, 115-130.

Wirsching, P.H., Light, M.C. (1980). Fatigue under wide band random stresses. J. Struct. Div. ASCE 1980, 106, 1593–607.

Xu, Y.L., Liu, T.T., Zhang, W.S. (2009) Buffeting-induced fatigue damage assessment of a long suspension bridge. Int. J. Fatigue 31, 575–86.

2. Full-scale monitoring of vertical slender structures

2.1 Introduction

Nowadays, structural monitoring is an essential tool in the field of structural engineering. However, even if the temporary instrumentation of structures and structural elements for the investigation of the dynamic behavior or for the identification of the dynamic properties is a consolidated practice, the birth of structural monitoring, intended as the science that regulates long-term measurement campaigns on structures, dates back to the second half of the 90s. In that period, with growing need to assure life safety and rapid reoccupation in regions of high seismicity, full-scale monitoring applications on buildings began to flourish in the western United States as part of coordinated strong motion instrumentation programs. This diffusion of long-term measurement campaigns became favorable for the regulation of the principles that drive the monitoring of structures. Thanks also to the technological improvement of transducers and data acquisition hardware, structural monitoring has received increasing attention, especially in the wind engineering field.

However, long-term full-scale measurements can find several different applications, and not all of them have been systematically addressed by research. In the last 25 years the relevant literature has almost entirely dealt with Structural Health Monitoring (SHM), which is the set of techniques that enable to identify a structural damage from differences over time of the dynamic response; see Doebling et al. (1996), Farrar et al. (2001), Sohn et al. (2003), Brownjohn (2007) and Lynch (2007) among others.

When the objective of the long-term monitoring is not to assess the safety of a structure or a component, the research state of the art becomes lacking and fragmented. Some papers have pursued the identification of the structural dynamic parameters from long-term measurements, both for the enhancement of a damping database and for the investigation of the amplitude-dependency of such parameters. Most of the studies have regarded tall buildings (Tamura et al., 1996, Satake et al., 2003, Bashor et al., 2005, Li et al., 2020). With regard to slender structures, the study by Carassale and Percivale (2008) of a light pole and the study by Pagnini et al. (2017) of a small wind turbine seem to be isolated cases in literature. A second line of research has aimed to further the understanding of the dynamic behavior of complex structures under different wind / operative conditions (Li et al., 1998, Pagnini et al., 2017). A third line, limited to high-rise buildings, has tried to validate structural performance and various design practices in full scale (Li et al. 2004, 2008, Kijewski-Correa et al., 2006).

It is timely to highlight the advancements proposed by the research group of the Notre Dame University, which in 2002 initiated the Chicago Full-Scale Monitoring Program to permit the response of three tall buildings in Chicago to be compared against design predictions, including their levels of inherent damping. Throughout the activity of the Program, they developed a comprehensive full-scale validation procedure tailored for the wind design practice of tall buildings. The rich literary production (Kijewski-Correa et al., 2006a, 2006b, 2013, Kilpatrick et al., 2003, Kochly, 2006, Bashor et al., 2005) addressed all the aspects already described, and represents the biggest contribution to structural monitoring of the wind-induced response. In particular, they used accelerometers and GPS sensors to measure the structural response, which was compared with predictions from wind tunnel tests on aeroelatic models to verify the validity of current practices.

However, despite their big research effort, many points are still open in the monitoring of structures subject to wind action. First, the literature review shows that no structures except tall buildings have been devoted to a systematic dynamic identification and validation of the wind design practice through full-scale measurements. Moreover, the few validations carried out has validated only wind tunnel tests results, while no analytical models of wind loading and response have been verified in full-scale.

The validations carried out by Li et al. (2004, 2008) were based only on accelerometer records, from which it is not possible to recover the mean and the slow variations of the wind-induced displacements (quasi static response); therefore, only the resonant part of the full-scale response was compared with wind tunnel results. Meanwhile, it was introduced the possibility to exploit the GPS technology for the monitoring of structures, so that it was possible to measure directly the displacements in full scale (Tamura et al., 2002, Kijewski-Correa et al., 2006b). However, due to the continuous variation in satellite visibility and orientation, as well as for the potential multipath distortions, GPS sensors require burdensome signal processing to achieve consistently reliable measurements (Kijewski-Correa and Kochly, 2007, Kijewski-Correa et al., 2013), with the effect of losing also a small part of the quasi static response (Kochly, 2006).

In this respect, classical applications usually involve the use of strain gauges in addition to accelerometers. Despite the great number of experimental studies involving together strain gauges and accelerometers (Lee et al., 2013, Manzato et al., 2014, Dos Santos et al., 2015), no surveys have addressed the possibility of recovering structural displacements from strain measurements, nor have carried out comparisons with accelerometers in terms of capability of detecting the different parts of the total response (mean, quasi-static and resonant).

In addition to these open-points, in the relevant literature rarely it is included a clear description of how some issues, regarding specifically the management of big data, have been addressed and solved. In particular, the statistical characterization of the time intervals constituting the database and, consequently, an algorithm for the extraction of homogeneous events that are suitable for the goals of the monitoring, are mostly neglected. For example, stationarity of wind loading and response is a fundamental assumption both for operational modal analysis (OMA) and for comparisons with wind tunnel tests results; therefore, in this case, all the time intervals in the database associated to strongly non-stationary events should be discarded. In this respect, many papers have dealt with the separation of homogeneous wind events from the analysis of a wind monitoring network database (Kasperski, 2002, Lombardo et al., 2009, Yeo, 2011, Lombardo, 2012, De Gaetano et al., 2014, Burlando et al., 2018). This topic, although well established in literature, has not been properly integrated into structural monitoring applications.

Some other aspects of the database processing are often disregarded, such as a systematic guide of how to handle the detrending of signals (Brincker and Ventura, 2015) whose static and quasi static-components are needed for the analysis.

Starting from these premises, the present chapter aims to provide a guide for the monitoring of vertical slender structures subject to wind action, both with fixed and with rotating masses. This guide provides information of how to cope with every aspect of the experimental activity, from the choice and the placement of the sensors, to the management of the database in the post-processing phase, in order to build a comprehensive full-scale validation procedure of the wind design practice of vertical slender structures.

2.2 Selection of the case study

The choice of the test structure should consider, when possible, a number of aspects that might simplify the design of the monitoring system and improve the reliability of the measurements.

First, the structure should be easily accessible to facilitate maintenance interventions that are required during long-term monitoring. The availability of the electric grid and of local area network (LAN) will guarantee the power supply to each sensor and the stability of Internet access. If not, in remote contexts, the power supply of sensors and acquisition units should make use of PV panels and batteries, while the data communication can be made via mobile broadband connection. Finally, the structure should be located in an open area, far from obstacles disturbing the wind field and from electric noise sources.

2.3 Measurement chain

In this section, the design of the measurement chain is discussed, detailing some important aspects that should be considered when planning and designing the long-term monitoring.

2.3.1 Number and location of sensors

The first task in dynamic measurement planning is the selection of the sensor locations and directions, which determines the total number of measurements. The minimum number of sensors to be used comes from the number of vibration modes contributing significantly to the response (Brincker and Ventura, 2015).

When dealing with the wind-induced response of slender structures, only the contribution of the first bending mode for every principal direction is generally considered in the calculation of the total response. This is especially true when the structure has a large localized mass at top (as the lighting crown typical of light towers). In this case, even a single sensor for every direction can give reliable information of the displacements. However, when the investigated effect is other than displacement, e.g., the structural stress, the number of modes to be considered may significantly increase. Considering that wind loading spectrum is concentrated in the low frequency range, generally two vibration modes are enough to describe any wind-induced effect.

Differently, when rotating masses are present, such as for wind turbines, the wind loading on the structure is “sampled” by the rotation of the mobile components. Therefore, the loading spectrum has peaks at frequencies that are multiple of the rotational velocity, contributing to excite higher vibration modes with respect to the fixed-masses condition. For these reasons, the number of modes to be considered increases. In this case, preliminary modal analysis should be performed to investigate possible resonances at the maximum velocity of the rotating parts.

As a general practice, it is convenient to augment the numbers of the sensors with respect to the minimum requirements. This allows to compensate for possible problems or malfunctions of the sensors (e.g. incapability of detecting quasi-static vibrations, sensitivity to temperature), to identify noise sources, or to obtain accurate estimation of the mode shapes.

With regard to the location, sensors should be installed at the antinodes of the considered vibration modes, in order to maximize the signal-to-noise ratio. It is important that no sensors are placed in a node point for any mode of interest because otherwise the sensor cannot obtain any information about this mode. The measurement points should be spread over the structure in such a way that each individual measurement point does not repeat any information in other channels. The choice of the

location can be based on experience or can also be based on computer simulations using finite element models or on predictions of the dynamic response based on simple beam theory. Additional information on the best location of sensors can be found in Kirkegaard (1991).

2.3.2 Sensor types and characteristics

Transducers should be small and lightweight with respect to the test structure to minimize the influence of the added mass. The selected sensors must be sensitive enough to measure the actual operating signals. Before performing the actual test of a structure, it is important to have an idea about the expected levels of vibration. In many cases, the designer of the structure may be helpful in providing information about the types and amplitude of the expected dynamic loads. Furthermore, sensors must be able to measure the frequency range of interest, that is, the maximum and minimum frequencies to be recorded and analyzed. As described in the previous section, the selection of the maximum significant frequency of the operating response (which defines to the number of modes to consider) is often the most challenging part of this task.

2.3.2.1 Accelerometers

Accelerometers are the most popular sensors in structural monitoring applications because of the robustness of the measurements and the ease of use. However, their limited frequency range, which in general does not include the very low frequencies, makes them inadequate when static and quasi-static displacement information is needed.

Accelerometers commonly used in engineering applications can be grouped into three categories: Piezoresistive, Piezoelectric and Capacitive (MEMS).

A piezoresistive accelerometer produces resistance changes in strain gauges that are embedded in the accelerometer system. These accelerometers have a very wide frequency range which makes them the best solution for measuring short duration (high frequency) shock events such as crash testing. Usual values of sensitivity are quite low, preventing the use of these sensors for low frequency and low amplitude signals. Mainly for these reasons, and considering also that they are much more expensive with respect of the other types of sensors, they are generally not used for the measurements of wind-induced vibrations.

Piezoelectric accelerometers typically use lead-zirconate titanate sensing elements which under acceleration produce a proportional electric output. They are the first choice for most vibration measurements due to their wide frequency response and good sensitivity. In addition, piezoelectric accelerometers have very low noise levels that suits perfectly with vibration testing. However, they generally cannot measure vibrations below a few hertz, but there are high sensitivity accelerometers that go down to 0.1 Hz. Therefore, they are excluded from applications where quasi-static response is needed. Since wind-induced vibrations are concentrated in the low frequency range, piezoelectric accelerometers are suitable for the goals of the monitoring as long as they can measure in the neighborhood of the fundamental frequency of vibration.

Micro-Electro-Mechanical System (MEMS) indicates a family of sensors manufactured using microelectronic fabrication techniques. These techniques create mechanical sensing structures of microscopic size, typically on silicon. When people refer to MEMS accelerometers they are likely referring to capacitive accelerometers although this technology can be used for other types as well. Capacitive MEMS accelerometers contain a seismic mass that under acceleration undergoes variation of the electrical capacity. Because of their low cost and small size, they have become quite popular

and are present in many electronic devices. Capacitive MEMS accelerometers are best suited for measuring low-frequency vibration, motion, and steady-state acceleration, but they suffer from a poor signal to noise ratio, a limited bandwidth, and mostly restricted to smaller acceleration levels (less than 200g). For these reasons they are particularly suited for measurements of wind-induced vibrations, making sure they are sufficiently low-noise.

2.3.2.2 Strain gauges

From a theoretical viewpoint, strain gauges have the advantage of providing reliable information both of the mean, quasi-static and resonant response. However, since the connection to the structural surface is realized through the use of glue, whose performance can decrease over time, strain gauges can slightly lose the capability of measuring the fast oscillations associated to the resonant response.

Strain gauges are based on the "Piezoresistive Effect". When a strain gauge is bonded to a surface under stress, it will distort or flex in unison with that surface causing a shift in electrical resistance proportional to the strain applied to the surface. A formula can then be used to convert the fluctuations of resistance to an accurate strain reading.

Strain gauges can be divided according to the configuration of the Wheatstone bridge, which is the electrical circuit used to measure the instantaneous resistance; they can be quarter-bridge, half-bridge or full-bridge. As it is known, strain gauges are strongly sensitive to measurement errors, mainly due to temperature and to the cables. Since the quarter-bridge configuration does not use any auxiliary gauge to compensate such effects, they should always be avoided in structural monitoring applications. Both half-bridge and full-bridge mitigate such errors, with the difference that the full-bridge configuration enhance the accuracy of the measure, but its realization is more expensive and time-consuming.

It is important to highlight that another limit of strain gauges is that they require highly experienced labor for their installation, where improper executions can invalidate the measurements.

2.3.2.3 Displacement sensors

Several sensors are capable of providing direct displacement measurements. A few that have been applied recently to structural engineering include laser Doppler vibrometers (LDV), microwave interferometer and terrestrial positioning systems (TPS).

However, even if these sensors have shown promising results for several applications (Nassif et al., 2004, Pieraccini et al., 2004, Leica, 2004) they are not well suited for continuous long-term monitoring, as they are strongly dependent on weather and environmental conditions (Kochly, 2006).

Global positioning systems (GPS) have the capability of operating continuously, unattended and in all weather conditions. GPS sensors can directly provide total displacements along two perpendicular horizontal axes, as well as in the vertical direction, though with lesser accuracy. New models can work at a sampling rate up to 20 Hz, thus becoming suitable for monitoring a wide range of structures (a deepening on the sampling rate is discussed in section 2.3.4.1).

However, benchmark tests have proven the GPS sensors to have accuracies at the sub-centimeter level (Kijewski-Correa, 2013). Therefore, they appear to be suited for the monitoring of high-rise buildings, while they are still incapable of measuring the low vibration level characterizing mid-rise slender structures like poles and towers.

Finally, it is timely to highlight that GPS sensors require considerable signal processing to achieve consistently reliable measurements (Kijewski-Correa and Kochly, 2007, Kijewski-Correa et al., 2013), with the effect of losing also a small part of the quasi static response (Kochly, 2006).

2.3.2.4 Wind and meteorological sensors

When monitoring the wind-induced response, it is fundamental to correlate simultaneous measures of the wind field around the considered structure. Outcomes from anemometers in the nearby can be exploited for this purpose, however, the installation of an anemometer on the structure itself is always preferable, in order to maximize the correspondence in time and space of wind loading and structural response. A fundamental aspect to consider when installing an anemometer is the height of the surrounding buildings and obstacles, so that the sensor is not in their wake.

With regard to their typology, the most widespread anemometers in full-scale monitoring applications are the cup anemometer and the ultrasonic anemometer. Cup anemometer is a mechanical sensor, made of three or four hemispherical cups mounted on horizontal arms, which in turn are connected to a vertical shaft. This sensor is based on the principle that the flow velocity is proportional to the spinning rate of the cups. The cup anemometer has undergone many modifications over the years to improve its performance and today it is still widely used for its low cost and facility of installation. However, vertical component of velocity cannot be measured, and the low temporal resolution make it not suitable for turbulence measurements. In this respect, the ultrasonic anemometer can sample wind velocity even 10-20 times per second, providing reliable turbulence quantification. Ultrasonic anemometers use ultrasonic sound waves to measure wind velocity: they measure wind speed based on the time of flight of sonic pulses between pairs of transducers. They can be both biaxial and triaxial, and thus are used when information of the vertical velocity is needed (as in the study of thunderstorms). The main disadvantage is the lower accuracy in case of precipitation, where raindrops may vary the speed of sound.

In addition to the anemometer, sensors measuring humidity, temperature or pressure can be installed to obtain a better meteorological characterization of wind events. Information of pressure is extremely useful to validate isolated peaks in the velocity signals. Temperature is important to interpret the strain records. Information of the meteorological stability is also fundamental to separate synoptic from non-synoptic wind events, which have different effects on structures (Solari, 2014).

2.3.3 Cabled vs wireless sensors

Despite wireless sensing technology has made significant advances in recent years, many people involved in vibration testing are still using wired sensors. There are some good reasons why cables are still being used. These reasons are as follows:

- Time synchronization of the different sensor measurements;
- Power supply problems with wireless units;
- Reliability of wireless systems not comparable to that of wired systems.

When wireless systems are being used, normally digital information is transferred wirelessly. This means that the analog-to-digital (AD) conversion is performed at the sensor. Since it is fundamental that the signals are sampled simultaneously, there is the problem of time synchronization between the different AD converters located at the sensors. This demand is easily met by GPS synchronization, that is normally within micro second uncertainty (Brincker and Ventura, 2015). In cases where a GPS signal cannot be picked up, a wired system is to be preferred.

The power supply is also a potential source of problems, because in long-term monitoring applications the measurement system must function over extended periods of time without any maintenance. If power is available at the site, a wired system might be preferred to have a reliable power supply to each sensor. If power is not available at the site, the problem of power supplying must be solved in any case, and having individual sensors, each with its own power supply might be a possible solution.

There are many reasons for the reduced reliability of wireless systems compared to the wired ones. Simple reasons are loss of connection between the sensors and the data acquisition system due to people or cars moving in the signal path and loss of GPS connection so that data cannot be synchronized. However, whenever wireless and digital solutions can be implemented without encountering the described issues, they should be applied. First, because they eliminate the primary source through which noise can enter into the measurement system (the cables), which is a primary goal of the experimental activity. In addition, it is also important to reduce cabling for two other reasons: cost and simplicity.

2.3.4 Sampling rate

Sampling rate defines the upper limit of the frequency band that can be used for the analysis of the recorded signals. It is the number of data samples acquired per unit of time and thus it is also denoted as the "sampling frequency". The upper limit of the frequency band is given by the Nyquist frequency f_v:

$$f_v = f_s/2; \quad f_s = 1/\Delta t \tag{2.1}$$

where f_s is the sampling frequency, and Δt is the sampling time step. Therefore, if the sampling frequency is 200 Hz, then the frequency band is limited to 100 Hz and any information about the structure beyond this frequency cannot be determined. This means that the sampling rate must be chosen large enough so that all the modes of interest are properly detected from the measured signals.

With the regard to the wind-induced response of slender structures, the frequency band of interest is generally below 10 Hz. A sampling frequency of 20 Hz thus represents a reasonable rate for the structural sensors, and it is certainly the most appropriate choice in real-time applications, where data transmission runs continuously and thus oversampling should be avoided. As already mentioned, in case of presence of rotating masses, the harmonic loads concentrates at frequencies that are multiple of the rotational velocity, with resultant excitation of the higher modes with respect to the fixed-masses condition. In this case, the maximum frequency of interest is dependent on the maximum rotational velocity of the mobile parts, which can vary a lot from case to case. However, one can assume that a sampling rate of 50 Hz is able to detect every contribution of interest in all situations.

The harmonic content of wind turbulence is concentrated below few hertz; therefore, considering that only standard pre-determined rates are generally compatible with the acquisition system, anemometric measurements are typically sampled at 10 Hz. If detailed information about turbulence is not required, 1 Hz can be considered a reasonable sampling frequency, especially in real-time applications. As regards the meteorological sensors, which do not need to provide dynamic measurements, the sampling rate can be lower (0.1-1 Hz).

2.3.4 Data acquisition

Before data can be analyzed, the analog signals produced by the sensors must be converted into numbers. This is done by an analog-to-digital converter (ADC). In wired systems, the conversion is accomplished by a single ADC hardware, which is also called "data-logger". It should enable to

sample simultaneously data from sensors with different sampling rate. In the conversion process from analog to digital, an important aspect must be considered. If a signal has frequency components outside of the Nyquist band, then the energy of these frequencies is artificially forced into the Nyquist band. This is known as "aliasing" of the signal and leads to erroneous interpretation of the data. In order to remove this measurement error, antialiasing filters are used to remove all signal components above the Nyquist frequency. The antialiasing filter is a low-pass filter that is designed in a way that the energy of the filtered signal is negligible for frequencies beyond the Nyquist frequency. If the antialiasing filter is not a built-in facility in the measurement system, then the user of the system should incorporate an analog filter between the sensor and the ADC. A graphical representation of this concept is shown in Figure 2.1.

After being converted and stored in the data-logger, data must be exported to files and sent automatically to the headquarter for analysis. Certain data-loggers have a built-in processor able to run the exportation and transmission phases; if no, they can be connected to a PC with a dedicated software. Data transmission can be performed through the use of a FTP server, or exploiting cloud storage services.

The last issue is related to the properties of the files to send. If the time-length of each file is not driven by real-time needs, it should be set from a compromise between the file size and the number of files of the database. A suitable choice, also in light of post-processing needs (see section 2.4.1), is to have files 10-minutes long. File format should be the most possible lightweight; in this respect binary data files are preferable.

2.3.5 Acquisition unit

The acquisition unit is the physical place where all the hardware enabling the continuous running of the monitoring is installed. To allow maintenance operations, the unit should be placed in an accessible area. Normally, it is a watertight box or a cabin at the base of the structure.

The unit must be big enough to host all the necessary hardware, which can include: data-logger, pc (mini-pc are recommended), amplifiers, UPS (uninterruptable power supply, to ensure the operation during power-loss events), mobile broadband modem and air-conditioning devices (to keep inner temperature constant over time).

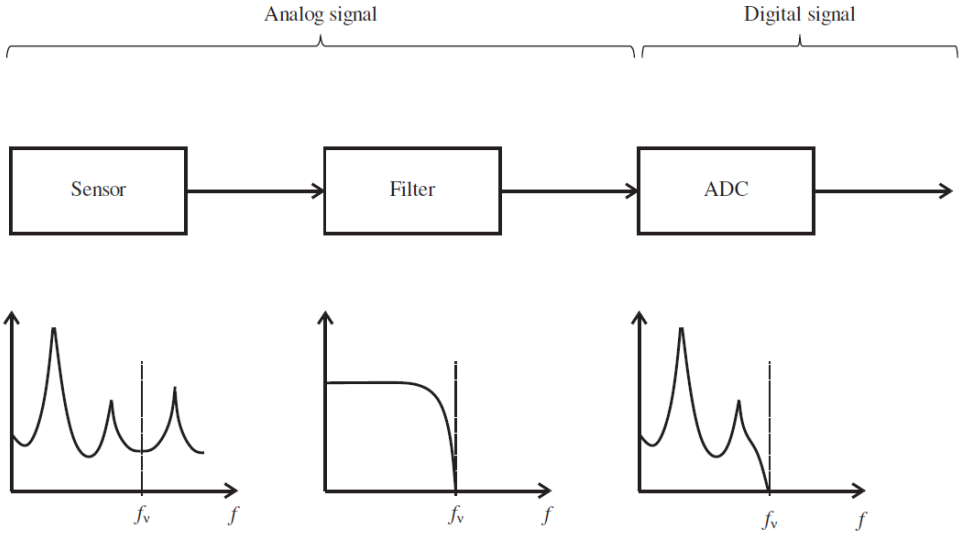

Figure 2.1. Analog-to digital conversion. From Brincker and Ventura (2015).

If the cooling of the acquisition unit is realized through ventilation (thus implying the presence of openings), those openings must be shielded to prevent water and dust to come inside.

2.4 Database management

Raw data received from the acquisition unit must be processed to make them ready-to use for analysis of the structural behavior. This section describes a coded procedure for the management of the experimental database, in order to obtain data segments suitable for the monitoring purposes and to accelerate the post-processing phase.

2.4.1 Segmenting

The database is partitioned in consecutive data segments of duration T (Figure 2.2). Time-length T is chosen according to the purposes of the analysis. Wind loading is a random process that is stationary over periods between 10 minutes and 1 hour. Therefore, when dealing with wind-induced response, it is convenient to use T=10 min or T=1h.

T=10 min is the classical time length used in wind engineering to decompose wind velocity in a static mean part and stationary turbulent fluctuations. T=1h can be best suited to perform OMA techniques, which require a better frequency resolution (especially for damping estimations).

2.4.2 Filtering

Filtering mainly means to eliminate some frequencies from the signal. The antialiasing filter, which is the analog filter that must be applied before the ADC, has been already discussed. After the ADC everything is digital, and therefore only digital filtering is used in the subsequent signal processing.

Digital filters are necessary if some frequencies in the Nyquist band must still be excluded from the signal. According to their goal, they can be divided as follows:

- High-pass filters, that exclude the lower frequencies in the Nyquist band
- Low-pass filters, that exclude the higher frequencies in the Nyquist band
- Band-pass filters, that exclude all frequencies except the frequencies in a frequency band

In general, one can say that high-pass filters are typically used to remove static and quasi-static trends, low-pass filters are used to remove energy in the high-frequency region (e.g. as a second anti-aliasing if we want to decimate data), and band-pass filters are used in order to divide a frequency band with many modes into smaller frequency bands with a less modes in each band.

2.4.3 Detrending

Detrending means to remove constant offsets in the signals, forcing the signals to have a zero mean. This step can be useful when the static components of the signal are altered due to excessive noise in the low frequency region. For instance, we can think of the trend of the signal as due to temperature effect in the electronics. Detrending is essential also for another reason. During forced vibration tests, sensors' output can be zeroed just before the application of the input excitation, so that what is measured by the sensors really represent the actual response to the input. When monitoring wind/ambient vibrations, the excitation is always active, even during the installation of the sensors, thus the correlation between zero input and zero output is lost. Hence, the static offset must be deleted in post-processing.

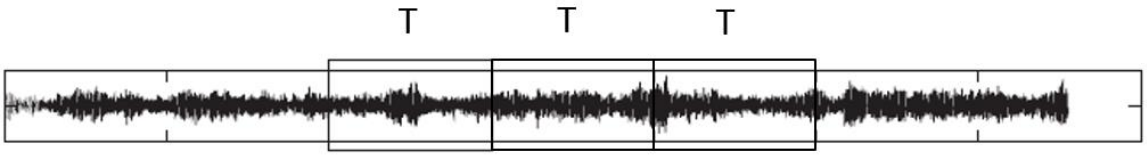

Figure 2.2. Segmenting of the database.

Detrending can be done by digital high-pass filtering. However, in cases of small trend errors, an alternative way to perform detrending is simply to remove the mean value of the considered data segment. With regard to accelerations, the detrending should be applied to every data segment, since we expect accelerations to have zero mean for every loading condition. With regard to strain or displacements, they should have zero mean only in data segments where wind velocity has zero mean. Therefore, this procedure can be applied:

- Mean wind velocity $\bar{u}$ is calculated for every data segment of the database;
- The mean value of the considered quantity $\bar{o}$ is computed for the data segments (herein called "zero wind" segments) where $\bar{u}$ is lower than a small threshold value;
- The considered quantity is finally detrended in each data segment by subtracting $\bar{o}$ of the "zero wind" segment that is closest in time.

2.4.4 Statistics and extraction

For a fast and focused extraction of data segments suitable for the purposes of the analysis, the database must be statistically characterized. In this way, data segments can be separated into homogeneous families to deal with them by models coherent with their physical reality.

In particular, the stationarity of the measured response is a fundamental assumption both for OMA techniques and for comparison with predictions from wind tunnel tests and from analytical models. Exploiting structural linearity, we can say that response is stationary if wind loading is stationary.

To extract stationary wind events, several statistical features must be calculated from the anemometric measurements. The statistics presented here are consistent with previous procedures developed and calibrated in order to process a huge amount of data, based on few synthetic elements, derived from anemometric recordings (De Gaetano et al., 2014, Burlando et al., 2018).

Prior to evaluate statistics, raw wind velocities along the horizontal axes of the anemometer, herein called $u_A(t)$, $v_A(t)$ are processed in this way:

- $U(t)$ is obtained as the magnitude of the vector sum of $u_A(t)$ and $v_A(t)$
- $\alpha(t)$ has been computed as the direction of the vector $U(t)$ with respect to the North (in clockwise direction);

Then, for each subsequent T=10-min time segment, a matrix is stored containing the following statistical parameters of U(t) into three groups:

- 1-s peak wind velocity $\hat{U}$, mean wind velocity U_{m10}, gust factor $G_{10} = \hat{U}/ U_{m10}$, turbulence intensity I_{10}, velocity skewness γ_{10}, velocity kurtosis k_{10}, mean wind direction α_{m10} and standard deviation of the wind direction $\sigma_{\alpha 10}$ in the interval T;
- maximum mean wind velocity averaged over 1-min U_{m1} and relevant gust factor $G_1 = \hat{U}/ U_{m1}$ in the interval T;

- mean wind velocity U_{m60} , gust factor $G_{60} = \hat{U}/ U_{m60}$, turbulence intensity I_{60} , velocity skewness γ_{60} and velocity kurtosis k_{60} in the1-h time interval centered around T.

It is important to specify that, despite their different definition, which is consistent with Burlando et al. (2018), $\hat{U}$ and U_{m1} are calculated with the same approach, thus as the maximum value of the moving average (calculated respectively over 1-s and 1-min periods) of U in the interval T.

With respect to the mentioned papers, to add valuable information about the variation of wind direction in 10-min segments, an additional parameter is included, which is the standard deviation of the wind direction $\sigma_{\alpha 10}$. Indeed it might occur that some wind events, which would be classified as stationary from a velocity viewpoint, exhibit considerable variations of the wind direction in 10 minutes, and therefore they cannot be treated with the classical models for the calculation of wind loading and response. The inclusion of $\sigma_{\alpha 10}$ in the dataset automatically prevents from including this kind of transient phenomena into the family of the extra-tropical depressions.

Clearly, $\sigma_{\alpha 10}$ is not directly calculated using the direction time-history α(t), since directions close in space (e.g. 2° and 357°) would result in an enormous variation with no physical meaning (Figure 2.3). The calculation of $\sigma_{\alpha 10}$ involves three steps:

- An interval of directions I_α, with a pre-selected width, is found not to be crossed by any value of the direction time-history;
- 360° is subtracted to all the direction values greater than the upper bound of I_α ;
- The standard deviation is performed to the modified direction time-history.

The width of I_α should be chosen such that, from one hand, is way larger than a typical variation between consecutive instants, from the other it must be little enough to be found almost in every data segment. Indeed it may happen that, in case of highly non-stationary phenomena, no intervals of such width are avoided by the direction time-history, that means that the wind velocity assumes every possible direction in that 10-min period. In this case $\sigma_{\alpha 10}$ is evaluated as the minimum of the standard deviations of two time histories: the original direction time-history and a modified time-history, obtained subtracting 360° to all direction values greater than 180°.

Once every time segment with duration T has been statistically characterized, the separation into homogenous families can be performed. For example, stationary data segments can be extracted imposing thresholds on G_{10}, G_{60} and $\sigma_{\alpha 10}$.

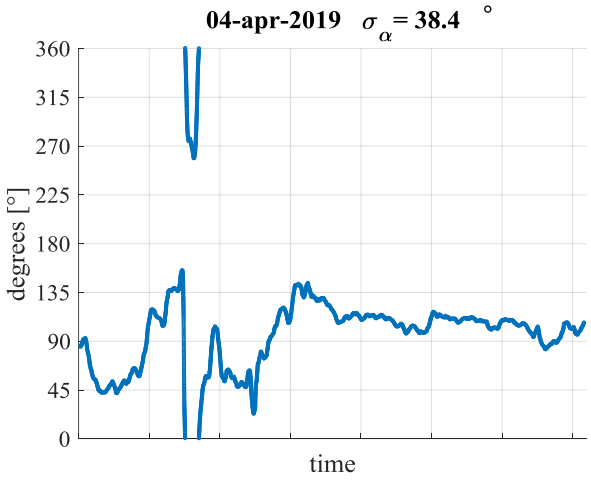

Figure 2.3. Time history of wind direction and resulting standard deviation. The direct evaluation would have led to a large value with no physical meaning

2.5 Evaluation of displacements

Calculation models of wind effects on structures provide the wind-induced response in terms of displacements or stresses. Specific sensors can directly measure these quantities (GPS and strain gauges, respectively). However, it might happen that the monitoring equipment does not include such sensors. For example, we have seen that GPS technology is not already capable of measuring the low displacements level that is typical of medium-rise slender structures. In this respect, classical applications involve the combined use of strain gauges and accelerometers. For this reason, a novel procedure to derive displacements by combining strain and acceleration measurements is developed.

Trivially, displacements can be obtained from accelerations by double integrating in the frequency domain: from the PSD of the accelerations $S_{\ddot{x}\ddot{x}}$, the PSD of the displacements derived from accelerations S_{xx_acc} is obtained dividing by ω^4. However, accelerations provide a reliable quantification only of the resonant part of the displacements. The static and quasi-static part of the response are provided by strain gauges under some assumptions.

From the elastic line equation (reference frame in Figure 2.4), known at instant t_0 the displacement function over the structural height z, $x(z,t_0)$, the bending moment $M_y(z,t_0)$ is calculated as:

$$M_y(z,t_0) = \frac{d^2x(z,t_0)}{dz^2} EJ_y \tag{2.2}$$

where EJ is the bending stiffness of the beam. Using the Navier formula, the bending deformation $\varepsilon_{zz}(z,t_0)$ is obtained as:

$$\varepsilon_{zz}(z,t_0) = \frac{M_y(z,t_0)}{W_y E} = \frac{d^2x(z,t_0)}{dz^2}\frac{J_y}{W_y} \tag{2.3}$$

with W_y elastic section modulus of the beam. From modal decomposition, assuming that the wind-induced response depends only on the contribution of the first bending mode (Solari and Pagnini, 1999), it follows that:

$$x(z,t_0) = \psi_1(z)\, p_1(t_0) \tag{2.4}$$

where $\psi_1(z)$ is the first mode shape and $p_1(t_0)$ is the first principal coordinate at instant t_0. Therefore, it follows that $\varepsilon_{zz}(z,t_0)$ is proportional to the second spatial derivative of the mode shape, herein called *strain mode shape*.

$$\varepsilon_{zz}(z,t_0) = \frac{d^2\psi_1(z)}{dz^2}\frac{p_1(t_0)J_y}{W_y} \tag{2.5}$$

Therefore, known $\varepsilon_{zz}(z_0,t_0)$ from measurements, the instantaneous principal coordinate can be calculated dividing by the strain mode shape at height z_0.

$$p_1(t_0) = \frac{\varepsilon_{zz}(z_0,t_0)}{d^2\psi_1(z_0)/dz^2}\frac{W_y}{J_y} \tag{2.6}$$

At this point, the calculation of the displacement at any height is straightforward using Eq. (2.4). Since the displacement obtained with this method is derived from strain measurements, herein after it will be called x_{est}.

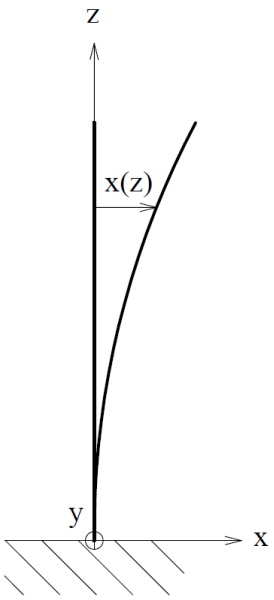

Figure 2.4. Reference frame of the elastic line equation.

As described, ε_{zz} represents the deformation in longitudinal direction due to bending. Therefore, only this quantity must be extracted from the strain measurements.

This technique for the estimation of the displacements requires that the mode shape function is continuous. Finite Element Analysis (FEA) allows extracting the values of the mode shape in many points (driven by the number of finite elements); the interpolation of such values thus enables a reliable estimation of the continuous mode shape. Instead, OMA methods provide a discrete mode shape with a limited number of points (driven by the number of the sensors); therefore, they could not be suitable since second derivatives may need to be found by finite differences and large numerical errors may be introduced. The problem that cannot be circumvented unless the numerical approach for estimation of the derivatives is improved.

The proposed method is based on the assumption that only the contribution of the first mode is considered in the total response, as it is classical in the calculation of the wind-induced response of slender structures, whatever effect is considered. While this is practically true as far as displacements are concerned, especially at the top, it is not necessarily true when dealing with other effects like strain, for which the large values of the higher strain mode shapes counteract the effect of a dominating first principal coordinate. Therefore, this method is valid for structures that tend to point-like systems, such as light towers or wind turbines, which have a big lumped mass at the top. The applicability of this method to any vertical slender structures must still be investigated.

The final step is then to combine the displacements obtained by the different sensors. To recap, accelerometers have provided displacements characterized by a reliable resonant part, while strain gauges have furnished displacements with reliable static and quasi-static parts. The combination of the displacements is carried out in the frequency domain. Taken the PSD of the two displacement time-histories, respectively called S_{xx_acc} and S_{xx_est}, the frequency f_{comb} is identified as the frequency where the two spectra intersect in the left slope of the resonant bell (Figure 2.5 a). The location of f_{comb} is chosen such that the resonant peak is provided by the accelerometers without affecting the quasi static characterization of the strain gauges.

The combined PSD of the displacement is finally defined as:

$$S_{xx\_comb} = \begin{cases} S_{xx\_est} & f \le f_{comb} \\ S_{xx\_acc} & f > f_{comb} \end{cases} \tag{2.7}$$

Figure 2.5 shows the combination of the power spectra. In 2.5a the original PSDs S_{xx_acc} and S_{xx_est} are displayed, while the thin black line identifies f_{comb}. Figure 2.5b instead shows the combined displacement spectrum S_{xx_comb} (black line); the grey line shows the part of the spectrum that has been discarded (indicated as *waste* in the figure).

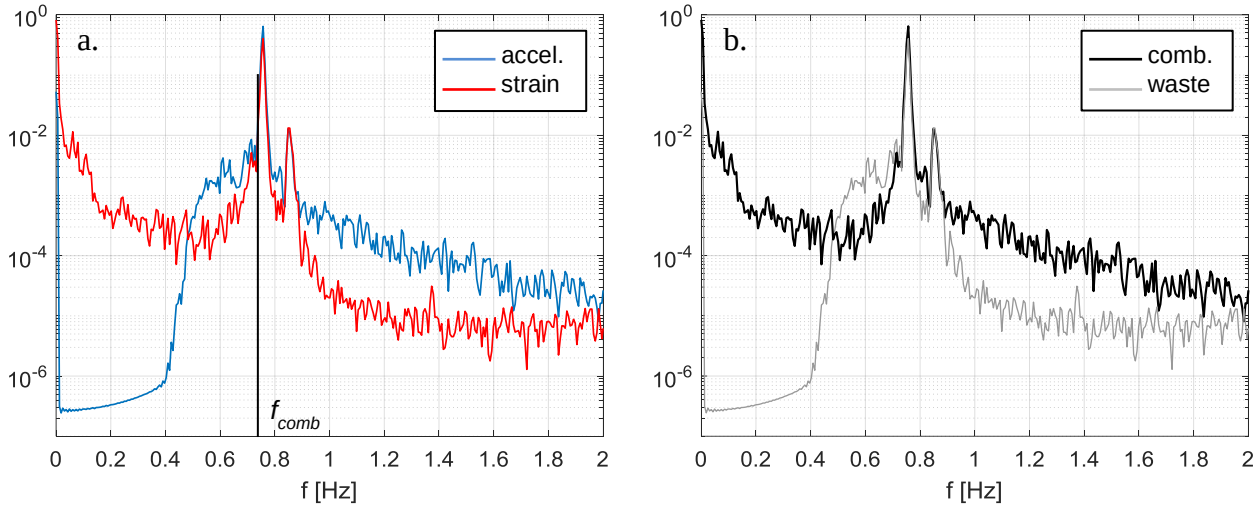

Figure 2.5. Combination of displacement spectra in the frequency domain. Displacement PSDs obtained from the sensors (a); total displacement PSD obtained by combining the sensor's spectra with relevant waste (b).

References

Bashor R, Kijewski-Correa T, Kareem A. (2005). On the wind-induced response of tall buildings: the effect of uncertainties in dynamic properties and human comfort thresholds. Proc. Am. Conf. Wind Eng, 2005.

Brincker R., Ventura C. E. (2015). Introduction to operational modal analysis. John Wiley & Sons, Ltd.

Brownjohn, J. M. W. (2007). Structural health monitoring of civil infrastructure. Phil. Trans. R. Soc. 365, 589–622.

Burlando, M., Zhang, S., Solari, G. (2018). Monitoring, cataloguing, and weather scenarios of thunderstorm outflows in the northern Mediterranean. Nat. Haz. Earth Syst. Sc. 18, 2309-2330.

Carassale, L., Percivale, F. (2007) Frequency-domain output-only identification of linear structures subject to stationary excitation. Proc. 5th Int. Conf. On Computational Stochastic Mechanics, Rhodes, Greece, Millpress, Rotterdam.

Doebling, S. W., Farrar, C. R., Prime, M. B., Shevitz, D. W. (1996) Damage identification and health monitoring of structural and mechanical systems from changes in their vibration characteristics: a literature review. Los Alamos National Laboratory report LA-13070-MS.

De Gaetano, P., Repetto, M.P., Repetto, T., Solari, G. (2014). Separation and classification of extreme wind events from anemometric records. J. Wind Eng. Ind. Aerodyn. 126, 132-143.

Farrar, C. R., Doebling, S. W., Nix, D. A. (2001). Vibration-based structural damage identification. Phil. Trans. R. Soc. 359, 131–149.

Kasperski, M. (2002). A new wind zone map of Germany. J. Wind. Eng. Ind. Aerod. 90, 1271–1287.

Kijewski-Correa, T., et al. (2006a). Validating the wind-induced response of tall buildings: A synopsis of the Chicago full-scale monitoring program. J. Struct. Eng. 132(10), 1509–1523.

Kijewski-Correa, T., Kareem, A., Kochly, M. (2006b). Experimental verification and full-scale deployment of global positioning systems to monitor the dynamic response of tall buildings. J. Struct. Eng. 132(8), 1242–1253.

Kijewski-Correa, T., Kochly, M. (2007). Monitoring the wind-induced response of tall buildings: GPS performance and the issue of multipath effects." J. Wind Eng. Ind. Aerodyn. 95(9–11), 1176–1198.

Kijewski-Correa, T., Kwon, D.K., Kareem, A., Bentz, A., Guo, Y., Bobby, S., Abdelrazaq, A. (2013). SmartSync: An integrated real-time structural health monitoring and structural identification system for tall buildings. J Struct. Eng. 139(10), 1675-1687.

Kilpatrick, J., Kijewski, T., Williams, T., Kwon, D.K., Young, B., Abdelrazaq, A., Galsworthy, J., Morrish, D., Isyumov, N., Kareem, A. Full scale validation of the predicted response of tall buildings: preliminary results of the Chicago monitoring project, 11th International Conference on Wind Engineering Proceedings, 2003.

Kirkegaard, P.H. Optimal design of experiments for parametric identification of civil engineering structures. Ph.D. thesis, Department of Building Technology and Structural Engineering, Aalborg University, Denmark, 1991.

Kochly, M. (2006), Validation of Global Positioning Systems for Monitoring Civil Infrastructure Systems: Performance Assessment and Removal of Multipath Effects, Department of Civil Engineering and Geological Sciences, Notre Dame, IN, University of Notre Dame.

Lee, E.T., Rahmatalla, S. Eun, H.C. (2013). Damage detection by mixed measurements using accelerometers and strain gages Smart Mater. Struct. 22 075014.

Li., Q. S., Fang, J. Q., Jeary, A. P., Wong, C. K. (1998). Full scale measurements of wind effects on tall buildings. J. Wind. Eng. Ind. Aerodyn. 74–76, 741–750.

Li, Q. S., Xiao, Y. Q., Wong, C. K., and Jeary, A. P. (2004). Field measurements of typhoon effects on a super tall building. Eng. Struct. 26(2), 233–244.

Li, Q.S., Xiao, Y.Q., Wu, J.R., Fu, J.Y, Li, Z.N. (2008). Typhoon effects on super tall buildings. J. Sound Vib., 313, 581–602.

Li, Q.S., Zhou, K., Li, X. (2020). Damping estimation of high-rise buildings considering structural modal directions. Earthquake Engng Struct Dyn. 49, 543–566.

Lynch, J. P. (2007): An overview of wireless structural health monitoring for civil structures. Phil. Trans. R. Soc. 365, 345–372.

Leica (2004). Leica TPS1200 Series. Heerburg, Switzerland.

Lombardo, F. T., Main, J. A., and Simiu, E. (2009) Automated extraction and classification of thunderstorm and non-thunderstorm wind data for extreme-value analysis. J. Wind. Eng. Ind. Aerod. 97, 120-131.

Lombardo, F.T. (2012). Improved extreme wind speed estimation for wind engineering applications. J. Wind Eng. Ind. Aerodyn. 104–106, 278–284.

Manzato, S., Santos, F., Peeters, B., Le Blanc, B., White, J. Combined accelerometers-strain gauges Operational Modal Analysis and application to wind turbine data. Proceedings of the 9th International Conference on Structural Dynamics, EURODYN 2014.

Nassif, H.H., Gindy, M., Davis, J. (2004). Comparison of Laser Doppler Vibrometer with Contact Sensors for Monitoring Bridge Deflection and Vibration. NDT&E International 38, 213-218.

Pagnini, L.C., Piccardo, G., Repetto, M.P. (2018). Full-scale behavior of a small size vertical axis wind turbine. Renew. Energy, 127, 41–55.

Pieraccini, M., Luzi, G., Mecatti, D., Fratini, M., Noferini, L., Carissimi, L., Franchioni, G., Atzeni, C. (2004). Remote Sensing of Building Structural Displacements Using a Microwave Interferometer with Imaging Capability, NDT&E International 37, 545-550.

Santos, F., Peeters, B., Debille, J., Salzano, C., Goes. L., Desmet, W. (2015). The use of dynamic strain sensors and measurements on the ground vibration testing of an F-16 aircraft. International Forum on Aeroelasticity and Structural Dynamics. San Petersburg, Russia.

Satake, N., Suda, K., Arakawa, T., Sasaki, A., Tamura, Y. (2003). Damping evaluation using full-scale data of buildings in Japan. J. Struct. Eng. 129(4), 470–477.

Sohn, H., Farrar, C. R., Hemez, F. M., Czarnecki, J. J., Shunk, D. D., Stinemates, D. W., Nadler, B. R. (2003). A Review of Structural Health Monitoring Literature: 1996–2001. Los Alamos National Laboratory Report, LA-13976-MS.

Solari, G., Pagnini, L.C. (1999). Gust buffeting and aeroelastic behaviour of poles and monotubolar towers. J. Fluids Struct. 13(7-8), 877-905.

Tamura, Y., Suganuma, S. (1996). Evaluation of amplitude-dependetn damping and natural frequency of building during strong winds. J. Wind Eng. Ind. Aerodyn. 59, 115-130.

Tamura Y., Matsui M., Pagnini L.C., Ishibashi R., Yoshida A. (2002). Measurement of Wind-induced Response of Buildings using RTK-GPS. J. Wind. Eng. Ind. Aerodyn. 90(12-15), 1783-1793.

Yeo, D.H. (2011). Database assisted design for high-rise structures in mixed extreme wind climates. In Proc. 13th Int. Conf. on Wind Engineering. Amsterdam, The Netherlands.

3. Wind-induced response of vertical slender structures

3.1 Introduction

The structural design and verification of poles and monotubular towers represent a very trivial problem at a first glance. Their manufacturing cost and their importance is surely modest. The static scheme of such structures, a simple cantilever beam with one or more lumped masses, is the most simple we could imagine in the structural framework. Despite their significant height, these structures never reach extreme heights.

However, a deeper analysis of the structural typology reveals a completely different reality. Even if the cost of a singular structure is limited, they are produced in such a huge quantity that they represent a considerable economic issue. Despite the triviality of the static scheme, these structures might undergo, due to wind action, extremely complex dynamic effects. Whatever their height is, the slenderness is high like no other structure. The coupled presence of a slender shaft and a lumped mass at the top may give rise to aeroelastic problems, with several critical wind-structure interactions.

The investigation of the wind-induced response of vertical slender structures started in the 1960s thanks to the pioneering contribution of Davenport (1961, 1964, 1967) He expressed the maximum alongwind displacement as the product of the mean static displacement by a non-dimensional constant coefficient, the gust response factor (GRF), which takes into account only the first vibration mode. As a direct consequence, Davenport defined the equivalent static force (ESF) as the force distribution that statically applied on the structure produces the maximum displacement. Exploiting structural linearity, the ESF was assigned as the product of the mean static force by the GRF.

Studies in the 1970s followed two distinct lines. Vellozzi and Cohen (1968), Vickery (1970) and Simiu (1976, 1980) retained the expression of the GRF as proposed by Davenport, introducing advances in wind and aerodynamic modelling. ESDU (1976) and ECCS (1978) determined the maximum values of load effects (e.g. bending moments and shears) using the influence function technique (IFT). At the beginning of the 1980s Solari derived a closed-form solution (CFS) of the GRF (1982, 1983) and later developed the Equivalent Wind Spectrum Technique (1988), a method by which turbulence is schematized as an equivalent field perfectly coherent in space, which enabled to obtain an advanced CFS (1989).

Research in the 1990s derived from the observation that the ESF, as initially conceived by Davenport, usually supplies reliable displacements but may involve errors in other load effects. Kasperski (1992) used the IFT to develop the load–response correlation (LRC) technique, a method that defines the quasi-static part of the ESF as the most probable load distribution for each specified load effect.

In parallel, a 3-directional (3-D) GRF technique was developed to generalize original Davenport's method from alongwind to 3-D response of structures (Piccardo and Solari, 1998, 2000). Based on this procedure, alongwind, crosswind and torsional ESFs were expressed as one generalised load distribution multiplied, respectively, by three non-dimensional constant coefficients, the alongwind, crosswind and torsional GRFs, each taking into account the corresponding first mode of vibration.

Within this framework, at the end of the 1990s, the Wind Engineering group at the University of Genova refined the gust factor technique to formulate an ad hoc calculation procedure for evaluating wind effects on poles and mono-tubular towers, in order to fill the void of a reliable calculation

method in national and international standards for this structural typology. The research efforts led to the development of a simplified model (Solari and Pagnini, 1998, 1999), generalizing the 3-D GRF to the presence of localized masses and aeroelastic terms.

In subsequent formulations, the 3-D gust effect factor (GEF) technique was developed (Piccardo and Solari, 2002, Solari and Repetto, 2002) representing the junction point and the progress of the above two research lines. It provides the alongwind, crosswind and torsional ESFs on cantilever vertical structures, calibrated to furnish specific load effects. This aim is pursued by expressing such ESFs as one generalized distribution multiplied, respectively, by three non-dimensional coefficients, the alongwind, crosswind and torsional GEFs, each depending on the load effect considered. Due to these properties, the 3-D GEF technique may be considered the generalization of the original GRF Davenport's method.

In the last years, Pagnini and Piccardo (2017) enriched the gust factor formulation by defining a Generalized Gust Factor (GGF) suitable for dealing with both buffeting and aeroelastic effects, namely vortex shedding and galloping vibrations. This method is applicable to general slender structures, variously inclined and constrained, representing the last step of the generalization of the gust factor technique.

Given the wide choice of calculation models, one of the main goals of the thesis is to apply to a case study one of the available methods, in order to validate it in full-scale. The present chapter introduces the calculation model that is used in the present work to calculate the wind-induced response of vertical slender structures. The modelling of wind loading and wind-induced response is reported in detail, and the engineering simplifications that lead to the CFS are discussed. Lastly, the chapter describes the main parameters involved in the calculation and how they have been evaluated to apply the full-scale validation procedure.

3.2 Calculation model

To evaluate the wind-induced response of vertical slender structures with fixed masses, the calculation model provided by Solari and Pagnini (1998, 1999) for light poles and monotubular towers is taken as a reference in the present work. It is a refined analytical model, and it provides a closed form solution of the gust buffeting response of poles and towers with localized masses, both in the alongwind and in the crosswind direction.

The wind-induced response is expressed taking into account aeroelastic terms for a stable system (i.e. not subject to galloping instability); indeed, the contribution of the aerodynamic part of damping is considered. In addition, the model furnishes the conditions for the occurrence of galloping instability. Considerations about vortex shedding response are also included in Solari and Pagnini (1998), but disregarding non-linear effects (later included in Pagnini and Piccardo, 2017).

Starting from a general formulation involving burdensome numerical evaluations, the model discusses and applies engineering simplifications leading to a CFS suitable for structural verifications.

3.2.1 Wind field

Let *x, y, z* be a Cartesian reference system with origin at O on the ground; *z* is vertical and directed upwards. The wind field along *z*-axis is represented by the temporal law of the instantaneous velocity vector **U** (Figure 3.1):

$$\mathbf{U}(z,t) = \bar{\mathbf{U}}(z) + \mathbf{U}'(z,t) \tag{3.1}$$

in which t is the time, $\bar{\mathbf{U}}$ is the mean wind velocity over a time interval T=10 minutes, and **U'** is the turbulent fluctuation of **U** around $\bar{\mathbf{U}}$. Considering near-neutral atmospheric conditions and the internal boundary layer, we can write:

$$\bar{\mathbf{U}}(z) = \mathbf{i}\bar{u}(z) \tag{3.2}$$

$$\mathbf{U}'(z,t) = \mathbf{i}u'(z,t) + \mathbf{j}v'(z,t) + \mathbf{k}w'(z,t) \tag{3.3}$$

where **i**, **j**, **k** are the unit vectors associated respectively with x, y, z; $\bar{u}$ is the mean wind velocity aligned with x; u',v',w' are the longitudinal, lateral and vertical turbulence components. As is usual in the study of vertical structures, w' is ignored. Therefore, the instantaneous wind velocity vector is contained in the horizontal plane and its Cartesian components in x and y directions are respectively:

$$\begin{aligned} u(z,t) &= \bar{u}(z) + u'(z,t) \\ v(z,t) &= v'(z,t) \end{aligned} \tag{3.4}$$

The mean wind velocity profile is classically expressed by the logarithmic law (Simiu, 1973):

$$\begin{cases} \bar{u}(z) = 2.5\, u_* ln(z/z_0) & z \geq z_m \\ \bar{u}(z) = \bar{u}(z_m) & z < z_m \end{cases} \tag{3.5}$$

where u_* is the shear velocity, z_0 is the roughness length and z_m is the value of z below which ū is taken as constant to be on the safe side.

Atmospheric turbulence is a stationary Gaussian random process. It is assumed that turbulent fluctuations are small with respect to the mean wind velocity ($u'/\bar{u}$ <<1, $v'/\bar{u}$ <<1, Davenport, 1961) and that u' and v' are not correlated (ESDU 85020, 1993).

The turbulence components are represented by their respective intensities:

$$I_\varepsilon(z) = \frac{\sigma_\varepsilon}{\bar{u}(z)} = \frac{k_\varepsilon}{\ln(z/z_0)} \quad (\varepsilon = u, v) \tag{3.6}$$

where σ_ε is the standard deviation over T=10 min of ε, assumed to be invariant with z (Solari, 1987); k_u=1, k_v=0.78 (Solari and Piccardo, 1998). Turbulence integral length scales are considered invariant with wind velocity:

$$L_u(z) = 300(z/300)^\delta \qquad L_v(z) = 0.25 L_u(z) \tag{3.7}$$

$$\delta = 0.46 + 0.074 ln(z_0) \tag{3.8}$$

3.2.2 Aerodynamic actions

Consider the pole or the monotubular tower schematized in Figure 3.2. The shaft is modelled by a slender cantilever beam whose vertical axis coincides with z; its cross-section has tubular circular or polygonal shape; let h be the height of the shaft above ground. N localized masses are applied to the shaft (as the equipment at the summit or rest platforms) in nodal points k (k=1,2,...,N) at height z_k.

The structure undergoes aerodynamic actions partly distributed along the axis of the shaft and partly concentrated in the geometrical centre of the masses assumed as coincident with the z-axis.

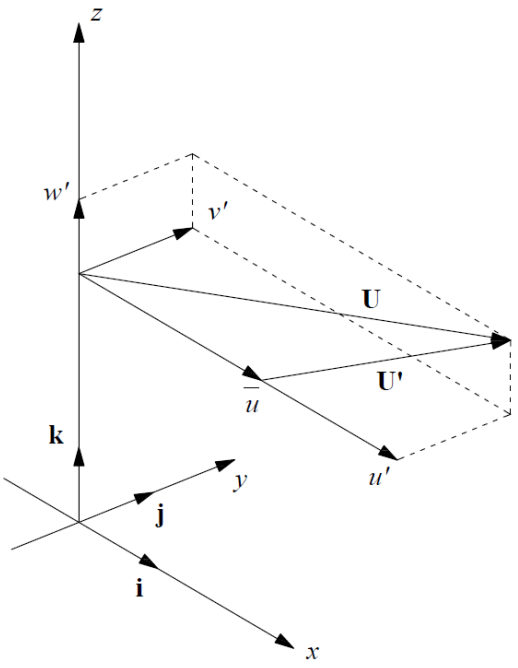

Figure 3.1. Wind field representation of the selected calculation model.

Aerodynamic actions along the shaft can be resolved into alongwind and crosswind forces F_{0x}, F_{0y}, and torsional moments M_{0z} around z. Ignoring M_{0z} due to shaft slenderness and torsional stiffness, F_{0x} and F_{0y} are given by:

$$F_{0\alpha}(z,t) = \bar{F}_{0\alpha}(z) + F'_{0\alpha}(z,t) \qquad (\alpha = x, y) \tag{3.9}$$

with $\bar{F}_{0\alpha}$ being the mean value of $F_{0\alpha}$; $F'_{0\alpha}$ is the fluctuation of $F_{0\alpha}$ around $\bar{F}_{0\alpha}$.

Aerodynamic actions on the kth mass are represented by a force $\mathbf{F_k}$ and a moment $\mathbf{M_k}$ with Cartesian components F_{kx}, F_{ky}, F_{kz} and M_{kx}, M_{ky}, M_{kz}. Ignoring the vertical force F_{kz}, the bending moments M_{kx}, M_{ky}, which are small if masses are small and compact, and the torsional moment M_{kz} which is not influential due to shaft torsional stiffness, F_{kx} and F_{ky} are given by:

$$F_{k\alpha}(t) = \bar{F}_{k\alpha} + F'_{k\alpha}(t) \qquad (k = 1, 2, ..., N) \tag{3.10}$$

with $\bar{F}_{k\alpha}$ being the mean value of $F_{k\alpha}$; $F'_{k\alpha}$ is the fluctuation of $F_{k\alpha}$ around $\bar{F}_{k\alpha}$.

Combining Eqq. 3.9 and 3.10 the aerodynamic forces acting on the monotubular tower turn out to be:

$$\bar{F}_{\alpha}(z) = \bar{F}_{0\alpha}(z) + \sum_{k=1}^{N} \bar{F}_{k\alpha}\delta(z - z_k) \qquad (\alpha = x, y) \tag{3.11}$$

$$F'_{\alpha}(z,t) = F'_{0\alpha}(z,t) + \sum_{k=1}^{N} F'_{k\alpha}(t)\delta(z - z_k) \qquad (\alpha = x, y) \tag{3.12}$$

where $\delta(.)$ is the Dirac delta function.

In order to simplify the description of the calculation model, whose detailed definition is beyond the goal of this thesis, we just can say that the aerodynamic forces depends on the drag and lift coefficients of the shaft, C_D and C_L, on the drag and lift coefficients of the kth mass, C_{Dk} and C_{Lk} and also on their respective first angular derivatives C'_D, C'_L, C'_{Dk}, C'_{Lk}.

For polygonal cross-sections, it is observed that increasing the number of sides (poles and monotubular towers rarely have sections with less than six sides) C_D is more and more regular (ESDU 79026, 1980) while C_L tends to zero. In the limit case of circular section C_D is constant and C_L=0; then C'_D=C'_L=0. Taking also into account the fact that poles and monotubular towers usually adopt rounded corners, it seems reasonable to assume, for engineering purposes, C_L= C'_D independently of the shape of the polygon; C'_L=0 is assumed only for regular polygons with more than eight sides (Cook, 1990). In addition, starting from the premise that localized masses exhibit a wide range of complex shapes, difficult to characterize from an aerodynamic viewpoint, as a first approximation it is assumed that C_{Lk}=C'_{Dk}=C'_{Lk}=0. Based on these simplifications, it follows that the mean crosswind forces are null and the fluctuating forces depends solely on the velocity components in their own direction:

$$\bar{F}_{0x}(z) = \frac{1}{2}\rho\bar{u}^2(z)b(z)C_D(z) \tag{3.13}$$

$$\bar{F}_{kx} = \frac{1}{2}\rho\bar{u}^2(z_k)A_kC_{Dk} \tag{3.14}$$

$$\bar{F}_{0y}(z) = \bar{F}_{ky} = 0 \tag{3.15}$$

$$F'_{0x}(z,t) = \rho\bar{u}(z)u'(z,t)b(z)C_D(z) \tag{3.16}$$

$$F'_{0y}(z,t) = \frac{1}{2}\rho\bar{u}(z)v'(z,t)b(z)[C_D(z) + C'_L(z)] \tag{3.17}$$

$$F'_{kx}(t) = \rho\bar{u}(z_k)u'(z_k,t)A_kC_{Dk} \tag{3.18}$$

$$F'_{ky}(t) = \frac{1}{2}\rho\bar{u}(z_k)v'(z_k,t)A_kC_{Dk} \tag{3.19}$$

where ρ is the air density, b is the reference size of the cross-section (generally the diameter), and A_k is the reference area of the kth mass.

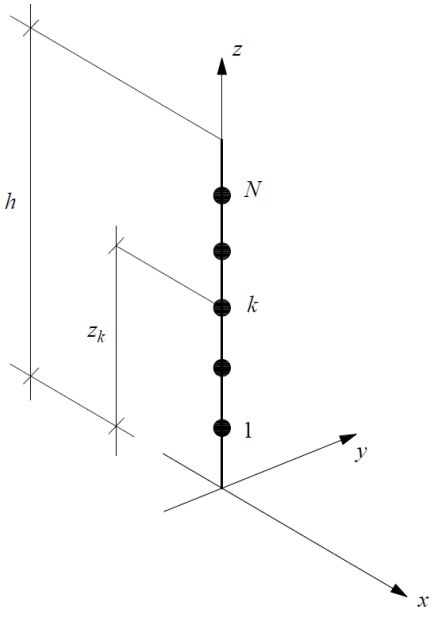

Figure 3.2. Structural model of the monotubular tower.

3.2.3 Gust buffeting response

The dynamic response of the monotubular tower is calculated assuming a linear viscoelastic behaviour. The displacements in the alongwind and crosswind direction, indicated respectively by *x* and *y*, are non-correlated stationary Gaussian random processes:

$$\alpha(z,t) = \bar{\alpha}(z) + \alpha'(z,t) \qquad (\alpha = x, y) \tag{3.20}$$

with $\bar{\alpha}$ being the mean value of α ; α' is the fluctuation of α around $\bar{\alpha}$. The mean force $\bar{F}_x$ produces the mean displacement $\bar{x}$; the fluctuating forces F_x' , F_y' give rise respectively to the fluctuating displacements x' , y' ; since $\bar{F}_y$ = 0 (Eq. 3.13), then also $\bar{y}$ = 0.

The mean value of the maximum displacement in direction α in the time interval T=10 minutes (called maximum displacement for simplicity) is given by:

$$\alpha_{\max}(z) = G_\alpha(z)\bar{\alpha}^x x(z) \tag{3.21}$$

where $\bar{\alpha}^x x$ is the static displacement due to the application of $\bar{F}_x$ in direction α; G_α is the GRF.

The solution of Eq. (3.19) is drastically simplified assuming that the displacement component α depends only on the contribution of the first mode shape $\psi_{\alpha 1}(z)$ in the plane αz. The static displacement $\bar{\alpha}^x x$ results:

$$\bar{\alpha}^x x(z) = \psi_{\alpha 1}(z)\frac{\rho \bar{u}^2(\bar{z})\bar{b}h\psi_{\alpha 1}(h)}{2m_{\alpha 1}(2\pi n_{\alpha 1})^2}\bar{C}_D\bar{K}_{\alpha x} \tag{3.22}$$

where $n_{\alpha 1}$ is the frequency of the first vibration mode in direction α and $m_{\alpha 1}$ is the relevant modal mass of the structure; $\bar{z}$ = 0.6h, $\bar{b} = b(\bar{z})$, $\bar{C}_D = C_D(\bar{z})$ and $\bar{K}_{\alpha x}$ is an appropriate non-dimensional coefficient defined in Solari and Pagnini (1998). The GRF is defined as:

$$G_x = 1 + 2g_x I_u(\bar{z})\sqrt{Q^2{}_x + R^2{}_x} \tag{3.23}$$

$$G_y = g_y I_v(\bar{z})\frac{\left|\bar{C}_D + \bar{C}_L'\right|}{\bar{C}_D}\sqrt{Q^2{}_y + R^2{}_y} \tag{3.24}$$

$$g_\alpha = \sqrt{2\ln[\Lambda_\alpha \upsilon_\alpha T]} + \frac{0.5772}{\sqrt{2\ln[\Lambda_\alpha \upsilon_\alpha T]}} \tag{3.25}$$

$$\upsilon_\alpha = n_{\alpha 1}\sqrt{\frac{R^2{}_\alpha}{Q^2{}_\alpha + R^2{}_\alpha}} \tag{3.26}$$

g_α and υ_α are respectively the peak coefficient and the expected frequency of α'; Λ_x=1, Λ_y=2. Q_α and R_α are non-dimensional parameters associated respectively to the quasi-static part and the resonant part of the response:

$$Q_\alpha = \frac{1}{\bar{K}_{\alpha x}}(K_0' Q_{0\alpha} + \sum_{k=1}^{N} K_{k\alpha}' Q_{k\alpha}) \tag{3.27}$$

$$R_\alpha = \frac{1}{\sqrt{\delta_{\alpha 1}}} \frac{1}{\bar{K}_{\alpha x}} (K'_0 D_{0\alpha} + \sum_{k=1}^{N} K'_{k\alpha} D_{k\alpha}) \tag{3.28}$$

Where $\delta_{\alpha 1}$ is the logarithmic decrement of the first modal damping in direction α; the relevant damping ratio is $\delta_{\alpha 1}/2\pi$; $Q_{0\alpha}$ and $D_{0\alpha}$ are respectively quasi-static and resonant parameters associated to aerodynamic actions on the shaft; similarly $Q_{k\alpha}$ and $D_{k\alpha}$ are quasi-static and resonant parameters associated to aerodynamic actions on the kth localized mass. K'_0 and $K'_{k\alpha}$ are additional non-dimensional coefficients defined in Solari and Pagnini (1998).

The modal damping $\delta_{\alpha 1}$ is composed of a structural part and an aerodynamic part, result of wind-structure interaction:

$$\delta_{\alpha 1} = \delta_{s1} + \delta_{A\alpha 1} \tag{3.29}$$

The logarithmic decrement of the aerodynamic part of the first modal damping both in alongwind and in crosswind direction is given by:

$$\delta_{Ax1} = \frac{\rho \bar{u}(\bar{z}) \bar{b} h \bar{C}_D \psi^2{}_{x1}(h)}{2 n_{x1} m_{x1}} (K''_{0x1} + \sum_{k=1}^{N} K''_{kx1}) \tag{3.30}$$

$$\delta_{Ay1} = \frac{\rho \bar{u}(\bar{z}) \bar{b} h (\bar{C}_D + \bar{C}'_L) \psi^2{}_{y1}(h)}{4 n_{y1} m_{y1}} (K''_{0y1} + \sum_{k=1}^{N} K''_{ky1}) \tag{3.31}$$

with K''_{0x1}, K''_{0y1}, K''_{kx1}, K''_{ky1} non-dimensional coefficients still defined in Solari and Pagnini (1998).

3.2.4 Limits and perspectives

As stated in the reference paper (Solari and Pagnini, 1999) some problems deserving further study come out of this framework. Wind-structure interaction is simulated considering only the alongwind and crosswind displacements. As a matter of fact, due to the large shaft flexibility, the rotations of the local masses in the alongwind and crosswind planes should not be ignored. In this same context, neither vertical turbulence nor moments around the x- and y-axis should be neglected.

The second aspect which is worth of deeper study concerns the nonlinear behavior from a geometric and aeroelastic viewpoint. From the geometric viewpoint the mass at the summit, paired to large deformation states, brings about second order effects whose extent must still be investigated.

Furthermore, the lack of extensive experimental studies on the aerodynamic of polygonal cylinders needs to be filled to obtain reliable aerodynamic coefficients and relevant angular derivatives. The damping database for this structural type needs to be enlarged too, since only few full-scale studies have dealt with its quantification (Pagnini and Solari, 2001, Carassale and Percivale, 2007).

Therefore, to develop the theory further, the necessity arises to carry out full-scale investigations to validate or calibrate the reliability of the model. Starting from these premises, in the next chapters the calculation model is applied to the monitored structures for a comparison with measurements. In order to evaluate the intrinsic capability of the model to predict the actual wind-induced behavior, the input parameters needed for its application must be identified with the maximum possible accuracy, so that uncertainties from different sources are not overlapped. Indeed, the parameters constitute an uncertainty source themselves. From the description of the model in the previous section, the main parameters contributing to the wind-induced response turn out to be:

- Wind parameters: roughness length z_0, turbulence intensity I_ε and integral length scale L_ε (ε=u,v);
- Loading parameters: mean aerodynamic force coefficients, namely drag coefficient C_D and lift coefficient C_L and their first angular derivatives C'_D, C'_L;
- Response parameters: first natural frequencies $n_{\alpha 1}$, mode shapes $\psi_{\alpha 1}$ and modal damping $\delta_{\alpha 1}$ (α=x,y).

Suitable values of these parameters are available in current codes and standards. However, their generalization to a comparable case study is always very delicate. Therefore, in the present study the parameters are evaluated from direct measurements in full-scale or from wind tunnel tests. For some parameters, measurements are not possible (z_0) or would be unreliable ($\psi_{\alpha 1}$, see section 4.5.1); in that case, they are estimated with appropriate methods.

By applying the response calculation model with the measured values of the input parameters, the comparison between measured and calculated response supplies the model error. Then, varying the parameters one by one, getting them from the calculation model or from current standards, it is possible to quantify how much each parameter affects model's prediction. Lastly, the experimental evaluations (in particular of damping and of the aerodynamic coefficients) enrich the relevant databases for the considered structural typology.

References

Carassale, L., Percivale, F. (2007) Frequency-domain output-only identification of linear structures subject to stationary excitation. Proc. 5th Int. Conf. On Computational Stochastic Mechanics, Rhodes, Greece, Millpress, Rotterdam.

Cook, N. J. (1990). The Designer's Guide to Wind Loading of Buildings. Part 2: Static Structures. Butterworths: Building Research Establishment.

Davenport, A.G. (1961). The application of statistical concepts to the wind loading of structures. Proc. Inst. Civ. Eng. London 19, 449–472.

Davenport, A.G. (1964). Note on the distribution of the largest value of a random function with application to gust loading. Proc. Inst. Civ. Eng. London 24, 187–196.

Davenport A.G. (1967). Gust loading factors. J. Struct. Div. ASCE 93, 11–34.

ECCS (1978). Recommendations for the calculation of wind effects on buildings and structures. Brussels, Belgium.

ESDU 76001 (1976). The response of flexible structures to atmospheric turbulence. London, UK.

ESDU 79026 (1980). Mean Fluid Forces and Moments on Cylindrical Structures: Polygonal Sections with Rounded Corners Including Elliptical Shapes. London, UK.

Kasperski, M. (1992). Extreme wind load distributions for linear and nonlinear design. Eng. Struct. 14, 27–34.

Pagnini L.C., Solari G. (2001). Damping measurements of steel poles and tubular towers. Eng. Struct. 23, 1085–1095.

Pagnini, L.C., Piccardo, G. (2017). A generalized gust factor technique for evaluating the wind–induced response of aeroelastic structures sensitive to vortex-induced vibrations. J. Fluids Struct. 70, 181-200.

Piccardo, G., Solari, G. (1998). Closed form prediction of 3-D wind-excited response of slender structures. J. Wind Eng. Ind. Aerodyn. 74–76, 697–708.

Piccardo, G., Solari, G. (2000). 3-D wind-excited response of slender structures: closed form solution. J. Struct. Eng. ASCE 126, 936–943.

Piccardo, G., Solari, G. (2002). 3-D gust effect factor for slender vertical structures. Prob. Eng. Mech. 17, 143–155.

Simiu, E. (1973). Logarithmic profiles and design wind velocities. J. Eng. Mech. ASCE 99, 1073-1083.

Simiu, E. (1976). Equivalent static wind loads for tall buildings design. J. Struct. Div. ASCE 102, 719–737.

Simiu, E. (1980). Revised procedure for estimating alongwind response. J. Struct. Div. ASCE 106, 1–10.

Solari, G. (1982). Alongwind response estimation: closed form solution. J. Struct. Div. ASCE 108, 225–244.

Solari, G. (1983). Analytical estimation of the alongwind response of structures. J. Wind Eng. Ind. Aerodyn. 14, 467–477.

Solari, G. (1987). Turbulence modeling for gust loading. J. Struct. Eng. ASCE 113, 1550-1569.

Solari, G. (1988). Equivalent wind spectrum technique: theory and applications. J. Struct. Eng. ASCE 114, 1303–1323.

Solari, G., Pagnini, L.C. (1998). The actions and effects of wind on poles and monotubular towers. CM 4, 29-51.

Solari, G., Pagnini, L.C. (1999). Gust buffeting and aeroelastic behaviour of poles and monotubolar towers. J. Fluids Struct. 13(7-8), 877-905.

Solari, G., Repetto, M.P. (2002). General tendencies and classification of vertical structures under wind loads. J. Wind Eng. Ind. Aerodyn. 90, 1299–1319.

Vellozzi, J., Cohen, E. (1968). Gust response factors. J. Struct. Div. ASCE 94, 1295–1313.

Vickery, B.J. (1970). On the reliability of gust loading factors. Proc. Techn. Meet. Concerning Wind Loads on Buildings and Structures, National Bureau of Standards, Washington DC, 93–104.

4. Vertical slender structures with fixed masses

4.1 Introduction

The full-scale monitoring procedure established in Chapter 2 and the calculation model defined in Chapter 3 find application for a real slender structure with fixed masses. This chapter reports the extensive experimental activity started in 2017 over a light tower in the Harbor of La Spezia (Northern Italy).

After describing the characteristics of the real structure, the chapter shows in detail the design and the construction of the monitoring system. Then, all the parameters required for the calculation of wind-induced response of the light tower (see Section 3.2.4) are accurately investigated intersecting full-scale measurements and experimental surveys. In this respect, the wind tunnel test campaign plays a major role in the chapter for the significance of the results, despite being functional to the calculation. Finally, full-scale measurements are used as a benchmark to assess the capability of the calculation model to predict the real wind-induced response. By applying the model with the measured values of the input parameters, the comparison between measured and calculated response supplies the model error. Then, the uncertainties associated to each input parameter are quantified by varying the parameters one by one, getting them from the calculation model or from current standards and codes.

4.2 Monitoring of a light tower

4.2.1 Description of the case study

The light pole under investigation is located in operative area of the container terminal in the Harbor of La Spezia, Northern Italy (Figure 4.1). It is a 16.6 m high steel pole placed upon the dam, at 2 m above sea level. It is made of two steel polygonal shafts, 5 mm thick, superimposed by slip joints (Figure 4.2a). Each shaft is realized through a lamination and calendering process of steel sheets, with the two edges jointed by a longitudinal welding with throat depth around 1 cm. The base and top diameters are, respectively, 528 mm and 254 mm. The slenderness of the tower is ≈ 40, calculated as the ratio between height and an average diameter.

The cross section is a 16-sides polygon. A weld bead runs along the height of each shaft. A steel ladder, opposite to the welding position, connects the bottom of the pole to the top. At about 10 meters above ground, the ladder is interrupted by an intermediate rectangular platform, with dimensions 0.65 × 1 × 1.1 m. At the top of the pole, a squared platform (1.2 × 1.2 × 1.1 m) houses the lighting equipment and a security camera. The lower portion of the pole is embedded in a 2.5 m high concrete cube (Figure 4.2b), which constitutes an almost perfect clamped end.

4.2.2 Monitoring equipment

The pole has been equipped with a monitoring system including wind speed and structural response sensors. Positions of the sensors are reported in Figure 4.3. A three-axial ultrasonic anemometer is installed on the top platform, 22 m above the ground level. It is supported by a 3 m high steel pole, which in turn is fixed to a strut of the platform (Figure 4.4a). It supplies high-resolution wind velocities, recording the three components of wind speed with a sampling frequency of 10 Hz.

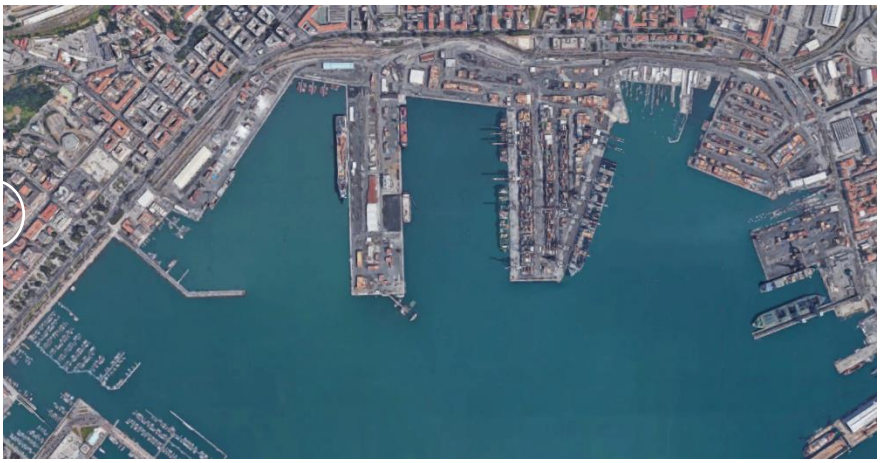

Figure 4.1. Location of the pole in the Harbour of La Spezia.

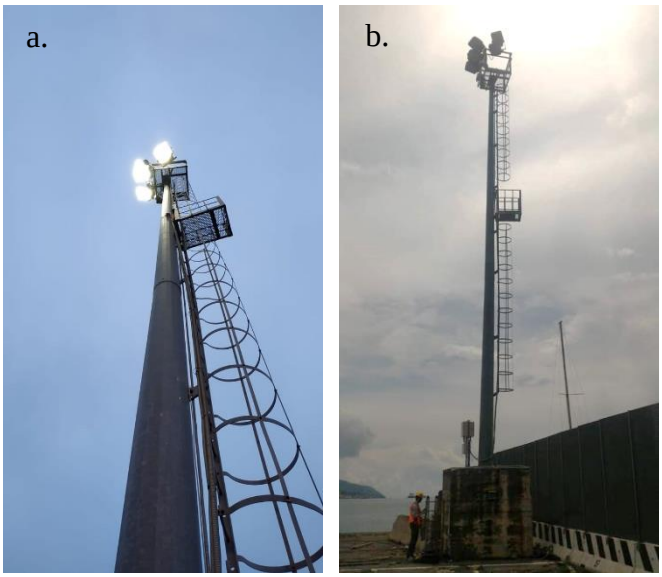

Figure 4.2. The polygonal shafts composing the tower (a), global view of the tower (b).

The structural response is recorded by accelerometers and strain gauges.

Two biaxial MEMS accelerometers record the horizontal accelerations within an operating range of ± 2 g. They are positioned at the top (16.7 m from the base) and at an intermediate level (11 m) of the pole (Figure 4.4b), corresponding to the anti-nodes of its first and second bending modes, as estimated from a prior numerical modal analysis. Accelerations are sampled 200 Hz.

Eight mono-axial half-bridge strain gauges are placed at the base of the tower to investigate the static and quasi-static response of the structure (Figure 4.4c). Two cross-sections are investigated (0.5m and 1.5 m from the base), each one housing four symmetric sensors. Strain gauges measure the nominal vertical strain, enabling to quantify the flexural deformation of the structure in two orthogonal directions. The sampling rate is set to 100 Hz.

Sensors are cable connected to an acquisition unit placed inside a watertight box fixed to the concrete block at the base (Figure 4.5). The acquisition unit includes a data-logger and a mini-pc with a specific software to record data simultaneously from sensors with different sampling rate (Figure 4.6a). Data are exported in ASCII format, with blanks in lower rate columns (Figure 4.6b). The computer can access the Internet through the local area network of the Port. It sends data once per day and warning

messages about its functionality. In order to support continuous operation, the acquisition unit has been equipped with a UPS, to overcome possible power losses, and a ventilation system to limit temperature inside the box.

4.2.3 Modelling

Since no design reports of the light tower were available, a refined laser-scanner survey of the light tower has been carried out to obtain detailed information of the complex geometry of the whole structure (Figure 4.7a, b).

From the laser-scanner outcomes a geometrical 3D model of the light pole has been created (Figure 4.7c) that can be easily exported to specific software for structural analyses.

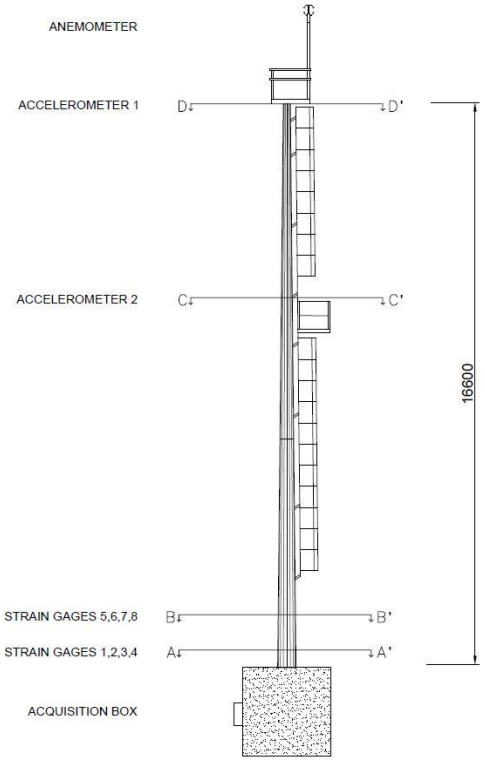

Figure 4.3. Positions of sensors and acquisition unit.

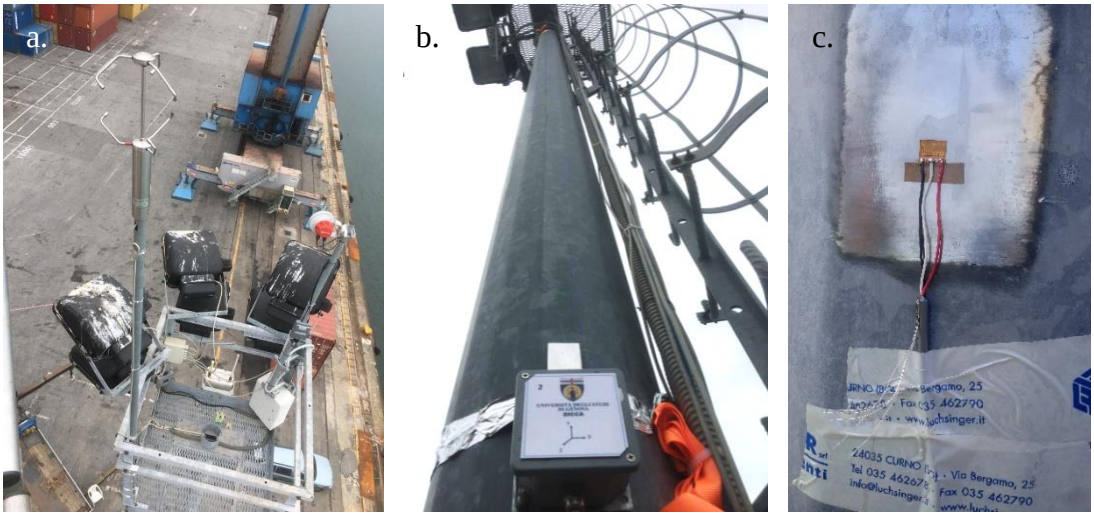

Figure 4.4. Ultrasonic anemometer at top of the pole (a), biaxial accelerometers (b) and uniaxial strain gauges (c).

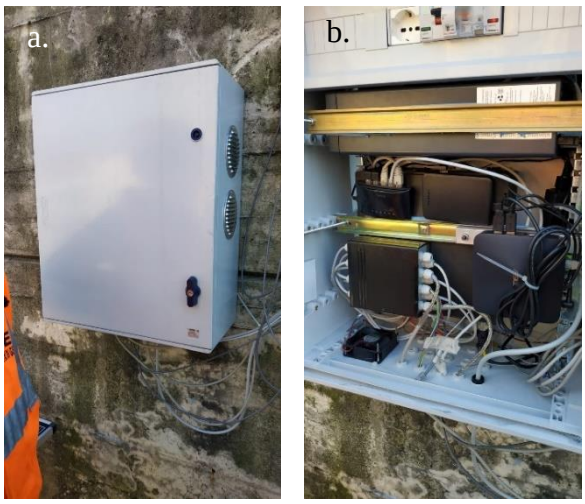

Figure 4.5. Acquisition box on the concrete block (a); inner arrangement of the devices (b).

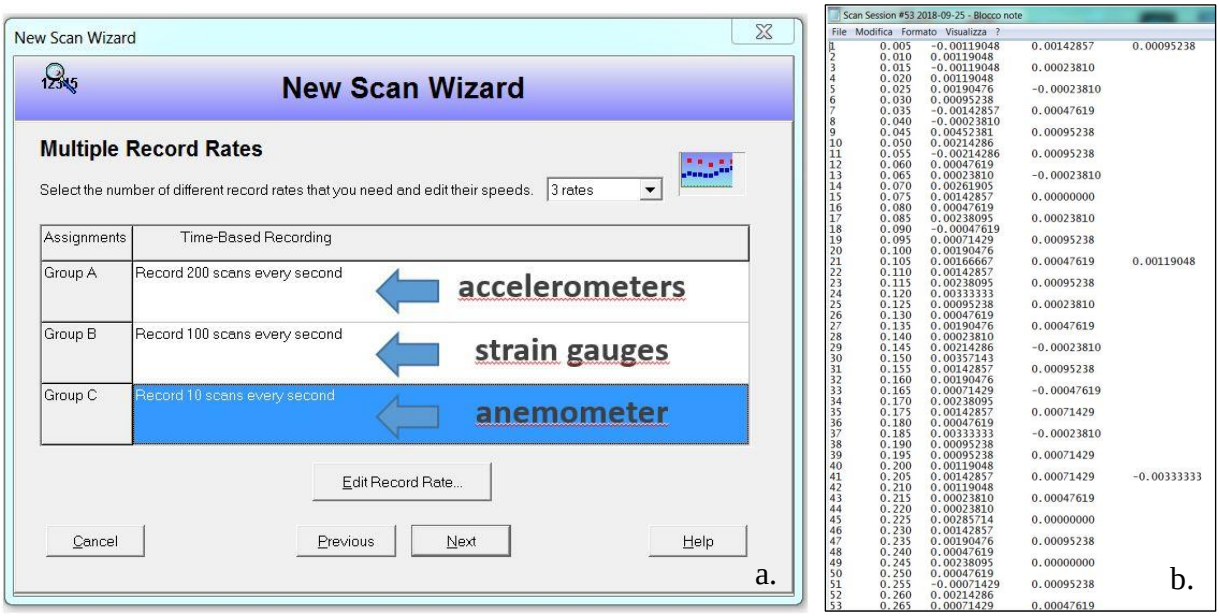

Figure 4.6. Acquisition software enabling different sampling rates (a), data exported to ASCII format (b).

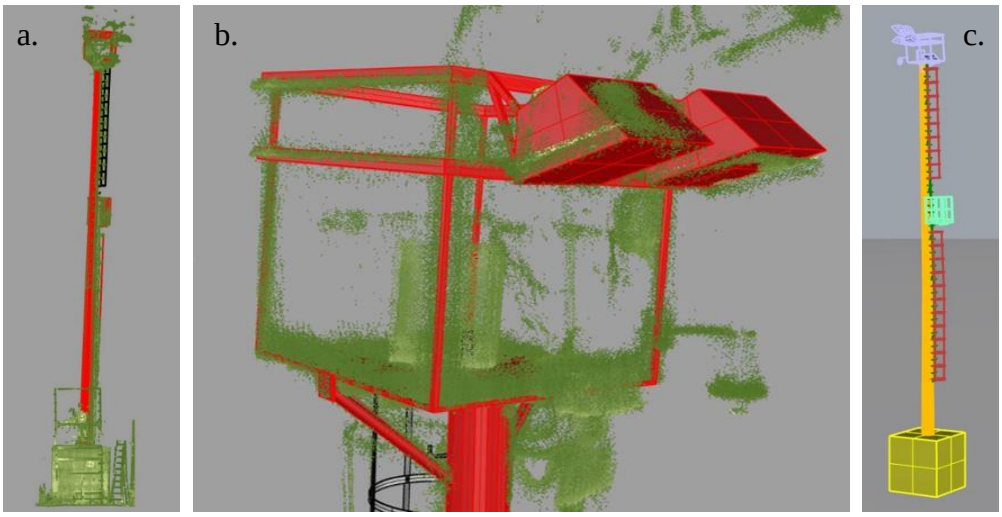

Figure 4.7. Laser scanning of the pole (a) with top platform detail (b) and resulting 3D geometrical model (c).

4.3 Calculation of wind field

4.3.1 Wind velocity components

The tri-axial anemometer at top of the pole provides every 0.1 s the three wind velocity components u_A, v_A and w_A in the instrumental axes x_A, y_A and z_A (z_A is vertical axis). Neglected the vertical components, consistently with the model, wind velocity vector **U** is contained in the horizontal plane (Figure 4.8).

The calculation model requires u and v, which are the horizontal components of wind velocity in x and y direction, respectively (Eq. 3.4). According to the model, the reference frame defined by x and y is determined such that v has nil mean over the time interval T = 10 minutes.

The goal is therefore to find the orientation of x and y in order to decompose wind velocity vector **U** along these axes. Considering 10 minutes of discrete wind velocity values, from the definition of x and y it follows:

$$\sum v_i = \sum U_i \sin(\beta_i - \alpha) = 0 \tag{4.1}$$

where U is the magnitude of **U** (obtained as the vector sum of u_A and v_A), β is the angle between **U** and x_A, and α is the angle between x and x_A, as shown in Figure 4.8. The subscript index i stands for instantaneous value. Expanding the sine function with the angle subtraction formulae, and carrying on the derivation, it follows that:

$$tg(\alpha) = \sum V_i \sin(\beta_i) \Big/ \sum V_i \cos(\beta_i) = \sum v_{Ai} \Big/ \sum u_{Ai} \tag{4.2}$$

from which α can be easily recovered. Once the orientation of the target coordinate system has been obtained, u and v can be calculated by projecting **U** on these new axes.

Because of being installed on the top of the light tower, the anemometric readings are subject to interference with the resonant vibrations of the tower. If the first mode occurs at very low frequencies (i.e. very tall tower), its contribution falls within the harmonic content of wind velocity and thus cannot be filtered out. Therefore, possible interference effect should be always considered. However, in this case the velocity of the vibrating tower is very low (largest motions occur with high periods) and it is negligible with respect to the actual wind speed. No corrections thus have been applied.

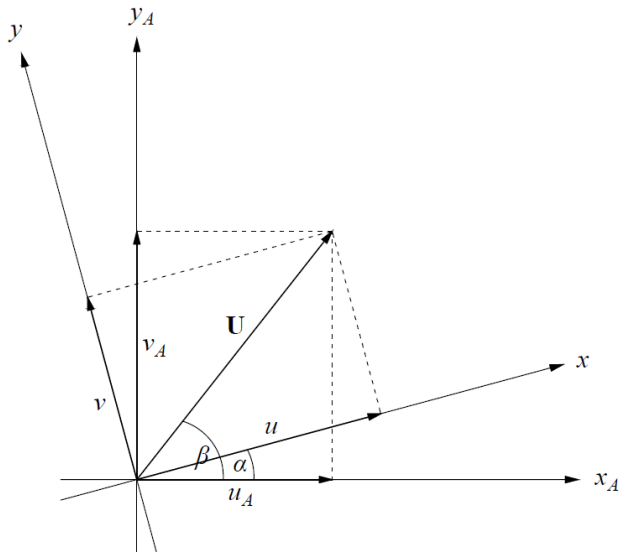

Figure 4.8. Wind velocity components in the horizontal plane.

4.3.2 Mean wind speed profile

The mean wind speed profile $\bar{u}(z)$ is derived starting from the anemometric measurements. First, $\bar{u}(z_{anem})$ is computed as the mean over T= 10 minutes of the velocity component u, with z_{anem} height of the anemometer over ground.

The profile is then calculated according to the calculation model, through the logarithmic law given by Eq. (3.5). The evaluation is carried out by getting z_m from Italian regulations (CNR, 2018), where it is supplied according of the exposition category of the reference site.

Roughness length is provided in a simplified way by current regulations regardless of wind direction. The present study derives this quantity by following the procedure supplied by ESDU 84011 (1993), according to which it is possible to calculate a reference mean speed profile for every wind direction taking into account changes of terrain roughness and topographic effects.

The procedure is applied considering a circular area with radius 20 km centered in the pole location that has been discretized in sectors 20° wide. Every sector has been divided in turn in fetches of uniform roughness (Figure 4.9). Starting from the sequence of consecutive fetch extents and roughness lengths, the reference mean wind speed at a determined height over ground can be estimated. Implementing a code to automatically perform the computation for several heights, the method has allowed to obtain for every wind direction a discrete mean wind profile.

In order to be consistent with the reference formulation, the logarithmic profile that best interpolates the data (from a least squares viewpoint) has been evaluated through a polynomial fitting (Figure 4.10). From the equivalent logarithmic profile z_0 is obtained using Eq. (3.5).

Finally, u_* is computed by scaling the logarithmic profile such that $\bar{u}(z_{anem})$ is equal to the measured value.

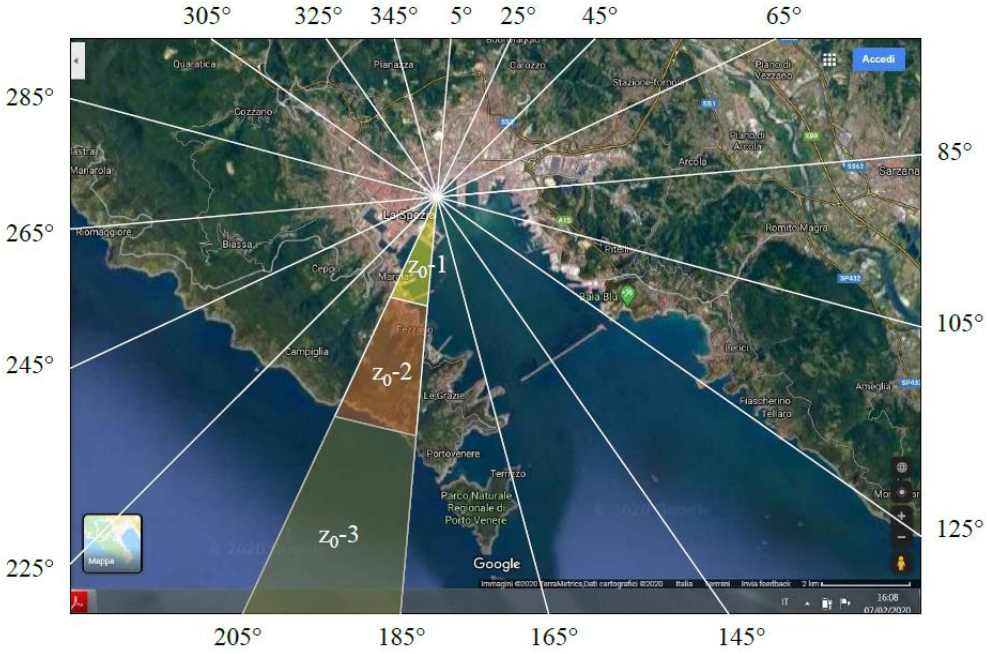

Figure 4.9. Division of the site area in fetches of uniform terrain roughness, according to ESDU 84011.

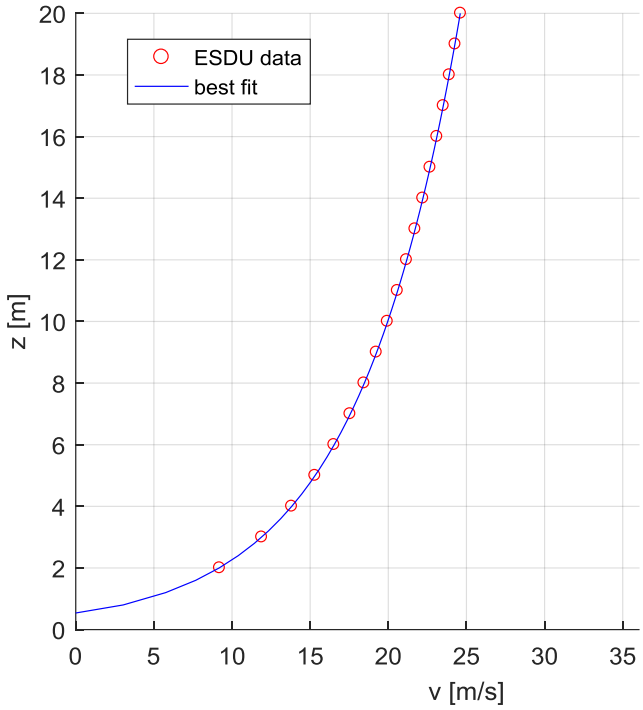

Figure 4.10. Evaluation of z_0 through polynomial fitting of reference velocities calculated according to ESDU 84011.

4.3.3 Turbulence

Turbulence intensity $I_\varepsilon(z)$ is evaluated starting from the anemometric measurements too. First, σ_ε is computed as the standard deviation over T=10 minutes of the velocity component ε (ε=u,v) measured by the anemometer. Then, turbulence intensity it is calculated according to Eq. (3.6), where σ_ε is considered invariant with z.

Turbulence integral length scale $L_\varepsilon(z)$ is directly evaluated from Eq. (3.7), depending only on z_0.

4.4 Aerodynamic coefficients – Wind Tunnel tests

4.4.1 Literature review

The flow properties around bluff bodies have attracted extensive research in the last century. The parameters that drive the aerodynamic behaviour of bluff cylinders are the drag coefficient C_D, the lift coefficient C_L and the Strouhal number St, which are closely associated with the vortex shedding dynamics and are evaluated paying special attention to their dependence of Reynolds number Re.

A vast amount of research has been focused on the flow around stationary circular cylinders; see Roshko (1955), Coutanceau & Daefaye (1991), Williamson (1988, 1996), Zdravkovich (1997), Thompson et al. (2001) and Yeung (2010) among others.

The flow around polygons is much less studied. The most of the studies on polygonal cylinders are for squares and rectangles; significant studies were made by Okajima (1982), Igarashi (1997), Matsumoto (1999), Breuer et al. (2000), Mills et al. (2003), Zhou et al. (2005), van Hinsberg et al. (2017, 2018).

On the contrary, only little attention has been paid in literature to the study of the flow around polygonal cylinders with more than 4 sides, even if such sectional shapes are commonly seen in many

engineering problems. Structures like light poles, tubular towers or wind turbines are mostly characterized by polygonal shafts with more than 12 sides. As regards these kinds of polygonal cross-sections, there has been no systematic experimental investigations and relevant measurements are scarce.

Research on this topic is therefore lacking and fragmented. Wind tunnel tests are still rare and do not supply reliable benchmark. An extensive experimental campaign about polygons with a large edge number has been conducted by James (1976). He measured the drag coefficient of polygonal sections with 8, 12 and 16 sides as a function of Reynolds number and corner radius, considering 3 different mean directions of the flow. Mehta et al. (1990) and Bosch & Guterres (2001) run wind tunnel tests over octagonal cylinders to verify the drag coefficients proposed in 1985 by AASHTO for highway support structures. Tian and Li (2007) investigated a polygonal cylinder with 24 sides in a low-speed wind tunnel to seek a low drag solution for their prototype supporting frames. Xu et al. (2017) systematically studied the wake of polygons with edge number from 3 to 16 through wind tunnel tests: they measured the aerodynamic parameters for two different orientations of the cylinders.

There have been attempts to simulate numerically the flow around a polygonal cylinder with more than 4 sides. Tian & Wu (2009) calculated the flow field around polygons at the corner orientation for even values of the edge number. Khaledi & Andersson (2011) investigated numerically the unsteady wake behind a hexagonal cylinder both corner and face oriented. However, the numerical works mentioned are inevitably limited to *Re* lower than that typically seen experimentally.

Two main shortcomings emerge from a review of the research papers dealing with many-sided polygons. First, a very poor characterization of the lift coefficient. Second, the study of the flow past polygons is almost entirely limited to one or two main orientations (mean flow direction aligned with corner or orthogonal to face). Therefore, there is no information about the trend of the aerodynamic coefficients as a function of the flow mean direction. Consequently, a reliable quantification of the aerodynamic derivatives is impossible for such kind of cross-sections.

Due to the lack of information, the engineering design of polygonal cylinders with a high number of edges is often dealt with using information available for circular cylinders, as appears from an analysis of current regulations. The Italian standard provided by CNR (2018), for example, furnishes the aerodynamic parameters for polygonal shapes up to 12 sides. Sections with higher side number are considered to be circular. Similarly, in Eurocode 1 (2005), sections with more than 12 sides are neglected (e.g. 14 sides) or treated as circular cylinders (e.g. 16 sides). The standard provided by ASCE (2002) stops at octagons. ESDU 79026 (1980), provides a method to derive the drag coefficient for sections up to 20 sides, by approximating polygons to circles with an equivalent roughness. On the same principle, ESDU 96030 (1998) supplies *St* values that are valid for both circular and polygonal sections with edge number greater than 8.

All these recommendations rely on a polar-symmetry of the cross-section to characterize the aerodynamics of a polygon, thus neglecting some aspects that can become very important in the structural behaviour. First, the coefficients provided are usually referred only to one mean direction of the flow, which is aligned to a symmetry axis of the section (generally the one aligned with a corner). Consequently, the mean lift force is always considered to be zero, as well as the lift derivative with respect to the angle of attack C'_L. Therefore, mean crosswind buffeting response and galloping are neglected for slender structures with these kinds of polygonal shafts. It is also important to notice that, among the mentioned regulations, only ESDU takes into account the influence of the corner radius on the aerodynamic behaviour of polygonal cylinders with more than 4 sides.

In addition to the shortages described, the aerodynamic contribution of distributed elements such as the welding or the external ladder, which very often recur in poles and monotubular towers, is dealt with neither in current regulations nor in scientific papers. With regard to localized masses such as rest platforms or lighting equipment, although there are some specific studies, the variety is so wide that is practically impossible to generalize the results.

For these reasons, the following sections describe the wind tunnel tests carried out on scale models of the light tower to investigate its aerodynamic properties. The study aims to address the described issues by investigating C_D, C_L and St, paying attention to highlight how the aerodynamic behaviour is affected by Reynolds number, flow direction, corner radius and ancillaries.

4.4.2 The scale models

Models of different typology have been realized to investigate the aerodynamic properties of the pole. A 3D model of the top platform, 1:5 scale, reproduces all the equipment at the top of the tower: the metallic frame, the spotlights and the security camera (Figure 4.11a).

Two sectional 1:8 scale models of the shaft have been realized from 3D printing (Figure 4.11b-c). They represent top and bottom segments of the 16-sides shaft, in the following referred to Model A and Model B, reproducing all the geometric features of the real structure: the rounded corners, the welding and the external ladder. The removal of the ladder also makes it possible to appreciate its contribution on the aerodynamic behaviour of the pole.

Both models have smooth surface. They are 1.8 m long; the diameter is 35 mm (Model A) and 62.5 mm (Model B). The corner radius is equal in both models (3 mm) as it is in the real structure. Therefore, for model A the ratio of the radius over the diameter (r/D) is equal to 0.05; for model B is 0.09.

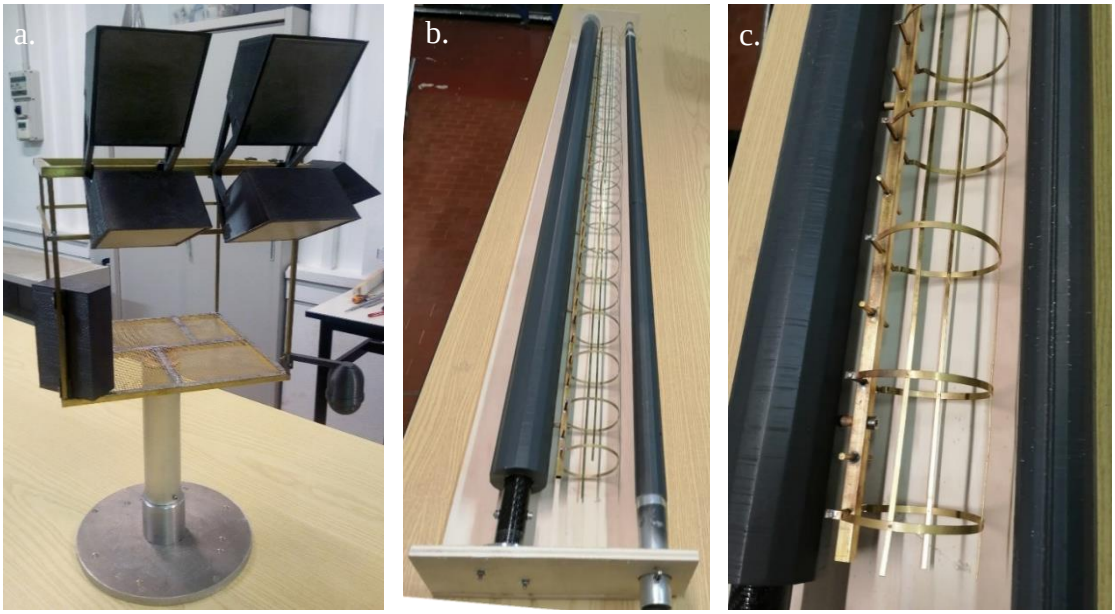

Figure 4.11. The wind tunnel models: 3D top model (a) and sectional models (b), with model B and model A from left to right. Ladder, welding and rounded corners in detail (c).

4.4.3 The experimental setup

The tests have been carried out in the wind tunnel facility at the Department of Civil, Chemical and Environmental Engineering of the Polytechnic School of the University of Genoa. It is a closed-loop subsonic wind tunnel for aerodynamic and civil experiments. The test chamber has a cross section with dimension 1.7 × 1.35 m^2 (width × height) and length 8.8 m, with a 1.3 m diameter turntable. It is equipped by a pitot tube to measure the undisturbed wind speed (placed 0.25 m below the wind tunnel roof, outside the wall boundary layer) and a fast-response multi-hole probe (Cobra probe) managed through a robotic arm to measure wind velocity profiles or wake properties. The wind tunnel has two test sections, one for 3D models and one for sectional models. In both test sections, flow uniformity is below 1% and longitudinal turbulence intensity is below 0.2% in smooth flow conditions.

The goal of the tests is the evaluation of the aerodynamic coefficients of the sectional models that are involved in the reference calculation model, namely the mean force coefficients (drag coefficient, C_D, and lift coefficient, C_L) and the Strouhal number St:

$$C_i = \frac{\overline{F}_i}{\frac{1}{2}\rho \bar{u}^2 A_{ref}} \qquad i = D, L \tag{4.3}$$

$$St = \frac{f_{sh} D}{\bar{u}} \tag{4.4}$$

where $\bar{u}$ is the reference mean wind velocity, A_{ref} is the reference area of the model, ρ is the air density, D is model diameter, f_{sh} is the vortex shedding frequency and $\overline{F}_D$, $\overline{F}_L$ are the time average of drag and lift force.

The 3D model has been mounted on a six-component force balance linked to the turning table. The system is composed by six SMT S-Type load cells, which are properly arranged to detect the three wind loads (longitudinal and lateral force and yawing moment), and, on the other hand, to guarantee the necessary stiffness required for such tests. Figure 4.12a shows the six-component force balance assembled.

Due to the presence of sharp edges, the aerodynamic properties of the 3D model have been considered to be independent of flow characteristics (Buresti, 1987); therefore, the top model has been tested only in smooth flow, varying flow velocity and angle of attack of the flow.

A dense and a sparse grid consisting of wooden square bars have been used to test the sectional models both in smooth and in turbulent flow (Fig. 4.13). Placing the grids upstream of the model, two turbulence levels have been generated at the test section, characterized by longitudinal turbulence intensity I_u equal to 7.5% and 3.5%, respectively, and integral length scale L_u equal to 50 mm and 25 mm.

With regard to the sectional models, the aerodynamic forces have been measured by two quartz six-component dynamometers at either end of the model. The force balances are mounted on two high precision stepper motors rotating the model automatically with 0.05° sensitivity (Fig. 4.12b). The stepper motors are in turn connected to a steel frame, bolted to the concrete floor slab, which acts to eliminate the flow-induced cylinder vibrations. The static setup requires the sectional models to be longer than the width of the test chamber; consequently, the three-dimensional effects due to the cylinder ends are mitigated.

The experimental campaign over the sectional has been divided in three sets of tests, each one with a different objective. They are summarised in Table 4.1.

The first set of tests (Set n°1) aims to investigate the aerodynamic behavior of the hexadecagonal cross-section without ancillaries. One targeted sector only has been explored, keeping the longitudinal welding on the leeward surface, in order to minimize its aerodynamic contribution. The considered sector is from 0° to 22.5° (Figure 4.14), starting and ending with the mean flow direction perpendicular to a face of the model. The flow directions have been investigated in steps of 2° except in the neighbourhood of the corner, where a 1.25° step has been used. Both sectional models have been tested, both in smooth and in turbulent flow conditions, and varying the motor frequency to investigate several velocities. Mean flow velocity has been varied approximately from 11 to 22 m/s. Therefore, the *Re* range is $\approx 3 \cdot 10^4 : 10^5$.

The second run of tests (Set n°2) investigates the contribution of the welding varying the angle of attack from 0° to 360° with a step of 5.625°. In this case, tests have been carried out on model B, at different turbulence levels but with fixed motor frequency.

The third testing set (Set n°3) investigates the model (Model B) equipped with the ladder. The angle of attack has been varied from 0° to 360° in steps of 11.25°. Tests have been carried out in smooth flow at a set wind speed value.

The definition of the angle of attack α is shown in Figure 4.14. It is timely to note that α=11.25° identify a symmetry axis of the configuration without the ladder. For both 3D and sectional models, blockage ratio is less than 5%, thus no corrections have been applied to the results. The duration of each test is 60 s. The transducer measurement signals are sampled at 2 kHz.

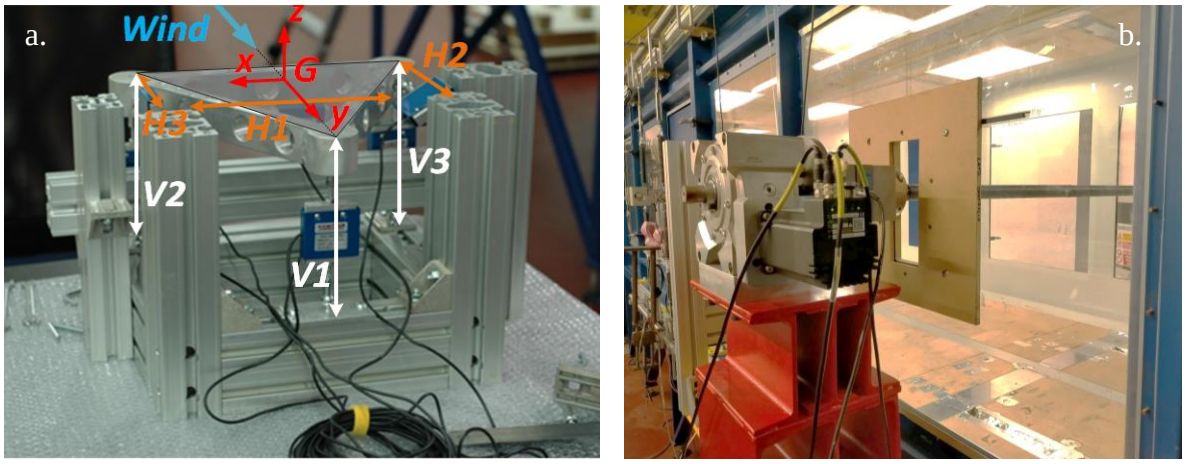

Figure 4.12. Force balances for testing the 3D model (a); force balances on stepper motor for testing the sectional models (b).

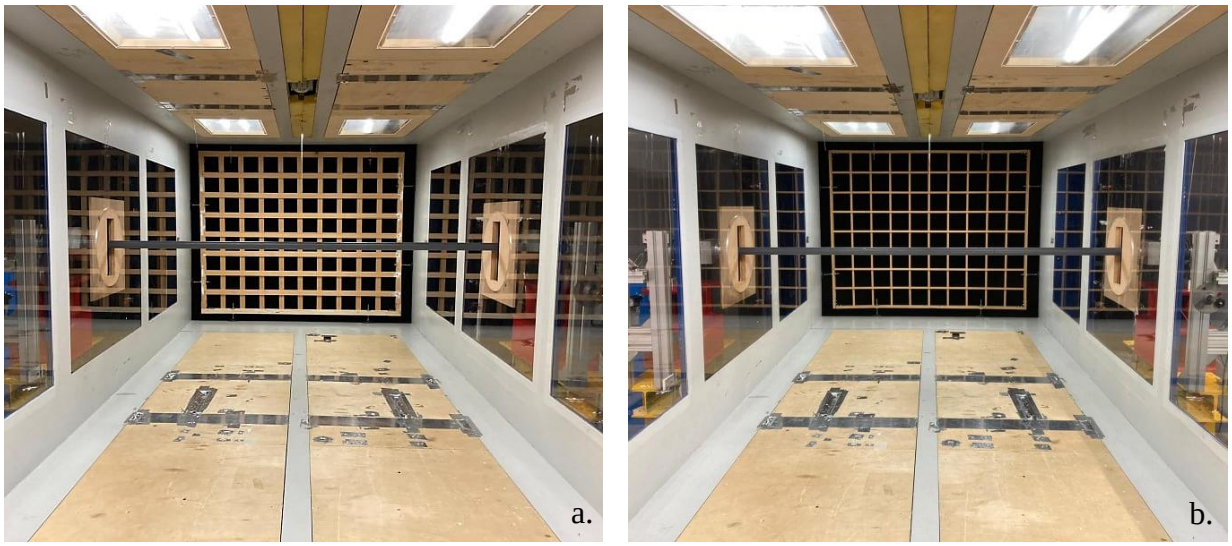

Figure 4.13. Wind tunnel inside-view with turbulent flow conditions. Dense grid (a) and sparse grid (b).

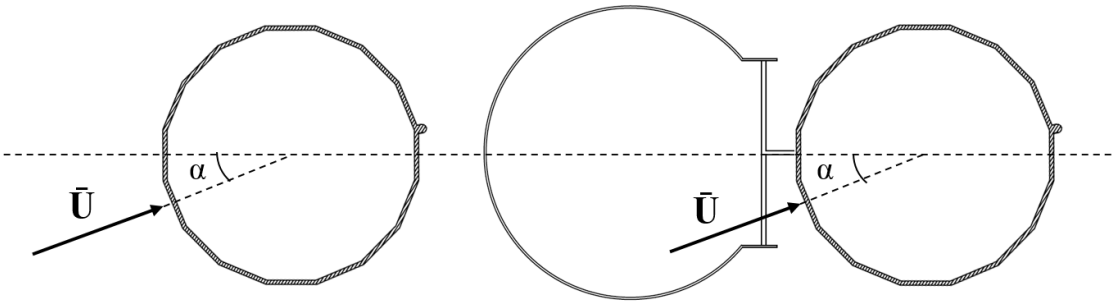

Figure 4.14. Definition of the angle of the mean flow direction, with and without ladder. In the picture α=22.5°.

Table 4.1. Division of wind tunnel tests on the sectional models.

Set number	Angles of attack (°)	Turbulence Intensity (%)	Motor freq. (Hz)	r/D	Ladder
1	0:2:10, 11.25, 12.5:2:22.5	0.2, 3.5, 7.5	25:5:40	0.05, 0.09	No
2	0:5.625:360	0.2, 3.5, 7.5	25	0.05	No
3	0:11.25:360	0.2	25	0.05	Yes

4.4.4 3D model results

The static tests over the 3D model have determined the contribution of the top platform to the total aerodynamic force on the pole. To evaluate only the forces on the platform, excluding the contribution of the supporting cylinder, the support has been shielded in order not to transmit any loading to the balances (Figure 4.15).

The resulting mean force coefficients are reported in Figure 4.16, where they have been evaluated with flow velocity equal to 11 m/s. The little physical asymmetries of the platform affect the coefficients as the drag is not perfectly symmetric and the lift is definitely not skew-symmetric. The drag coefficient undergoes small variations in the directional domain (from 0.8 to 1.2) oscillating around 1, while the lift is always close to zero; therefore, with regard to alongwind and crosswind actions, the platform practically behaves like a flat screen. However, the results suggest the both

vertical and torsional actions are not negligible and thus should be taken into account for some wind directions.

Finally, the tests have been repeated increasing flow velocity to about 17 m/s, in order to investigate possible Reynolds effects. The results almost perfectly replicate the previous ones (Figure 4.17) showing independence of *Re*, as we expected from a bluff body with sharp corners.

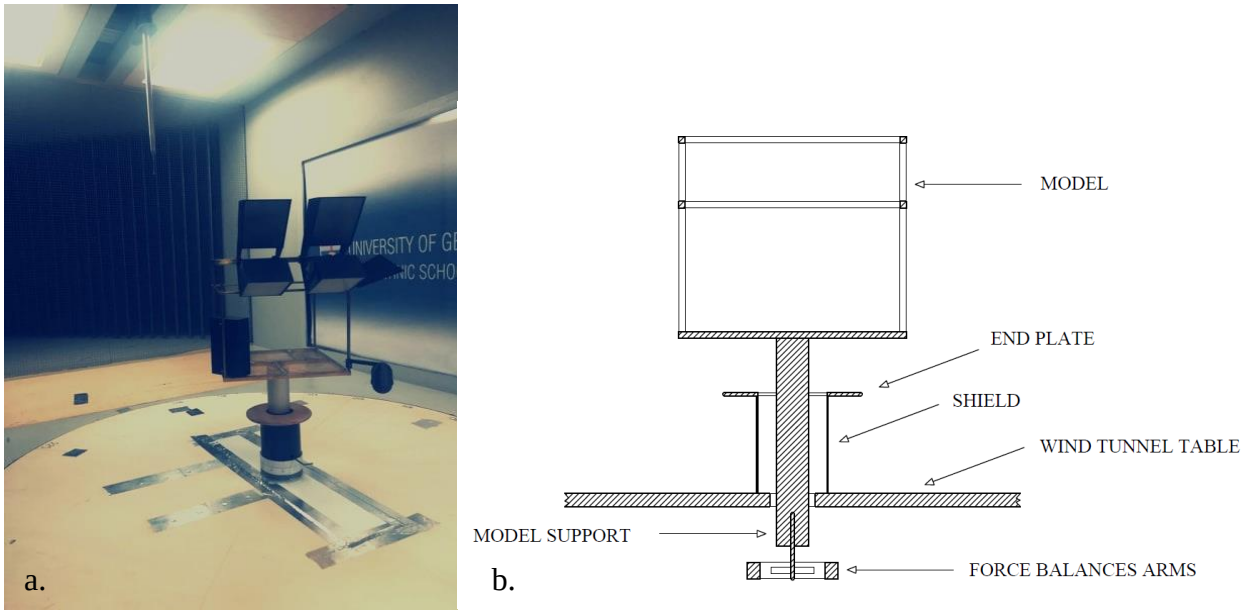

Figure 4.15. Static test setup of the 3D top model (a). The lower portion of the model is shielded not to consider its contribution to the aerodynamic forces (b).

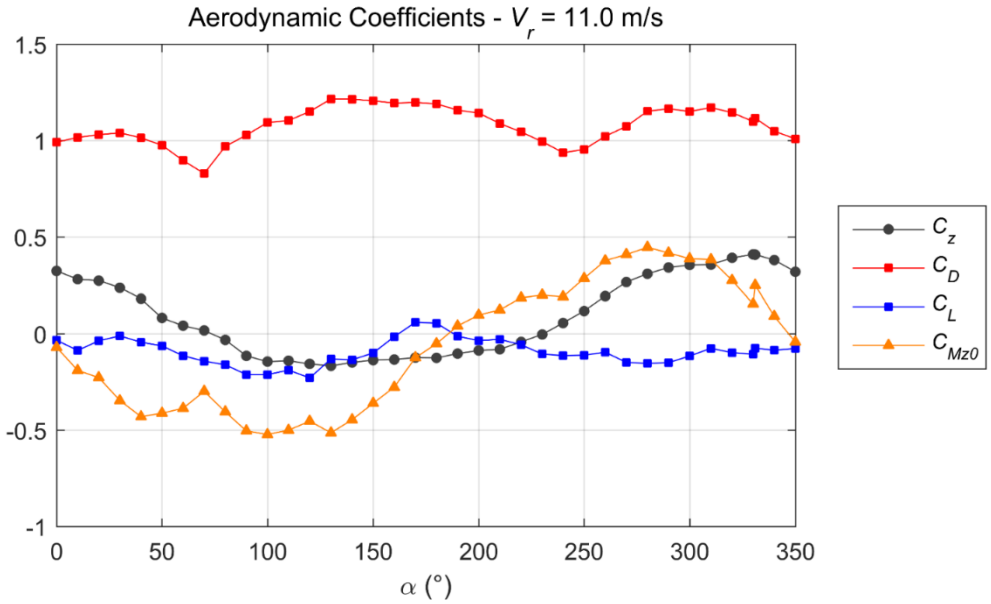

Figure 4.16. Mean force coefficients as a function of the angle of attack, with motor frequency 25 Hz.

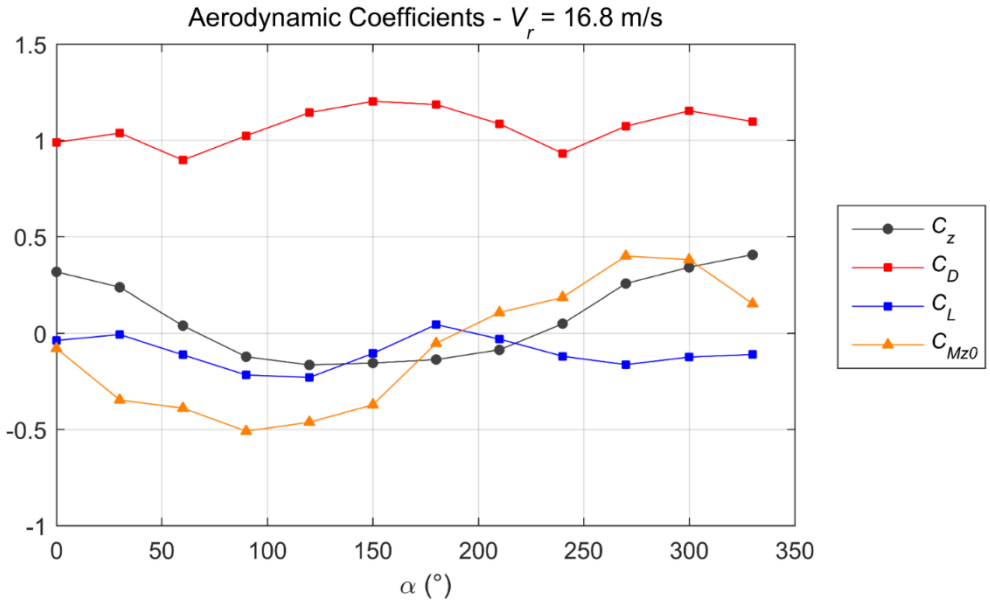

Figure 4.17. Mean force coefficients as a function of the angle of attack, with motor frequency 30 Hz.

4.4.5 Sectional models results

4.4.5.1 Role of the angle of attack

Set n°1 aims to characterize the aerodynamic behaviour of a hexadecagonal cylinder. In particular, this section discusses the aerodynamic coefficients of model B as a function of the angle of attack of the flow. Figure 4.18a plots the drag coefficient obtained from the tests performed in smooth flow (I_u < 0.2%), at different wind speeds (i.e., different *Re*). In the figure, the symmetry axis of the model is shown at 11.25°; in this condition, the longitudinal welding is exactly opposite to the stagnation point and its influence on the results should be almost irrelevant.

First, from the drag diagram it is evident that, increasing flow velocity, the cylinder is entering the critical regime characterized by the drag crisis. Indeed the drag reduces of a 40-50% changing *Re* from 5.6 to $9.1 \cdot 10^4$. In addition, the physical symmetry is reflected in the figure: the drag coefficient has an almost symmetric trend, and the little asymmetries, increasing at high *Re*, can be justified by the instability that characterises the critical regime, where even minimal defects of the model or of its orientation can result in huge variations.

Finally, it is timely to highlight the influence of the angle of attack on the drag. The drag variation in the directional domain is 15% in the sub-critical range (black line) up to 25% at the maximum *Re* (light grey line).

With regard to the lift coefficient, Figure 4.18b, some interesting aspects arise. The four plots converge to zero at 11.25°, which is the symmetric configuration where the corner is aligned with the mean flow direction. This result therefore confirms that the model reproduces the physical symmetry of this layout. Instead, moving from α=11.25° towards α=0° and α=22.5°, where the mean flow direction is perpendicular to a side of the cross-section, we find that the lift assumes a considerable negative value, despite the theoretical symmetry of this layout, too. This means that, either some larger uncertainties affect the reproduction of the face-orientation, or the welding plays a role, even if it is kept downstream.

Notable results concern maximum and minimum lift in this directional domain. Despite being neglected by current standards, the mean lift coefficient assumes remarkable positive and negative

values, being up to the 40% of the drag, confirming the results obtained by James (1976). At the lowest flow velocity, which falls into the sub-critical Reynolds range (black line), the lift curve is fairly skew-symmetric (except the last two values, at 20° and 22.5°), and its maximum and minimum values are located halfway between the two symmetric configurations (corner-orientation and face-orientation).

Entering the critical Reynolds range, the lift curve gradually deviates from the expected skew-symmetrical trend, lowering as velocity increases. In addition, the maximum and minimum lift occur closer to the corner configuration. This result proves the high instability characterizing the critical regime in smooth flow conditions.

Figure 4.19 shows the results of the tests on model B performed at a fixed wind tunnel motor frequency (25 Hz) varying turbulence intensity from 0.2% to 7.5%. The presence of grids of increasing thickness consequently causes a slight decrease in the flow mean speed, which decreases by 10% with the sparse grid (I_u=3.5%) and by 20% with the dense one (I_u=7.5%). Figure 4.19a shows that turbulence produces a so-called *equivalent Reynolds effect* on the drag coefficient, which decreases considerably as turbulence increases.

Figure 4.19b shows that it plays an even stronger role on the lift coefficient, which changes sign until it assumes almost specular values. This effect will be detailed in section 4.4.5.3. In addition, it is important to highlight the different influence of turbulence with respect to velocity (Figure 4.18b) on the lift. Despite entering in the critical range, the three lift curves in 7b are still almost skew-symmetric except for the last two angles. The fact that the curve of the maximum turbulence level (light grey), which in section 4.4.5.3 will be seen to be in the post-critical range, is perfectly skew-symmetric demonstrates that some small imperfections regarding the configuration around 22.5° become significant in the critical range.

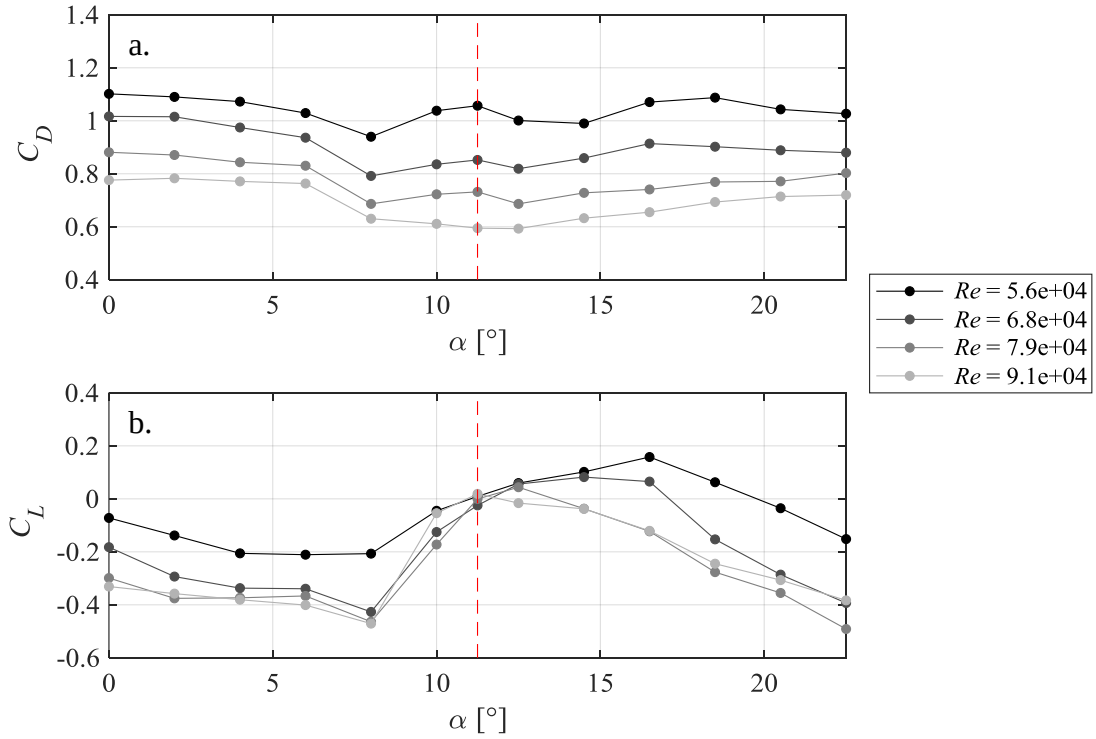

Figure 4.18. Mean drag (a) and lift (b) coefficients as a function of the angle of attack, in smooth flow (I_u<0.2%) and different mean flow velocities. Corner radius r/D=0.05.

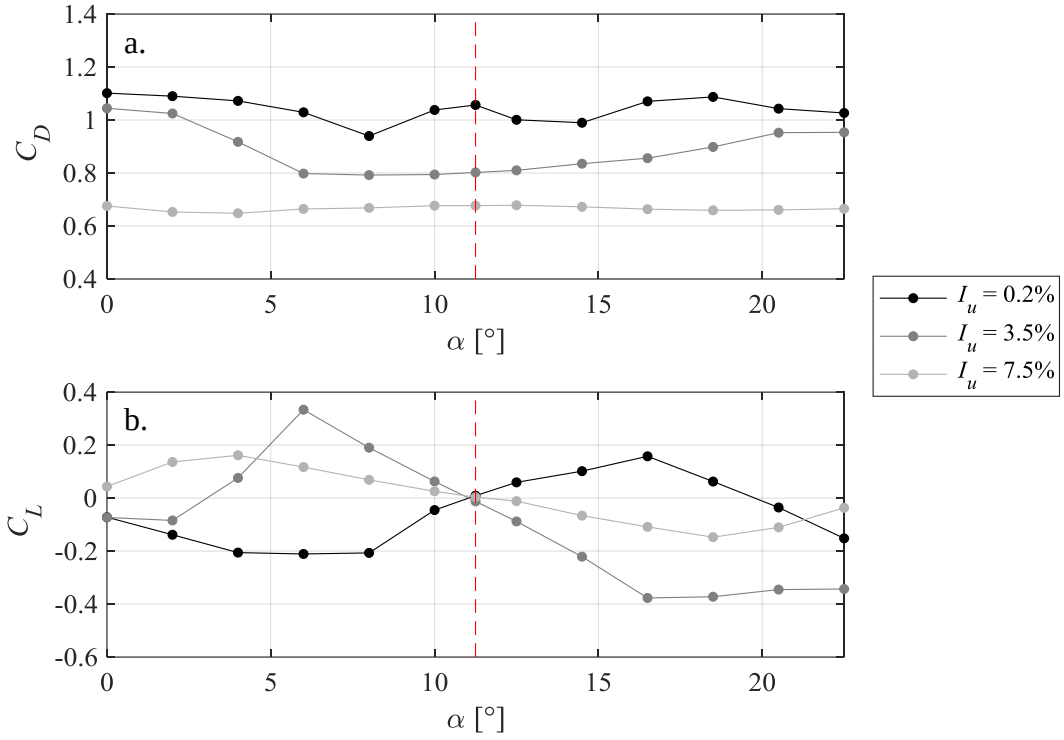

Figure 4.19. Mean drag (a) and lift (b) coefficients as a function of the angle of attack, with fixed motor frequency (25 Hz) and different turbulence intensities. Corner radius *r/D*=0.05.

4.4.5.2 Role of corner radius

The role of the corner radius on the aerodynamic behaviour has been investigated by comparing the results obtained on model A (*r*/*D* =0.09) and model B (*r*/*D*=0.05). Figure 4.20 shows the mean drag (a) and lift (b) coefficient obtained in smooth flow with different wind tunnel motor frequencies as to keep *Re* of the two models as close as possible (5.2 and $5.6 \cdot 10^4$) and in the sub-critical range.

The increase of corner radius makes the cross-section closer to a circle from an aerodynamic viewpoint, regularizing the trend of both coefficients. In particular, the lift coefficient is much closer to zero, and becomes zero in the three symmetry configurations, i.e., α=0°, α=11.25°, α=22.5°. Considering that the weld is more pronounced in the small model (Model B), the results suggest that the negative lift of the large model at face-orientation shouldn't be ascribed to the presence of the longitudinal welding along the cylinder.

4.4.5.3 Role of Reynolds number

This section analyses the role of Reynolds number in the aerodynamic behaviour of the hexa-decagonal cross-section. Results about both the large and the small model, as well as tests both in smooth flow and at the two considered turbulence levels, are reported on the same diagrams.

Following the procedure described by ESDU 79026 (1980), the effect of turbulence is considered in equivalent terms by defining a turbulence factor f_T; results are then presented both as a function of effective Reynolds number $f_T Re$ and as a function of *Re*. The factor f_T varies as a function of the effective roughness of the cylinder. For polygonal sections, the effective roughness is evaluated based on the side number and the corner radius. Only polygons with a smooth surface are considered for the evaluation of f_T.

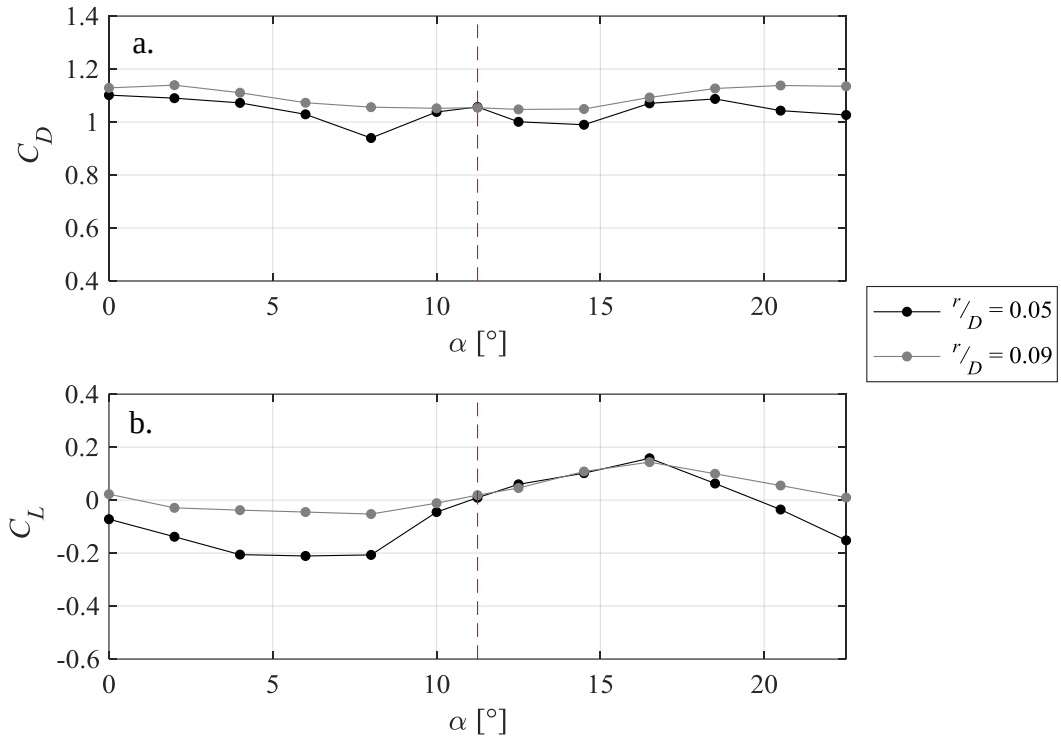

Figure 4.20. Mean drag (a) and lift (b) coefficients as a function of the angle of attack, with smooth flow (I_u<0.2%) and different corner radius. Re=5.2:5.6·10^4.

Figures 4.21-4.22 show the Reynolds effect on drag and lift force coefficient, respectively. Three main configurations are investigated: face-orientation (α=0°, Fig. 4.21a, 4.21d, 4.22a, 4.22d), corner-orientation (α=11.25°, Fig. 4.21b, 4.21e, 4.22b, 4.22e) and an intermediate one (α=6°, Fig. 4.21c, 4.21f, 4.22c, 4.22f).

Figure 4.21 investigates the drag coefficient. The outcomes of the present campaign are compared with significant results reported by the literature. Results obtained by James (1976) are taken as a reference; these tests were performed in smooth flow, at fixed corner radius (r/D=0.12) and investigated the same three orientations. Even if he presented the results as a function of Re, in smooth flow f_T =1 and the effective Reynolds number coincides with Re. In addition, the values proposed by ESDU 79026 for the hexadecagonal shape are included in the figure. It is timely to say that these curves should relate only to the corner-orientation, which according to ESDU should produce the maximum aerodynamic force. Indeed, the curve proposed by ESDU is a conservative one, derived from James' investigations, which the structural designer should use independently of the orientation of the cylinder.

The results shown by Figures 4.21a, 4.21b, 4.21c confirm that the curve proposed by ESDU comprehends all the measurements in conservative terms. The highest agreement between the curve proposed by the standards and the results of this campaign is obtained at α=0° (flow perpendicular to face, Figure 4.21a), where also the highest values of the drag are obtained, as it was found also by James. Therefore, the results show that the corner-orientation does not produce the maximum drag force.

A good agreement is found for every orientation between the drag coefficients measured in smooth flow and the results from James, even if only the first part of the critical range is addressed by our test in smooth flow.

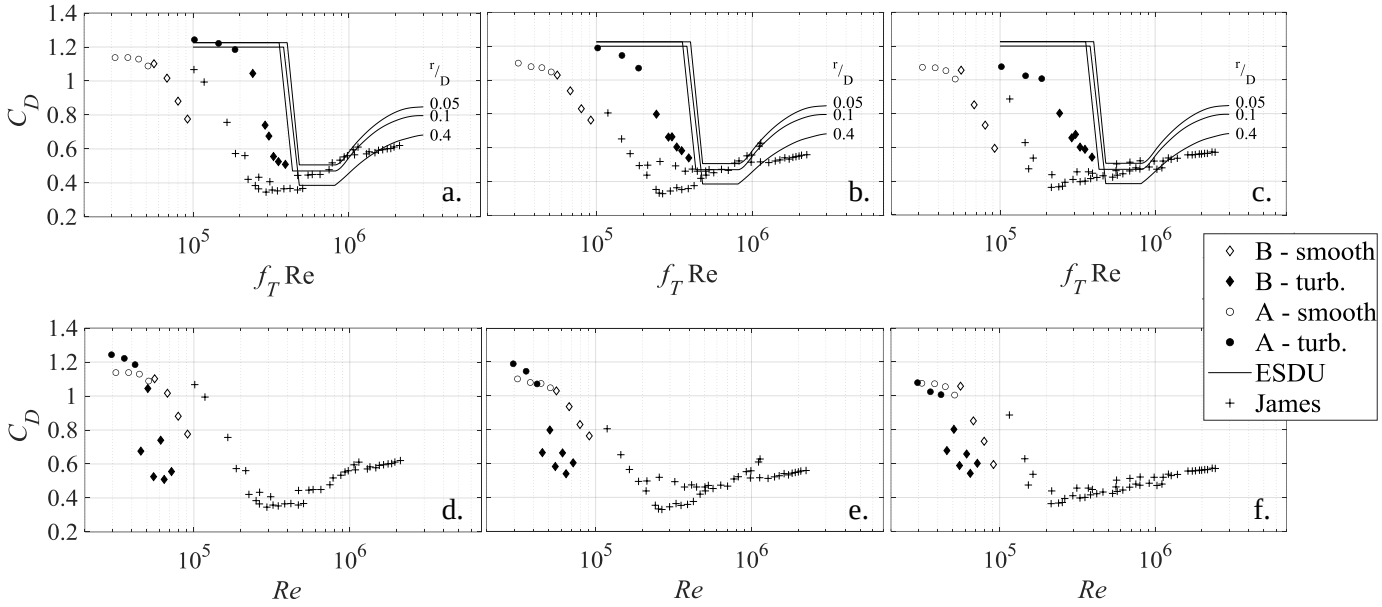

Figure 4.21. Mean drag coefficient as a function of effective Reynolds number (a, b, c) and as a function of Reynolds number (d, e, f). The angle of attack of the flow is α=0° (a, d), α=6° (b, e), α=11.25° (c, f).

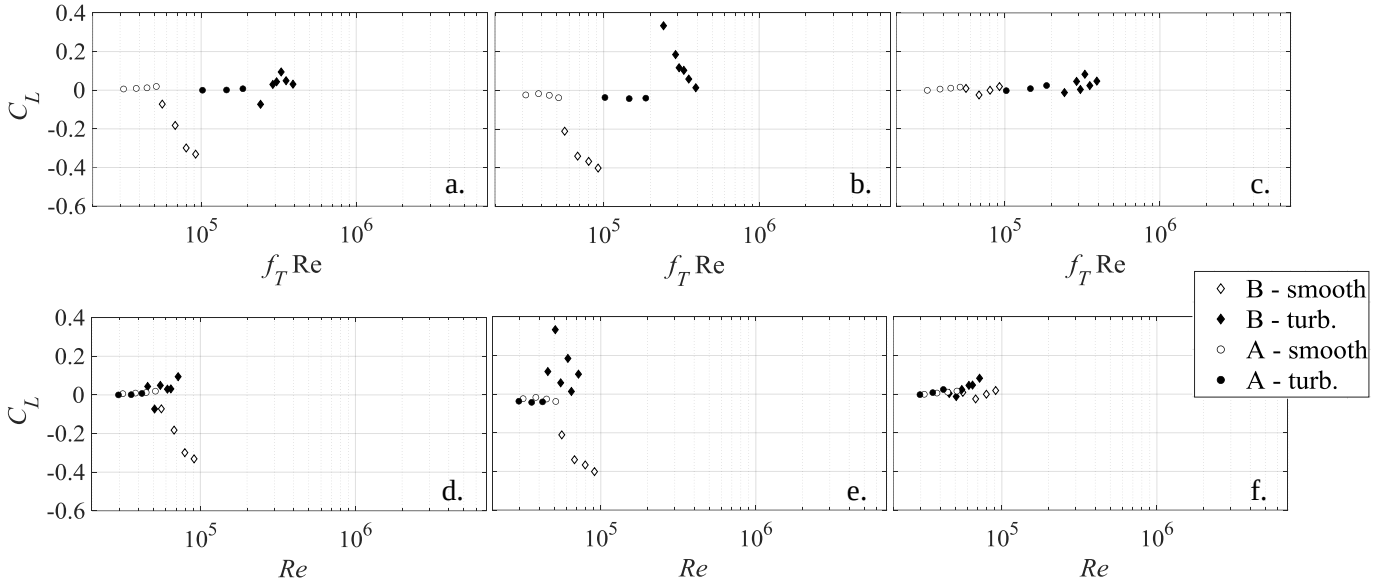

Figure 4.22. Mean lift coefficient as a function of effective Reynolds number (a, b, c) and as a function of Reynolds number (d, e, f). The angle of attack of the flow is α=0° (a, d), α=6° (b, e), α=11.25° (c, f).

The most impressive result emerging from Figures 4.21a, 4.21b, 4.21c is a clear separation into two branches between turbulent (full symbols) and smooth tests (void symbols). Turbulent-flow results are artificially translated in a separate Reynolds range because of f_T, which is approximately 1 in smooth flow but can be up to 7 in the examined turbulent conditions. However, if we present the results as a function of *Re*, data in the different flow regimes get closer but lose some alignment (Fig. 4.21d, 4.21e, 4.21f). Therefore, the present campaign suggests that a better definition of a quantity representative of turbulence effect on the drag should be considered.

Figure 4.22 show the results of the lift coefficient. In this case, values measured on the two models (circles and diamonds for model A and B, respectively) should be read separately, because the change of shape changes completely the extent of the transversal force.

At corner orientation (α=11.25°, Figure 4.22c, 4.22f), as described in the previous sections, the symmetry of the configuration is perfectly represented by both models. Therefore, the lift coefficient is essentially zero regardless of Reynolds number. At the mid-orientation (α=6°, Figure 4.22b, 4.22e) the model is asymmetric with respect to the flow and thus we find the highest lift both of model A (circles) and model B (diamonds). At face-orientation (α=0°, Figure 4.22a, 4.22d) some imperfections affect the symmetry of model B. Indeed, while values of model A recall the trend of the corner-orientation, model B undergoes a considerable lift force.

The effect of the asymmetries, both intentional or due to defects, is amplified in the critical regime; indeed for each orientation the maximum lift is reached in the middle of the critical range. In addition, as previously mentioned, the lift evolves non-monotonically along with $f_T Re$, with an abrupt change of sign when turbulence is applied. Actually, it happens that the position of the horizontal bars of the grid are not perfectly symmetrical with respect to the model, generating possible inhomogeneity between the flow above and below it. This defect is able to force the lift to act in the other direction, proving again the high instability of the critical regime. This effect is significant of what may occurs also in full-scale conditions, when even small perturbations (from obstacles, trees, etc.) can affect the direction of the lift force.

4.4.5.4 Role of the welding

The contribution of the welding to the aerodynamic behaviour of the cylinder is investigated in the second run of tests (Set n°2), where model B has been tested varying the angle of attack from 0° to 360°. The tests have been performed both in smooth and in turbulent flow (both turbulence levels) at fixed wind tunnel motor frequency (25 Hz), keeping the sub-critical Reynolds range in all the tests.

Figure 4.23 shows the results of mean drag (a) and lift (b) coefficients. The symmetry axis of the cross-section, passing through the welding, is highlighted by a red dashed line. Consistently with the results previously presented, the figure highlights a good symmetry and skew-symmetry in C_D and C_L respectively, as well as a decreasing trend of the drag coefficient along with the increase of the Reynolds number.

The figure shows that the welding has the maximum effects around 90° and 270°, where it is orthogonal to the flow: simultaneously, it enlarges the exposed area (increasing the drag) and maximizes the asymmetry of the section with respect to the flow (increasing the modulus of the lift). The welding is capable of increasing the drag at least of the 20%, while the lift can reach +- 0.8, which is an incredibly high value. This suggests that even small imperfections may able to break the symmetry can cause the lift to be comparable to the drag, changing remarkably the direction of the resultant force with respect to the direction of the flow.

The intermediate turbulence level, which falls in the middle of the critical regime according to $f_T Re$, produces the most unstable trend of both coefficients, causing in particular the highest values of the lift. In addition, the application of the grid makes the lift change sign for every angle, extending the results presented in Section 4.4.5.3 for every angle of attack.

4.4.5.5 Role of the ladder

Then, the ladder has been added to model B to evaluate is aerodynamic contribution. Figure 4.24 shows the results of mean drag (a) and lift (b) coefficients. The ladder prevents the cross-section from having any symmetry (see Figure 4.14); therefore, no axes are traced in the diagram.

The presence of the ladder increases the exposed area. Where the ladder is perpendicular to the flow (around 90° and 270°), the drag undergoes the maximum increase, about +60%. When the ladder is

downstream, the original trend is retraced. When it is upstream, it produces a sort of equivalent Reynolds effect, with a 35% drag reduction. Moreover, the ladder has the effect of increasing the maximum values of the lift, which become very similar to the case of the sole cylinder in turbulent flow (Fig. 4.23), even if they occur at different angles of attack. In the neighbourhood of 180°, results almost overlap with the bare cylinder, as the ladder is shaded by the shaft.

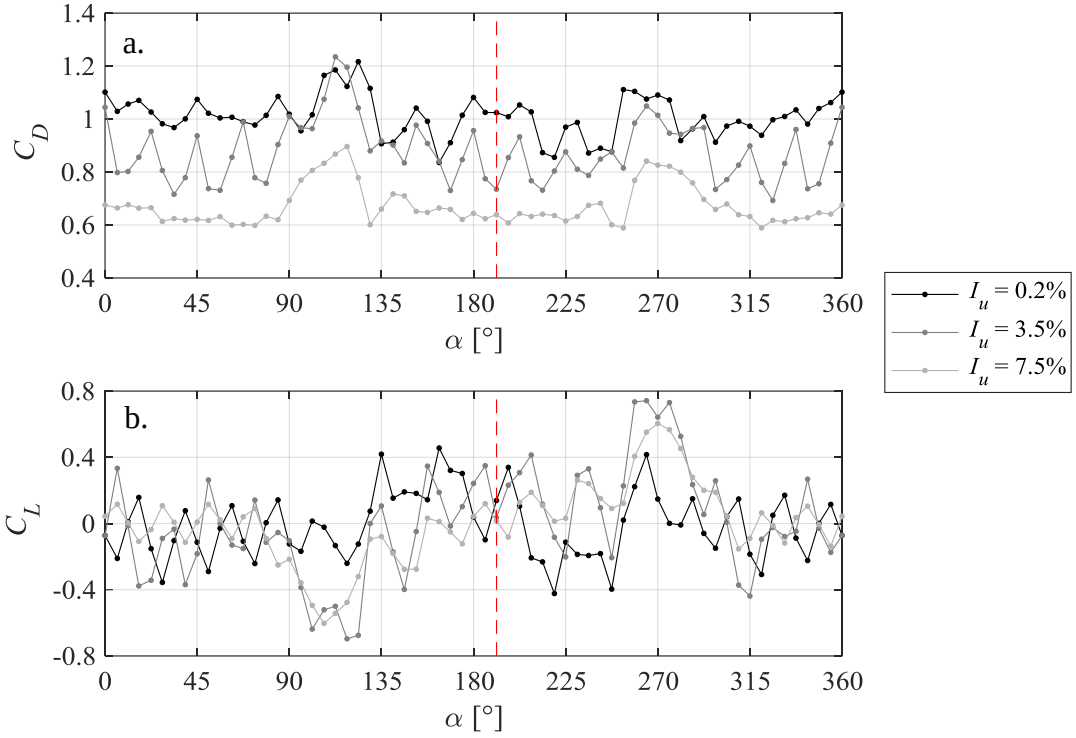

Figure 4.23. Mean drag and lift coefficients as a function of the angle of attack, with fixed motor frequency (25 Hz) and different turbulence intensities. Corner radius *r/D*=0.05.

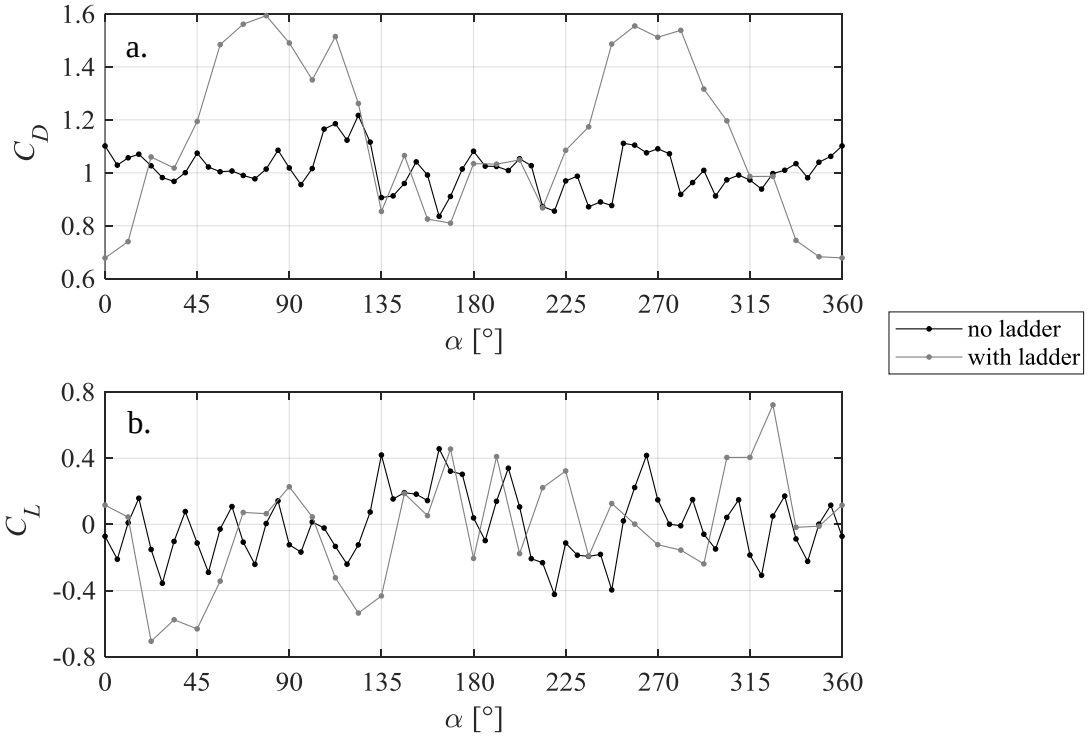

Figure 4.24. Mean drag and lift coefficients as a function of the angle of attack, with smooth flow (I_u<0.2%) and fixed motor frequency (25 Hz), with or without the ladder. Corner radius *r/D*=0.05.

These outcomes suggest some important aspects to take into account in the design of these kind of structures to wind actions. For wind directions opposite to the ladder location, the pole can actually be treated a bare cylinder. For the other directions, it is difficult to predict the aerodynamic contribution of the ladder, which is able to modify deeply the drag even without changing the exposed area.

4.4.5.6 Galloping investigation

The possible occurrence of galloping instability is investigated by calculating the galloping coefficient a_G=- $(C_D+C'_L)$, where C'_L is the first derivative of the mean lift coefficient with respect to the angle of attack, expressed in radians. The necessary condition for its occurrence, known as the *Glauert-Den Hartog criterion*, is that $a_G > 0$, i.e., $C_D+C'_L < 0$. Considering the uncertainties inherent in the galloping onset conditions (Pagnini et al., 2017) this section intends to investigate the conditions ruling the sensitivity of this kind of polygonal shapes to possible galloping critical conditions (Caracoglia and Jones, 2006), leaving out the critical velocity assessment that is beyond the goal of this work. However, it is important to state that, the higher the galloping coefficient is, the lower the critical velocity is.

Figure 4.25 shows the quantity $C_D+C'_L$ of the bare cylinder (Model B) as a function of α. Figure 4.25a shows results in the sector α=0-22.5°, with step not larger than 2°; Figure 4.25 b investigates the whole domain between 0° and 360° with a step of 5.625°. The tests are carried out at 25 Hz of the motor frequency and at with different turbulence levels. The derivative of the lift is computed through the *symmetric difference quotient*:

$$C'_L(\alpha_i) = \frac{C_L(\alpha_{i+1}) - C_L(\alpha_{i-1})}{\alpha_{i+1} - \alpha_{i-1}} \tag{4.5}$$

Despite the simplified method used to compute the lift derivative, if we consider the small variations of the drag and the Lagrange's *mean value theorem*, the values computed are essentially correct at least for one point inside the 11.25° wide neighbourhood, as it is proved for the first sector, where densely sampled data are available. Therefore, the procedure adopted is certainly reliable when the aim is simply to highlight a limited sector where the fulfilment of the necessary condition occurs.

Coherently with previous results, the intermediate turbulence is the one that supplies the maximum a_G value, which in this case is the minimum value of $C_D+C'_L$. . At the highest turbulence level a_G is close to zero for every angle. It is worth noting that there is a general discrepancy of sign between the values obtained in smooth and turbulent flow, i.e., for every α it exists a flow condition in which the instability is met. It means that, for this particular polygonal section, no mean flow directions can be excluded from the possibility of galloping occurrence. Considering the whole domain (Figure 4.25b), it is shown that the condition a_G<0 is satisfied frequently; the most critical sector actually seems to be 0-22.5° that falls outside the influence of the welding.

It must be said that Figure 4.25 only regards model B, where *r/D* is equal to 0.05, disregarding the presence of the ladder. The comparison between the galloping coefficients of model A and B in smooth flow (Figure 4.26) highlights a general flattening along with the increase of *r/D*, as the aerodynamic behaviour of the polygon tends to that of a circular cylinder (as discussed in section 4.4.5.2, Figure 8). With reference to the considered case study, the results show that possible critical issues can affect the lower portion of the shaft, while basically they can be excluded as far as the top portion is concerned. The influence of the ladder on galloping is analysed in Figure 4.27 where the results of model B in smooth flow are compared. The presence of the ladder makes the galloping

coefficient positive for all directions except in a very small domain, where the ladder is upstream and produces a decrease of the drag (Figure 4.24).

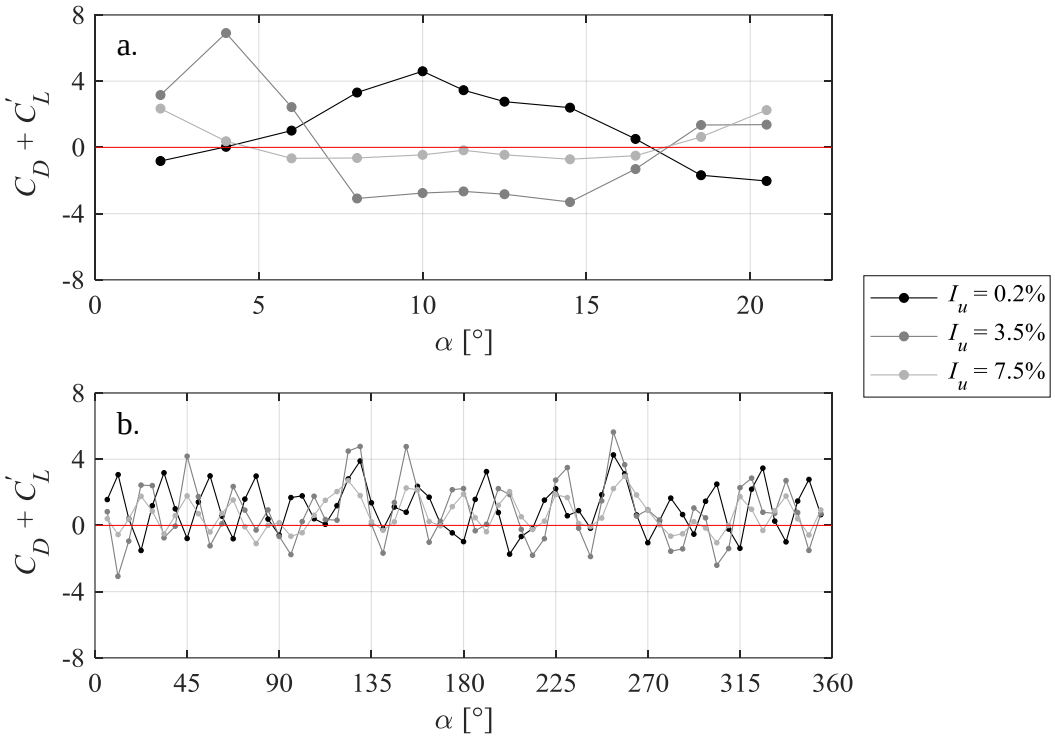

Figure 4.25. Galloping coefficient as a function of the angle of attack, with fixed motor frequency (25 Hz) and different turbulence intensities. Corner radius *r/D*=0.05.

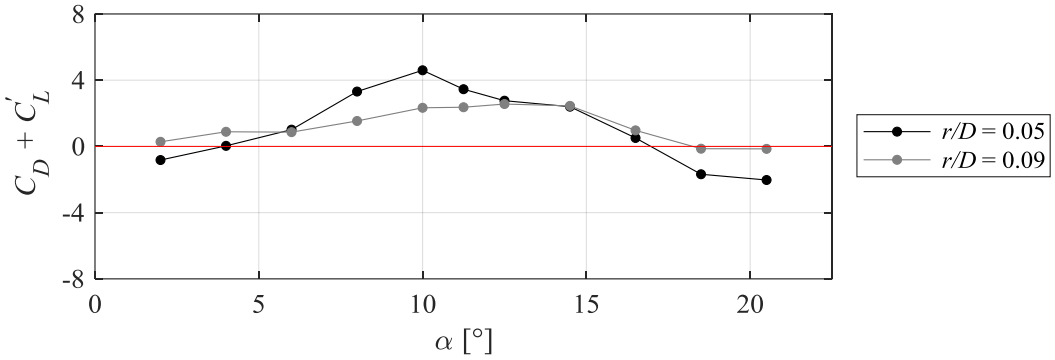

Figure 4.26. Galloping coefficient as a function of the angle of attack, with fixed motor frequency (25 Hz) and turbulence intensity (0.2%), varying corner radius.

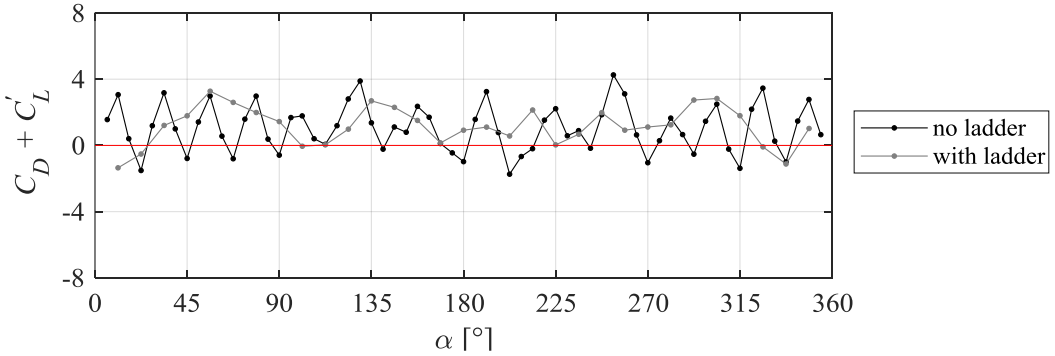

Figure 4.27. Galloping coefficient as a function of the angle of attack, with fixed motor frequency (25 Hz) and turbulence intensity (0.2%), with and without the ladder.

4.4.5.7 Strouhal number

The Strouhal number *St* links the vortex shedding frequency f_{sh} with the mean flow velocity $\bar{U}$, according to the equation $St = f_{sh}\, D/\bar{U}$. For each test, f_{sh} is evaluated from the location of the vortex shedding peak in the power spectral density (PSD) of the lift time-history. Figure 4.28a shows the PSD of the lift force measured on model B in smooth flow with $\bar{U}$=13.6 m/s, while 4.28b regards the tests on model B in turbulent flow (I_u=7.5%) with $\bar{U}$=19.3 m/s. The shedding peak (indicated by the black line) can be distinguished from the rest of the harmonic content since it changes location with flow velocity. When it falls between two structural peaks, as in the figure, it can be identified easily. When the vortex-shedding is resonant with the vibration modes of the model and of the static setup frames, the exact location becomes awkward to determine. Therefore, only the tests that enabled a reliable quantification of *St* have been considered.

Figure 4.28 shows a first important result. Turbulence, which is applied in 4.28b, is able to suppress the vortex shedding excitation, whose energy content is about 20 times lower than in smooth flow (4.28a).

The Strouhal number of the hexadecagonal cross-section has been studied as a function of Reynolds number for the three main orientations of the model. Investigations carried out by ESDU are used as for comparison.

ESDU 96030 (1998) provides a method to derive the response of structures to vortex shedding, applicable to cylinders with circular or polygonal cross-section (side number>8). Consistently with ESDU 79026, polygons are considered as circles characterized by an equivalent roughness based on edge number and corner radius. The document provides one diagram of *St* as a function of the effective Reynolds number, valid for every circular or polygonal section; the asymptotic decrease at high *Re* depends on the effective roughness ε/D of the section, real (for circles) or calculated in equivalent terms (for polygons). However, it is timely to stress that the values of ε/D considered in ESDU 96030 practically belongs only to circular sections, since the ones obtained for our models are in the order of 10^{-2}, which is one order of magnitude greater than the highest proposed. Therefore, there is no reliable information about the trend of *St* of polygonal sections in the high Reynolds range. Finally, it is important to remember that, as in the case of the drag coefficient, ESDU theoretically refers only to polygons corner-oriented.

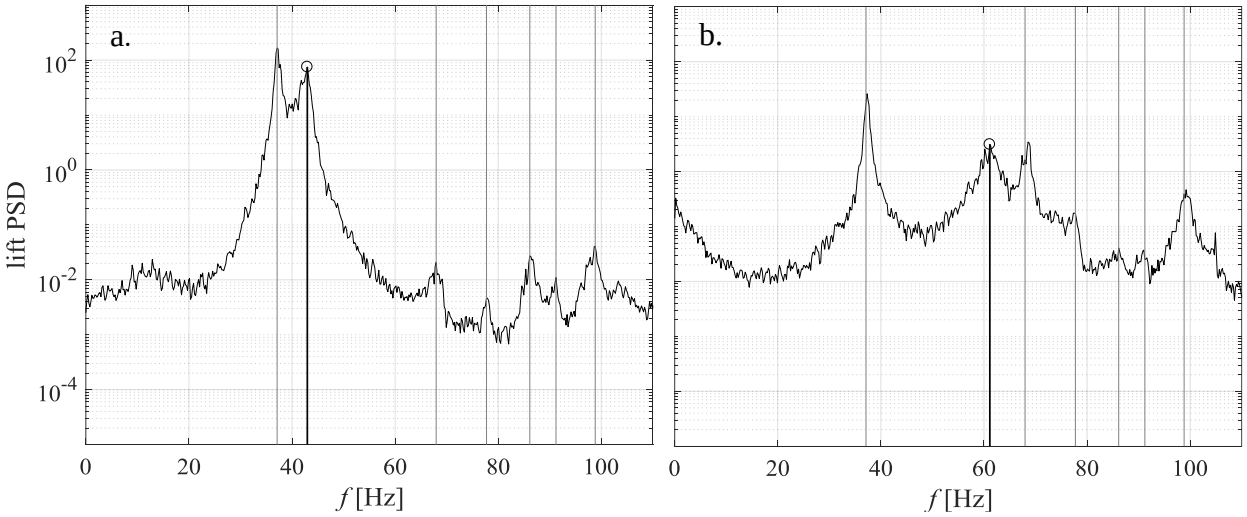

Figure 4.28. Identification of vortex shedding frequency. Black vertical line indicates f_{sh}, while grey lines identify the structural frequencies. a) $\bar{U}$=13.6 m/s. b) $\bar{U}$=19.3 m/s.

Figure 4.29 shows the Strouhal number evaluated from the tests on both model A and B, both in smooth flow and with the two turbulence level, as well as for every considered flow velocity. The three main configurations are investigated: face-orientation (α=0°, Fig. 4.29a), intermediate orientation (α=6°, Fig. 4.29b) and corner-orientation (α=11.25°, Fig. 4.29c).

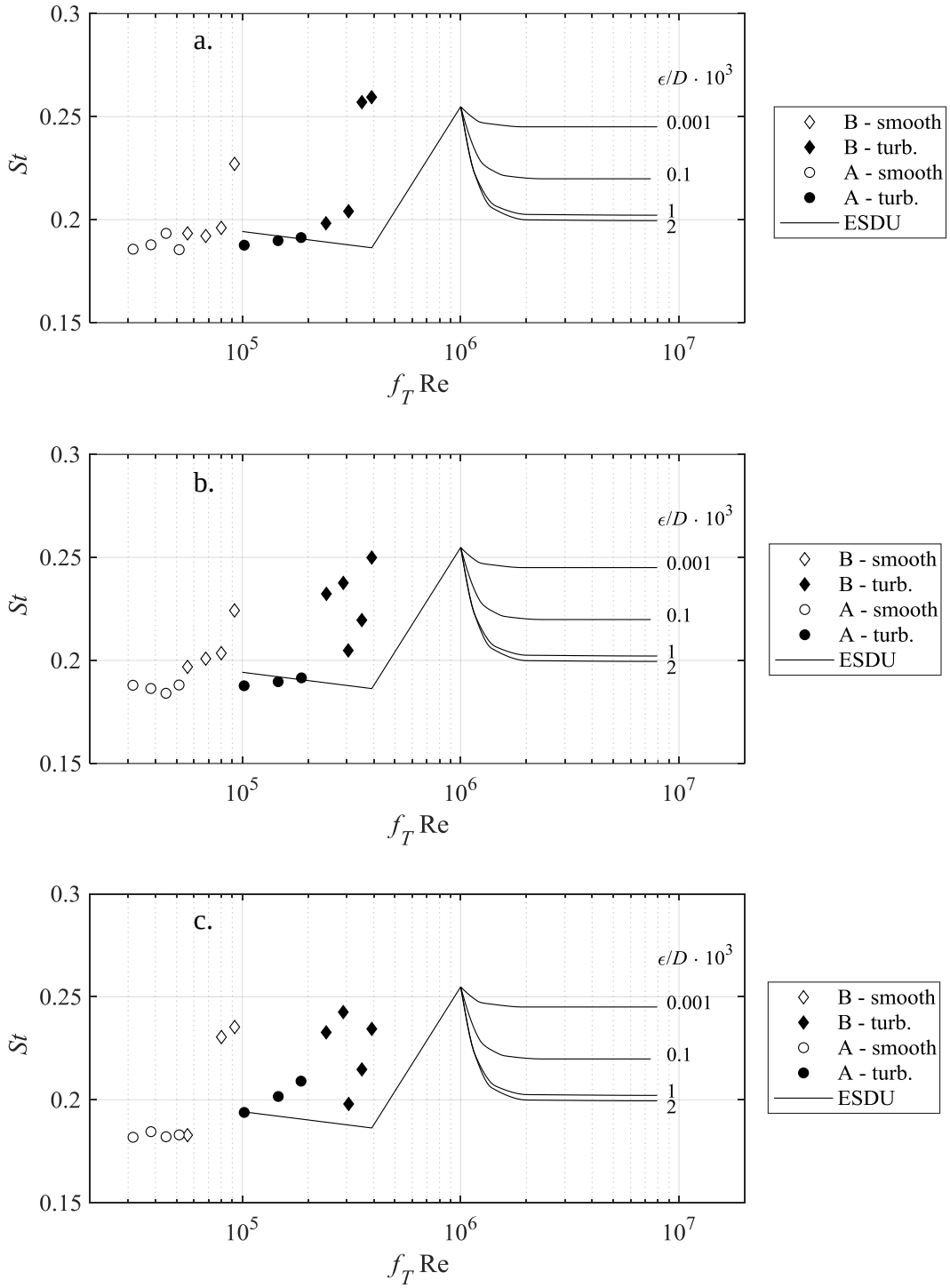

Figure 4.29. Strouhal number as a function of effective Reynolds number for fixed angles of attack. a) α=0° (face-orientation), b), α=6° (mid-orientation), c) α=11.25° (corner-orientation).

The results shown are comparable with the ones regarding the mean force coefficients from a qualitative viewpoint. In particular, smooth and turbulent values follow a similar but independent trend, as if they were indicating the same behaviour but at two separate Reynolds ranges. In addition, with regard to the face-orientation, the turbulent values seems to recall well the trend proposed by ESDU, but at a lower $f_T Re$.

If we move to the corner-orientation, three main differences are noted. First, the subcritical smooth values stabilize at a lower *St* with respect to the face configuration. Second, the sudden growth, both for turbulent and smooth values, seems to occur earlier than the first orientation, at lower effective Reynolds numbers. Last, the *St* values obtained in turbulent conditions scatter across the critical Reynolds range, bifurcating into two different branches that represent two independent growths or, less likely, an increase and an abrupt reduction as shown by ESDU.

Analysing the diagram referred to the mid orientation (α=6°), intermediate results are obtained in every respect, both with regard to the subcritical *St* and with respect to the scattering of the critical values, suggesting a monotonic evolution of the aerodynamic behaviour changing the mean flow direction. It is timely to observe that, unfortunately, the Reynolds range covered in the present campaign is too low to characterize the asymptotic decrease of *St*, where differences between circular and polygonal sections should arise.

4.5 Dynamic Identification

4.5.1 Numerical model

A preliminary numerical estimation of the dynamic behavior of the light tower has been obtained through a simple finite element model (FEM). The model (Fig. 4.30) reproduce the tapered polygonal shaft, the ladder and the two platforms by using solid tetrahedral elements. The lighting equipment has been taken into account with a lumped mass placed in the top platform. The model has been clamped at the lower end of the shaft to simulate the base joint where the pole is embedded in the concrete foundation.

Table 4.2 reports the first modal shapes and frequencies deduced from FEM, clustering the natural modes into groups with homogeneous behavior. Mode No.1 and No.2 reproduce the principal bending mode of a cantilever beam along the two principal inertia axes of the structure. This difference between the two directions is due to the presence of the ladder and the mid platform that produce a non-symmetric behavior. The following modes (grouped into 2nd modes) concern the typical second bending modes of a cantilever beam. From 6 to 9 Hz (grouped into 3rd modes) there are several torsional modes of the top platform and the ladder involving also small torsional motions of the shaft. The other modes occur all beyond 10 Hz.

It should be noted that the FEM model is constructed by deducing data from a preliminary draft of the light pole, not having the full constructive details of the specific tower under investigation. This fact adds some uncertainties to the numerical analysis. FEM results are, therefore, to be considered as a simple guide to the experimental results and not as an actual complement to them.

The mode shapes of the two first bending modes have been extracted from the model and used as input in the reference analytical model. First, because the first bending mode of a vertical cantilever beam is subject to very small variations from case to case, and therefore the uncertainties of the FEM have a negligible effect on it. Second, the numerical estimation of the mode shapes has been considered more reliable than the experimental one since the number of accelerometers for each inertia axis of the structure is very limited.

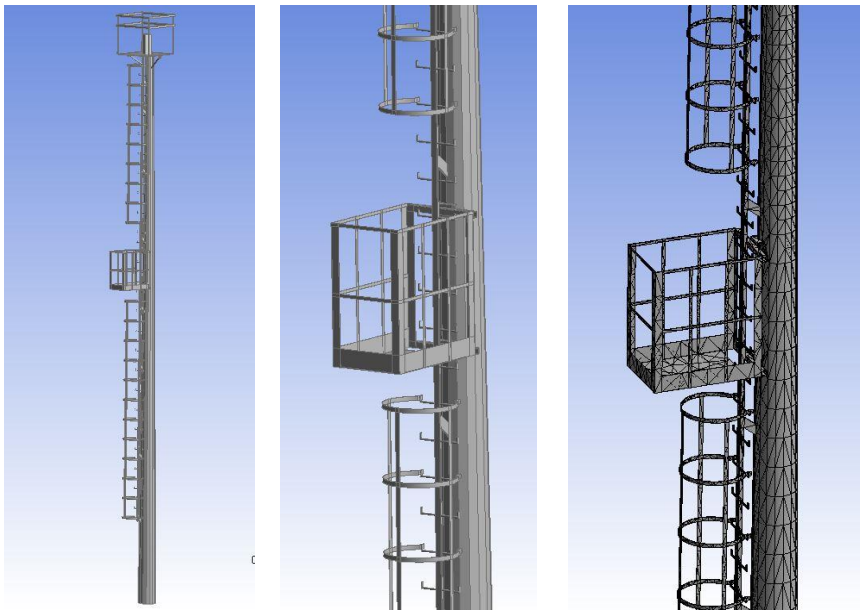

Figure 4.30. Finite element model of the light pole. Geometry (a), ladder and platform detail (b), mesh (c).

Table 4.2. Main vibration modes

Tabular Data

	Mode	Frequency [Hz]	
1	1.	0.77369	1st modes
2	2.	0.90203	
3	3.	4.675	2nd modes
4	4.	5.206	
5	5.	6.0462	3rd modes
6	6.	7.2145	
7	7.	7.7	
8	8.	8.6976	
9	9.	9.1754	
10	10.	12.464	

4.5.2 Dynamic testing

The experimental identification of the dynamic parameters of the structure is pursued through Operational Modal Analysis (OMA) techniques. In OMA, measurement data obtained from the operational responses to ambient vibrations are used to estimate the parameters that describe the dynamic behavior of the system. The fundamental idea of OMA is that the structure to be tested is subjected to some type of excitation that has approximately white noise characteristics, thus it has energy distributed over a wide frequency range that covers the range of the modal properties of the structure.

This assumption implies that the input loads are not driving the system at any particular frequency and therefore any identified frequency associated with significant strong response reflects structural modal response. However, it does not matter much if the actual loads do not have exact white noise characteristics, since what is really important is that all the modes of interest are adequately excited so that their contributions can be captured by the measurements (Brincker and Ventura, 2015).

4.5.3 Natural frequencies

The method used in this work to estimate the modal frequencies is the so-called "peak-picking" technique. The basic idea of the peak-picking technique is that a structure subjected to ambient excitations has strong responses near its natural frequencies. These frequencies can be identified from the peaks in the power spectral densities (PSD) computed for the time histories recorded at the measurement points (Brincker and Ventura, 2015).

Therefore, the PSDs of the acceleration measures have been computed for a reference wind event, in order to identify and discuss the spectral contributions of the light tower. During the reference event, 10-minutes long, wind is blowing from the sea with a mean velocity of 10.7 m/s. Figure 4.31 shows the PSD of accelerations recorded in the ladder direction.

Under the guidance of the FEM outcomes, the modal frequencies below 10 Hz can be associated to the corresponding vibration modes. They are identified as:

- n_1 = 0.76 Hz, first bending mode of the shaft in the ladder plane;
- n_2 = 0.85 Hz, first bending mode of the shaft in the ladder direction;
- n_3 = 3.61 Hz, second bending mode of the tower in the ladder plane;
- n_4 = 3.96 Hz, second bending mode of the tower in the ladder direction;
- n_5 = 4.51:8.31 Hz, dominant torsional modes of platforms and ladder.

From a comparison with the numerical results, there is very good agreement as far as the two first bending frequencies are concerned, with an error minor than 6%. The numerical model starts to overestimate significantly the natural frequencies from the second bending modes, where the error reaches 24%. The discrepancy slightly increases at the higher modes. However, despite the predictable uncertainties of the numerical outcomes, for the moment no updates of the FEM are planned, since only the first bending modes are required for the implementation of the reference analytical model.

In order to define the first bending frequencies as input parameters of the reference model, the peak picking technique has been implemented to run automatically for every wind event of the monitoring database. Indeed, many structural monitoring campaigns found that natural frequencies decrease with wind velocity and, consequently, with oscillation amplitude (Tamura and Suganuma, 1996, Li et al., 2008).

Figure 4.32 shows the evolution of the two first bending frequencies as a function of wind velocity (averaged over 10 minutes), taking into account 1 week of full-scale data. Despite some errors at the lowest wind velocities, where the automatic procedure can fail due to the low excitation of the considered modes, no considerable variation of the natural frequencies is observed. Therefore, the values of n_1 and n_2 identified in the reference event are used as input of the analytical model.

4.5.4 Damping ratios

The evaluation of damping is a much thornier issue especially in low wind conditions, when the damping ratio is expected to be extremely small because of the lack of the aeroelastic contribution. For this reason, estimation techniques based on spectral analysis need a very high frequency resolution (i.e., long time-histories of structural response).

To improve the reliability of the estimates, two different techniques are used comparing their results, taking advantage of procedures specifically aimed at OMA problems. Both techniques fall within the framework of the Frequency-Domain Decomposition (FDD) (Brincker et al., 2000, 2001).

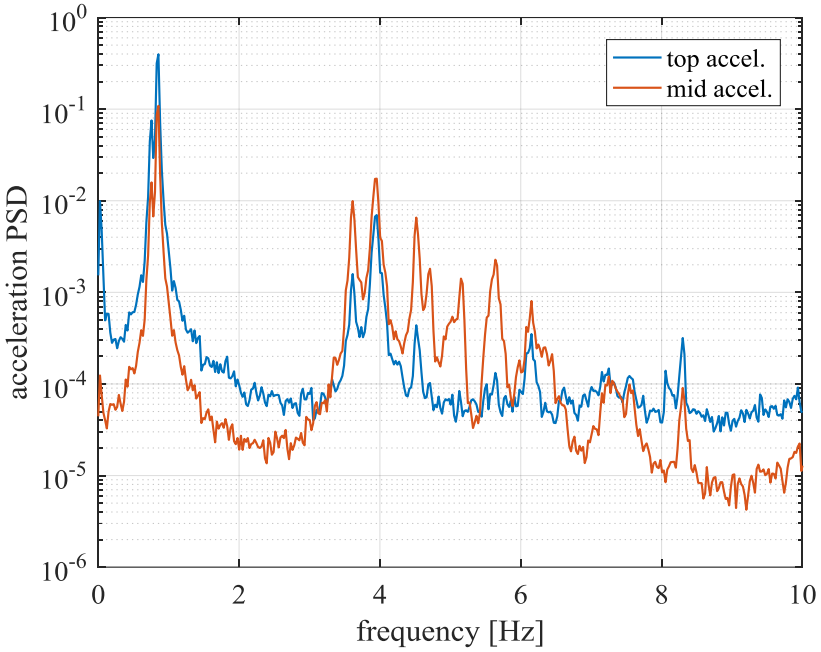

Figure 4.31. PSD of the acceleration recordings during a reference wind event.

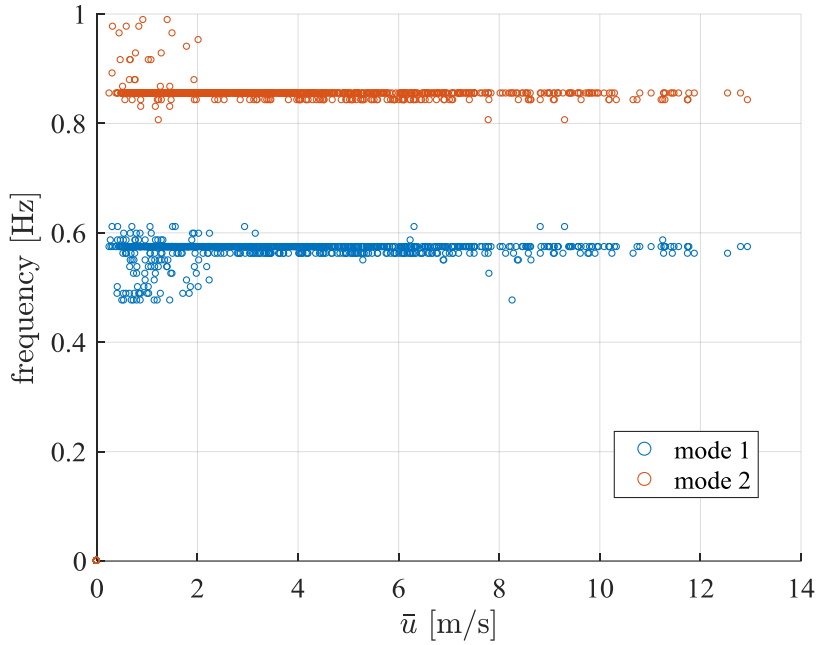

Figure 4.32. First bending frequencies of the tower as a function of wind velocity.

The first one, completely in the frequency domain, has been already used in experimental campaigns carried out by the Wind Engineering research group in Genoa (Carassale and Percivale, 2007, Pagnini et al., 2018). According to these technique, the damping ratios are estimated by line-fitting the first eigenvalue (or singular value) of the spectral density (SD) matrix of the measured accelerations (Figure 4.33). Working in the neighborhood of each resonance frequency, the response can be approximated by the square modulus of the frequency response function of single degree-of-freedom (SDOF) systems. The search for the optimal solution provides an estimate of the frequency and peak value that best approximate (in least-square terms) the experimental response.

Working in both frequency and time domain, the Enhanced Frequency Domain Decomposition (EFDD) technique (Brincker et al., 2001) represents an advancement of the standard FDD. In the classical EFDD, a primary mode shape estimate is defined as the first singular vector at the considered peak. At the spectral lines around the peak, all the singular values were searched, in order to find the singular value at each frequency line where the corresponding singular vector has the highest Modal Assurance Criterion (MAC) value with the primary mode shape estimate, and this singular value is then associated with the single degree-of-freedom system auto spectral density function. The frequency-domain function is reported time domain, where frequency and damping can be estimated by simple means interpreting the correlation function as a free decay of a corresponding SDOF system. This is done in the present study as in the original paper by Brincker et al. (2001), by performing a linear regression on the logarithm of the extremes to estimate the logarithmic decrement of the SDOF oscillator.

Besides applying the EFDD principles, the recommendations for evaluating unbiased correlation functions through Welch's method (Brincker and Ventura, 2015) are followed. In particular, the Welch estimate is obtained by zero-padding non-overlapping data segments. Finally, when turning back to time domain, the unbiased correlation is achieved dividing by a triangular window. The procedure is described in Figure 4.34.

The damping investigation is limited to the identification of the first bending modes in the two principal directions. The study is carried out intersecting the two OMA techniques with the analytical prediction of the calculation model. The measured damping already includes both structural and aerodynamic damping. The model instead quantifies only the aerodynamic part (Eqq. 3.30-3.31); structural damping has been considered as an average value of the measurements at low velocities ($\bar{u}$<2 m/s): $\xi_{s1}\approx 0.1\%$.

In this respect, a consideration should be made. According to the model, aerodynamic damping grows linearly with the drag coefficient and with velocity. In parallel, the WT tests have proved that C_D undergoes an abrupt decrease with velocity (Figure 4.35a). If we depict damping as a function of wind velocity, as it is commonly done to appreciate the aerodynamic contribution, there is a range in which the damping ratio does not grow linearly (Figure 4.35b).

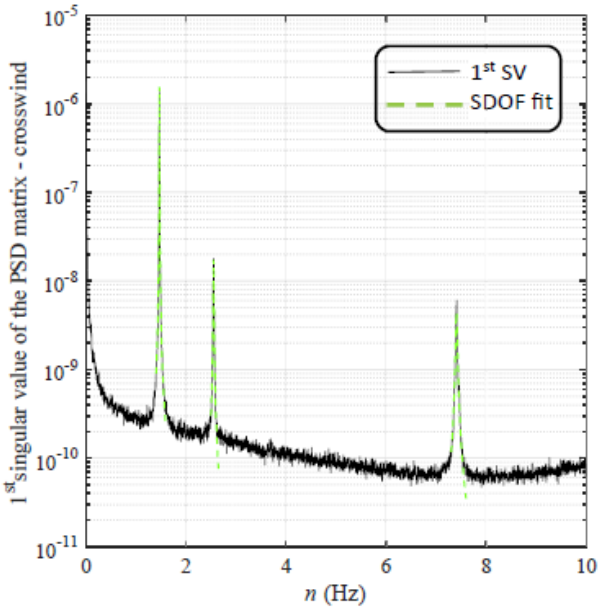

Figure 4.33. Line fitting of the first singular value of the spectral density matrix (from Pagnini et al., 2018).

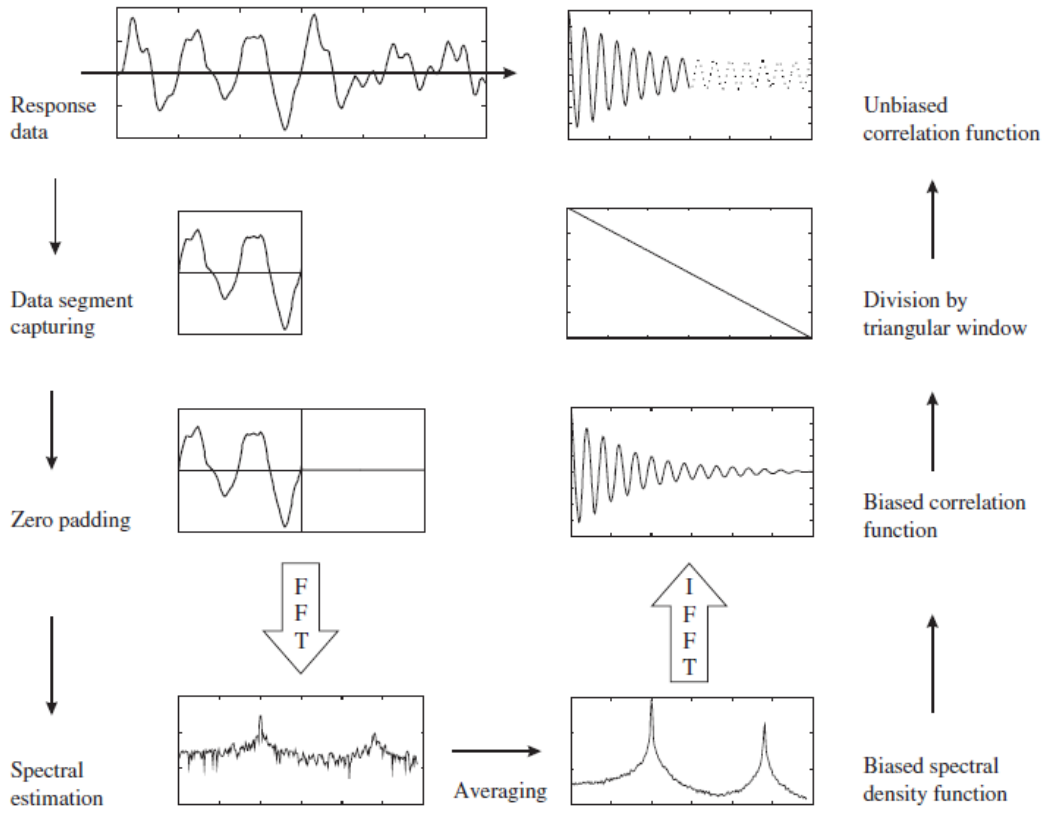

Figure 4.34. Unbiased Welch correlation estimate (from Brincker and Ventura, 2015).

Figure 4.36-4.37 show the results of the comparison between experimental evaluations and analytical predictions. Every empty dot represents 1 hour of registration; the x-coordinate represent the mean wind speed in that 1-hour interval. The abscissa then is divided in velocity intervals 1 m/s-wide (0-1 m/s, 1-2 m/s, etc.) and the damping values falling within each interval have been averaged (filled dots). It is evident that the first modes dissipation is almost evanishing under low wind excitation (i.e., less than 1 per thousand); at a wind speed of 7 m/s, the modal damping has already increased tenfold because of the aerodynamic contribution.

Figure 4.36 considers time histories where wind blows in the direction of the ladder. Therefore, alongwind turbulence excites mode No.2, while crosswind turbulence activates mode No.1. The diagrams show a very good agreement between measurements and predictions, especially in the velocity intervals with lots of data. Moreover, it is interesting to notice that the change of slope is detected by both the OMA techniques; to the best of author's knowledge, no scientific works have ever reported such effect.

Some considerations should be stressed concerning the crosswind damping, whose aerodynamic contribution depends on the inverse of the galloping coefficient ($C_D+C'_L$). Because of the uncertainties highlighted in the wind tunnel tests about the evaluation of the aerodynamic derivatives, C'_L has been set to zero as is the case of circular cylinders. Therefore, from a theoretical viewpoint we should have seen a great dispersion of the measured damping values around the analytical prediction. However, this does not happen in practice, suggesting that the high aerodynamic derivatives computed from WT results, which are referred to the lower portion of the tower, do not affect considerably the global behavior of the structure.

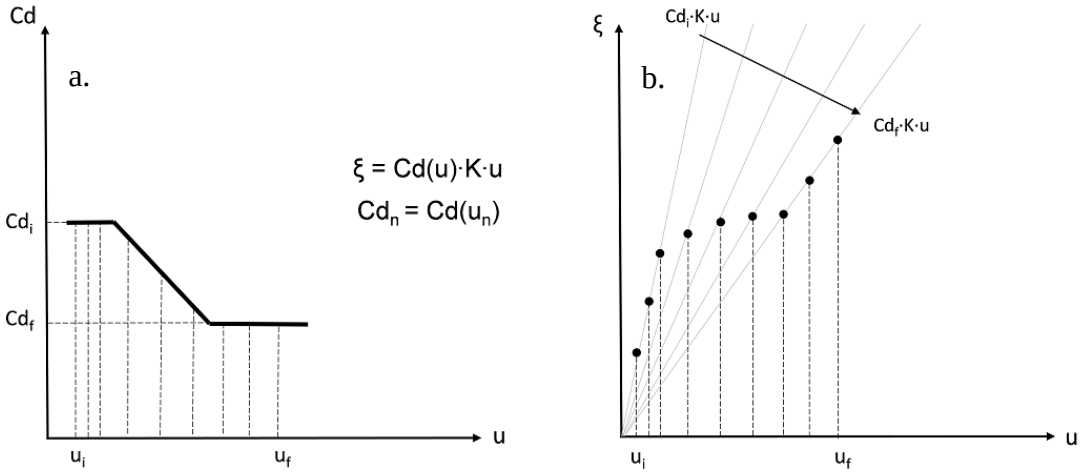

Figure 4.35. Drag crisis effect on aerodynamic damping. Qualitative plot of drag dependence of velocity (a) end resulting damping dependence of velocity (b). K is used to express the proportionality in a simplified way.

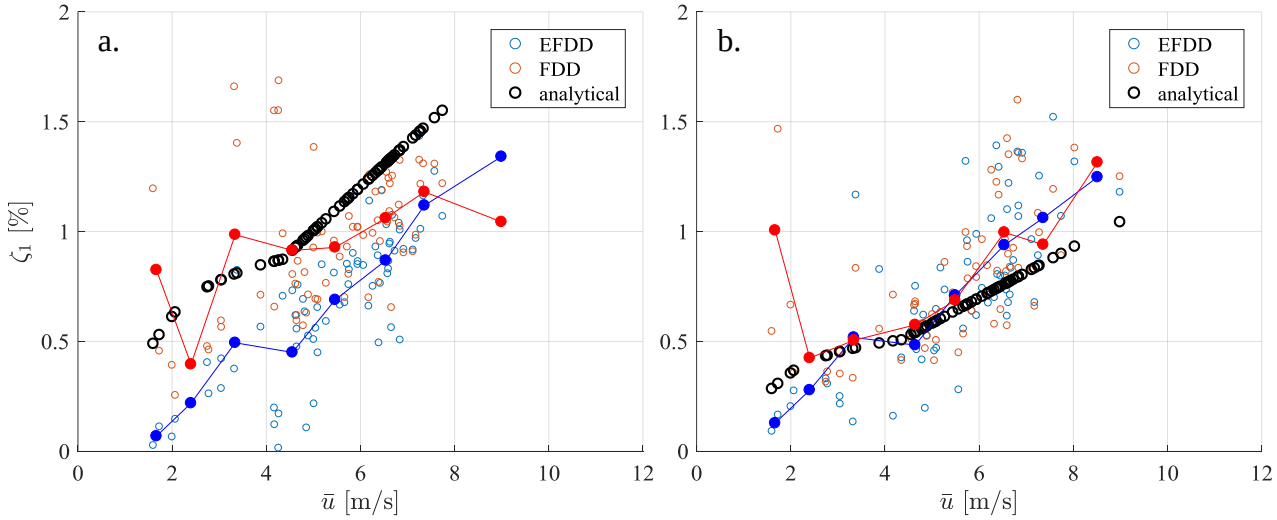

Figure 4.36. Comparisons between experimental estimations and analytical predictions. Wind blows in the ladder direction: mode No.2 excited in the alongwind direction (a), and mode No.1 excited in the crosswind direction (b).

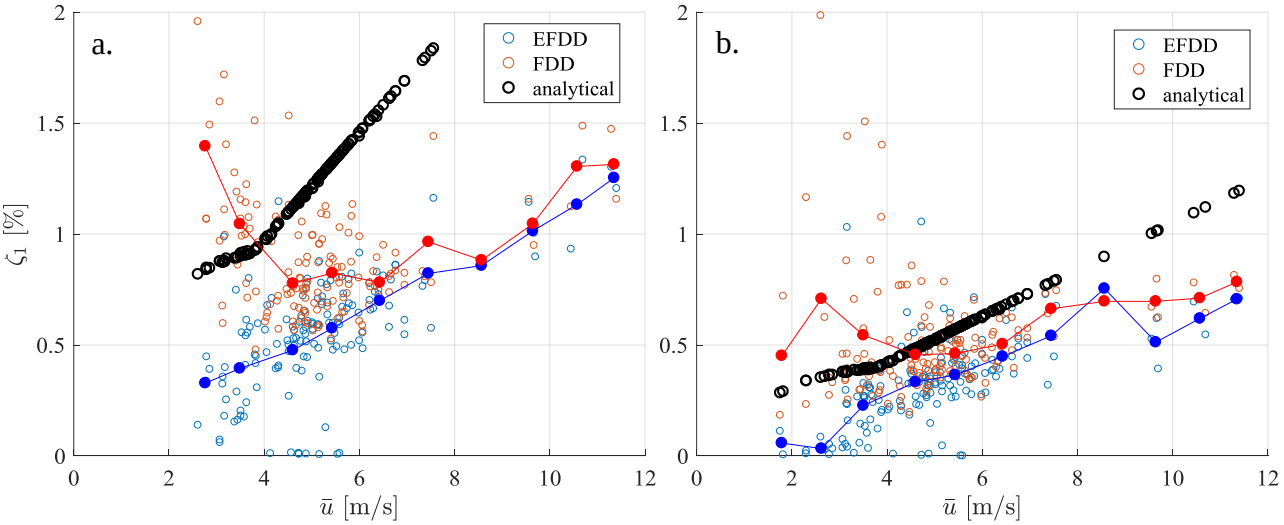

Figure 4.37. Comparisons between experimental estimations and analytical predictions. Wind blows orthogonal to ladder direction: mode No.1 excited in the alongwind direction (a), and mode No.2 excited in the crosswind direction (b).

Figure 4.37 considers time histories where wind blows orthogonally to the ladder. Therefore, alongwind turbulence excites mode No.1, while crosswind turbulence activates mode No.2. In this case, there is a high discrepancy between measurements and predictions. The analytical damping takes into account the augmented drag coefficient due to the presence of the ladder, while the experimental values almost replicate what has been obtained for the other direction. The result points out a symmetric behavior of the structure as far as the aerodynamic contribution to damping is concerned.

4.6 Full scale validation

In this section the calculation model is applied to the monitored structure by assuming, as entry parameters, firstly the values measured during the tests and secondly the ones provided by reference models and standards. The results obtained are affected by three main error sources: (1) the uncertainties of the analytical model; (2) the approximations introduced by estimating the non-measured parameters; (3) the uncertainties related to the experimental measures. When the tests are accurate and properly documented, the error sources (2) and (3) result as quite small and the comparisons become really representative of the model reliability.

4.6.1 Method

Three levels of accuracy of the analytical prediction are considered (Figure 4.38). At the maximum accuracy level (*accuracy level 2*), the response is calculated with the measured values of the parameters, to evaluate the error of the model (model bias). Subsequently, the response is computed by varying the parameters one by one, getting them either from the reference model (*accuracy level 1*), or from current standards and regulations (*accuracy level 0*), in order to quantify the uncertainties due to the parameters (parameter bias).

The comparison is operated in terms of mean and maximum top displacements of the tower over time intervals of length T=10 minutes. The measured displacements are obtained by combining strain and acceleration measurements according to the method defined in Section 2.5.

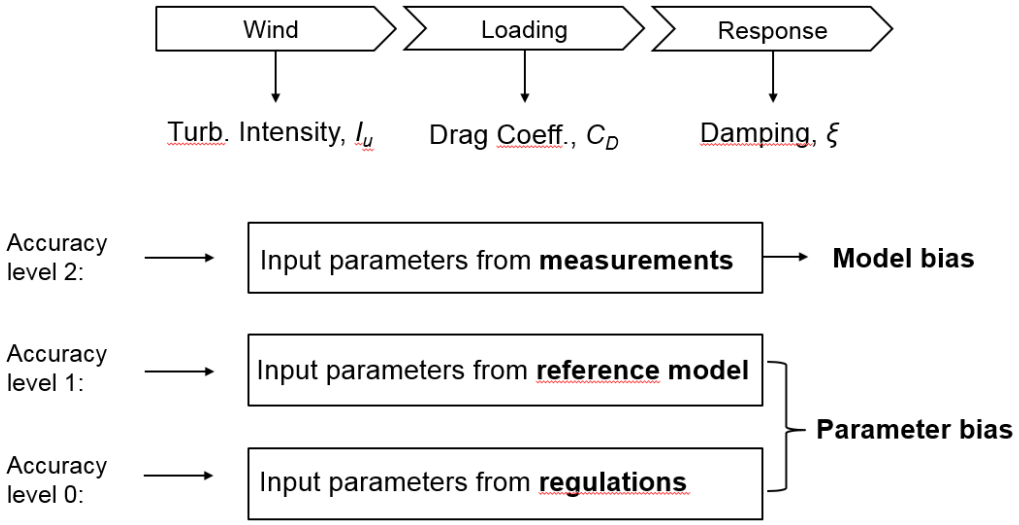

Figure 4.38. Full-scale validation procedure to evaluate model bias and parameter bias.

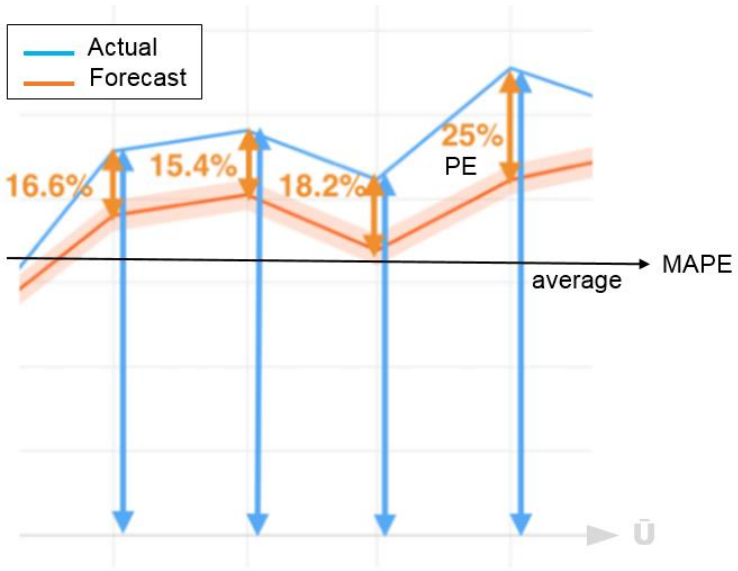

Figure 4.39. Error calculation procedure. Percentage error (PE) is computed for every velocity interval. Finally, all the PEs are averaged to obtain the mean absolute percentage error (MAPE).

Consistently with fundamental hypotheses of the response model (Sections 3.21-3.2.3), available measurements have been subject to a careful selection leaving out the 10-minutes segments not coherent with the following conditions:

- wind speed and direction are stationary over 10-min intervals;
- the structure has a vibration mode along the mean direction of the wind.

The selection is achieved exploiting the statistical matrices characterizing the database. In particular, suitable homogeneous wind events are extracted by imposing:

- 1-hour gust factor $G_{60} < 1.8$;
- standard deviation of wind direction $\sigma_{\alpha 10} < 15°$;
- mean wind direction $\bar{\alpha}$ in the 30°-wide sector around a principal axis of the structure.

The validation is carried out by comparing measured and calculated displacements as a function of mean wind speed. Wind velocities are divided in bins 1-m/s wide; for every bin all the pertinent displacements are averaged (separating measured and analytical ones). Then, for every bin, the percentage error (PE) of the averaged displacement is evaluated as:

$$\mathrm{PE}_i = \frac{A_i - F_i}{A_i} \cdot 100 \tag{4.6}$$

where A_i is the actual value (measured) of the i-th bin and F_i is the forecast (analytical) of the i-th bin. Finally, the absolute values of the percentage errors are averaged to obtain a global parameter representing a measure of the bias of the prediction, defined as the mean absolute percentage error (MAPE):

$$\mathrm{MAPE} = \frac{1}{n}\sum_{i=1}^{n}\left|\frac{A_i - F_i}{A_i}\right| \cdot 100 \tag{4.7}$$

where n is the number of velocity bins considered. Figure 4.39 shows the error calculation procedure.

4.6.2 Model bias

Model bias is quantified by comparing measurements and calculations with *accuracy level 2*. Figures 4.40/4.45 show the results of the comparison. With the same visualization of the previous diagram related to damping (Fig. 4.36), every dot is representative of a 10-minutes interval, and the filled dots are the average of the values falling in the bin. The grey plot represents the percentage error of every velocity bin. For seek of simplicity, the structural axes are herein called *x* and *y*; *x*-axis is in the direction of the ladder, *y*-axis orthogonal.

As far as the alongwind mean displacement is concerned (Figures 4.40-4.41), the figures show an excellent agreement. The dispersion of measurements is very limited except at the low velocities, where noise prevails over wind excitation. Disregards wind velocities lower than 2 m/s, the MAPE is equal to 14.3% and 9.1% for *x* and *y* directions, respectively.

With respect to the maximum alongwind reponse (Figures 4.42-4.43), the analytical model overestimates the displacement at the high velocities, turning out to be slightly conservative. MAPE is 44.9% for *x*-direction and 24.7% for *y*-direction. However, it is timely to note that only few data with high velocities have been collected.

The diagrams of the maximum crosswind displacement (Figures 4.44-4.45) show a greater discrepancy, with MAPE varying from 81.9% to 110%. As a first source of disagreement, C'_L has been put to zero because of the uncertainties highlighted in the wind tunnel tests, as for the investigation of damping. However, measurements should spread around the analytical predictions, while they are always overestimated. In addition, the crosswind response confirms that the vortex shedding phenomenon is negligible for the considered structure, where the critical velocity is ≈ 2m/s.

These diagrams give a measure of the structural uncertainty of the model, having reduced at the minimum the uncertainties due to the input parameters. These results validate the goodness of the model for the considered structural typology. In particular, the validity of the engineering simplifications of the CFS is confirmed (Solari and Pagnini, 1999).

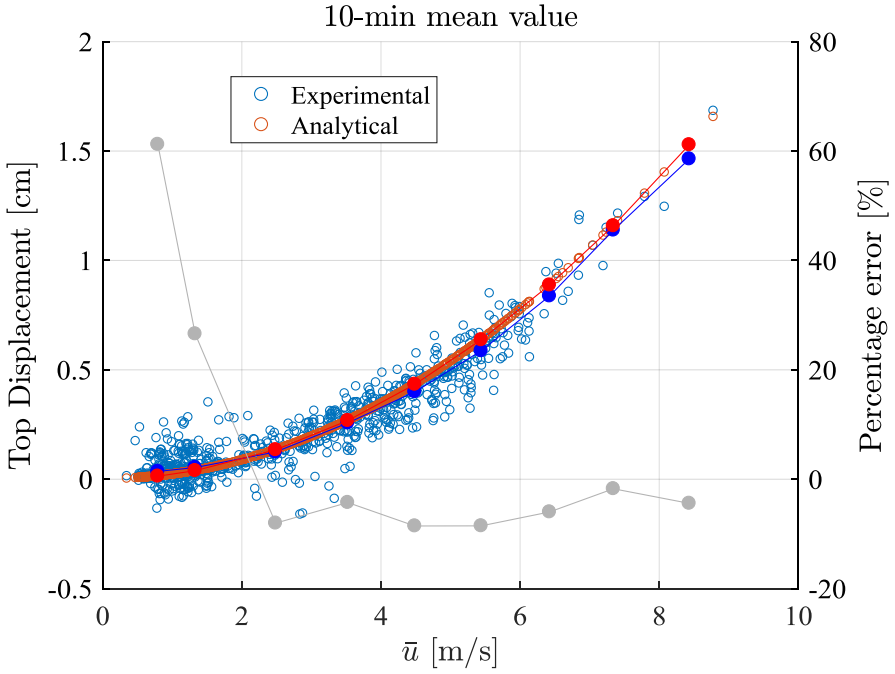

Figure 4.40. Comparison of alongwind mean displacements, wind acting in x-direction. *Accuracy level 2*. MAPE=14.3%.

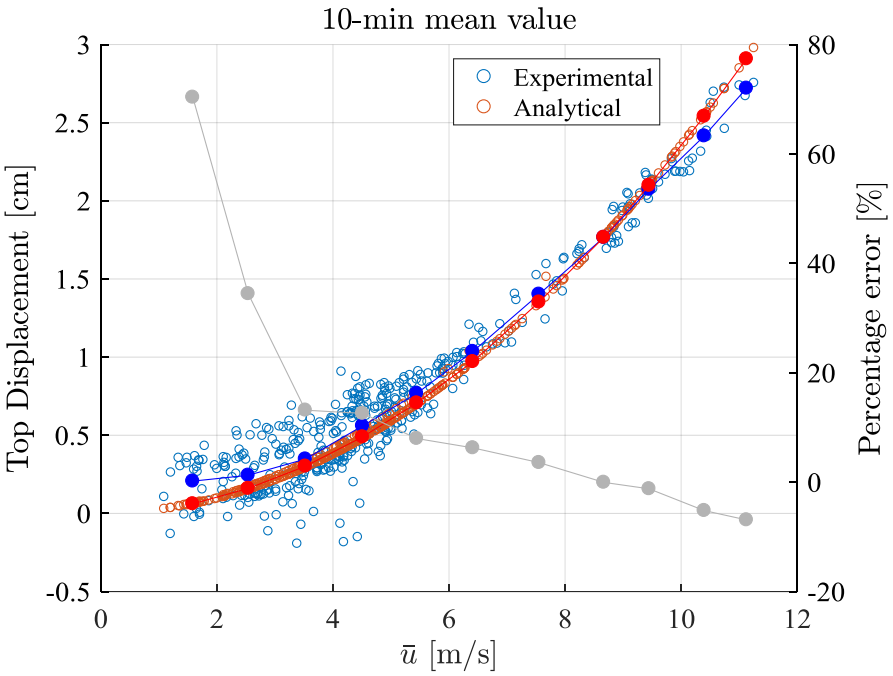

Figure 4.41. Comparison of alongwind mean displacements, wind acting in y-direction. *Accuracy level 2*. MAPE=9.13%.

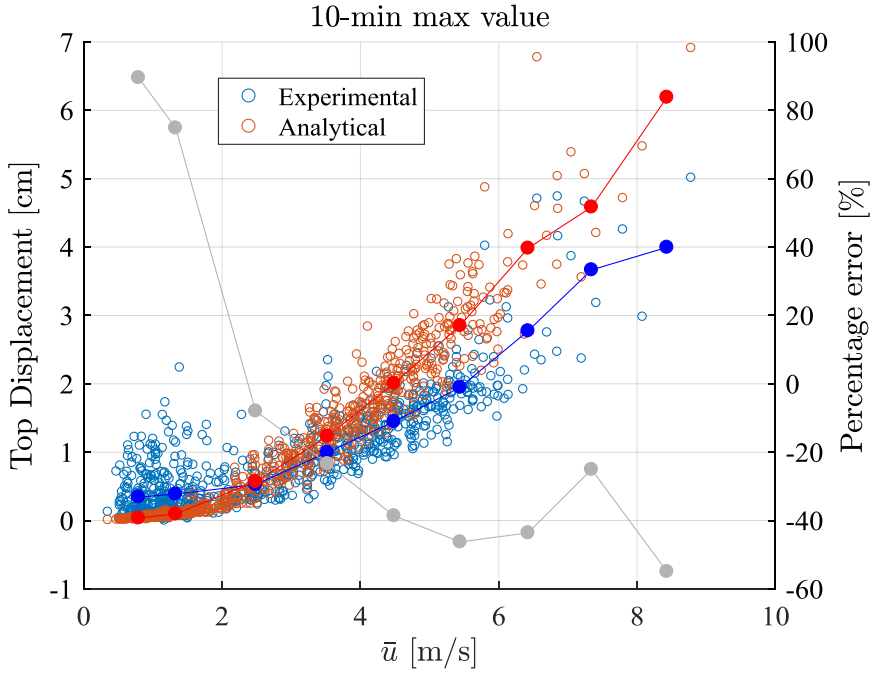

Figure 4.42. Comparison of alongwind maximum displacements, wind acting in x-direction. *Accuracy level 2*. MAPE=44.9%.

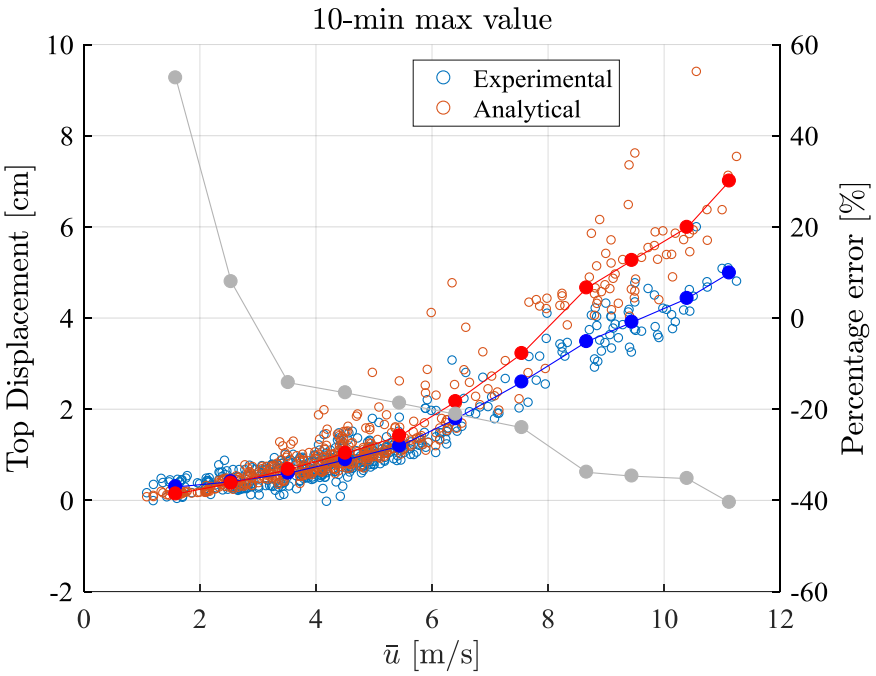

Figure 4.43. Comparison of alongwind maximum displacements, wind acting in y-direction. *Accuracy level 2*. MAPE=24.7%.

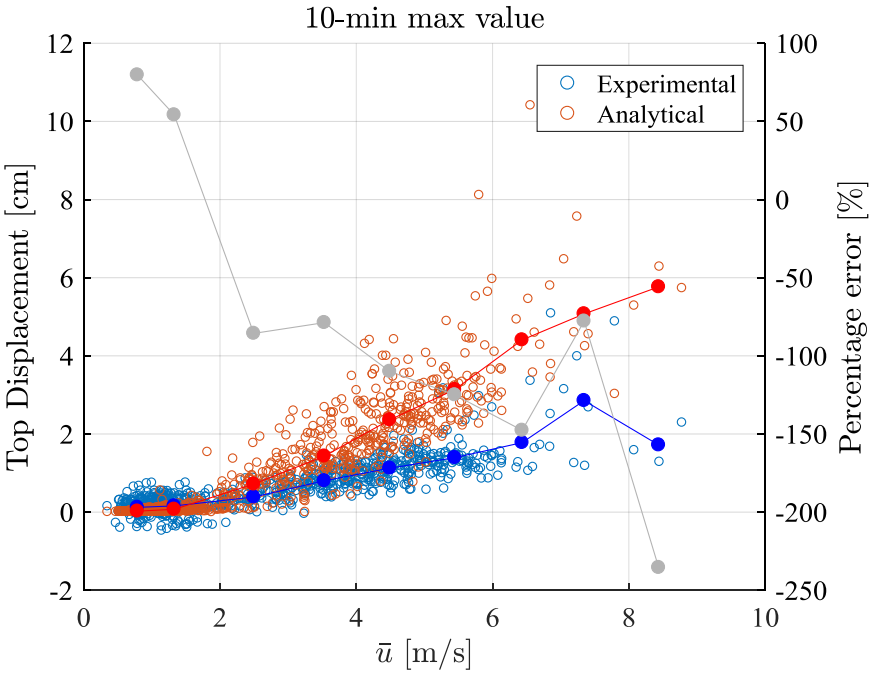

Figure 4.44. Comparison of crosswind maximum displacements, wind acting in x-direction. *Accuracy level 2*. MAPE=110%.

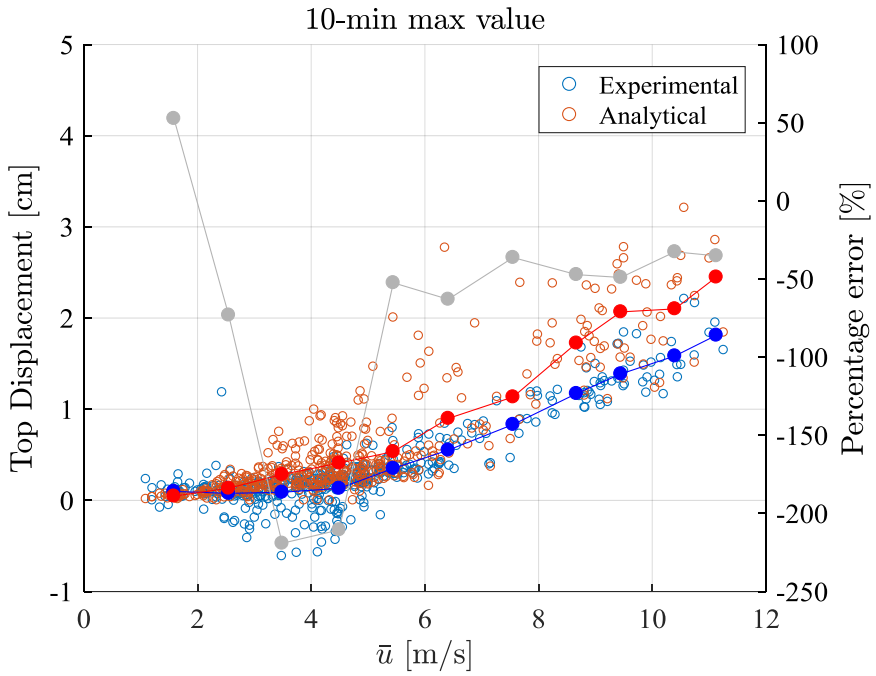

Figure 4.45. Comparison of crosswind maximum displacements, wind acting in y-direction. *Accuracy level 2*. MAPE=81.9%.

4.6.3 Parameter bias

Parameter bias is quantified by comparing measurements with calculations at *accuracy level 1* or *accuracy level 0*. In this case, the error quantification regards only the alongwind response. The parameters that are taken from standards or from the calculation model are turbulence intensity I_u, drag coefficient C_D and damping ratio δ_{x1}. Figures 4.46/4.49 show the results.

Firstly, turbulence intensity I_u is estimated according to the calculation model (Eq. 3.6) where it depends only on z_0. From Figure 4.46 it is observed that the uncertainties associated with turbulence intensities are small: the error increases of just some points with respect to the *level 2* comparison (Figure 4.42), therefore the model gives a reliable measure of the real turbulence.

Then, the weight of the drag coefficient on the wind-induced response is investigated. In particular, the aerodynamic contribution of the ancillaries is highlighted. The drag coefficient of the shaft is taken from Italian standard CNR-DT 207 (2018) where distributed ancillaries are not considered, C_D=1.2. Figure 4.47 shows that when wind blows in the *y*-direction, the mean response is underestimated for every wind velocity by the analytical model, and MAPE almost doubles with respect to the relevant *level 2* comparison (Figure 4.41). This result highlights the importance of considering the presence of ancillaries in the structural design of poles and towers.

Finally, the influence of damping is explored. Recalling Eq. (3.29), structural damping of a is taken from the Italian standard (CNR-DT 207, 2018) where it is equal to 0.2% for the considered structural typology. At first, aerodynamic damping is evaluated according to the model (Eq. 3.30). Figure 4.48 shows the results of the comparison. In this case, the response overestimation highlighted in Figure 4.42 counteracts damping overestimation (Figure 4.36a). Consequently, the error in the maximum response slightly decreases with respect to the reference *level 2* comparison (Figure 4.42).

A further evaluation is carried out using the value of the aerodynamic damping that is supplied by Italian standard (CNR DT-207, 2018) for tubular steel tower. It is given by:

$$\xi_{ax1} = \frac{\rho \bar{u}(\bar{z}) \bar{b} h \bar{C}_D}{4\pi n_{x1} m_{x1}} \tag{5.5}$$

It is immediate to observe that the contribution of the localized masses here is not considered. Damping is therefore strongly underestimated and, as a result, the analytical prediction strongly overestimates the maximum displacement, especially at the high velocities (Figure 4.49); MAPE has tripled with respect to the *level 1* comparison (Figure 4.48).

Such results highlight that a reliable damping evaluation is crucial for the correct evaluation of the structural response. Moreover, disregarding the actual dissipative contribution of localized masses may lead to significant overestimate of the wind-induced actions and effects.

In the overall, it seems that the analytical model always overpredicts the response (on the safe side) except for figures 4.47, i.e. when drag coefficient is largely approximated. This fact confirms the need for wind tunnel analysis.

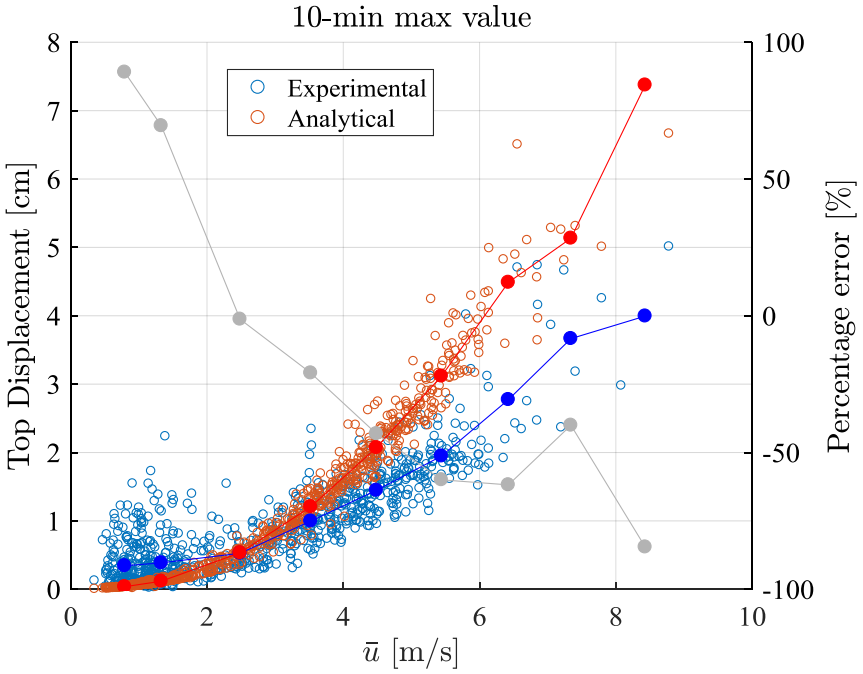

Figure 4.46. Comparison of alongwind maximum displacements, wind acting in x-direction. *Accuracy level 1*: turbulence intensity I_u from reference calculation model. MAPE=52.2%.

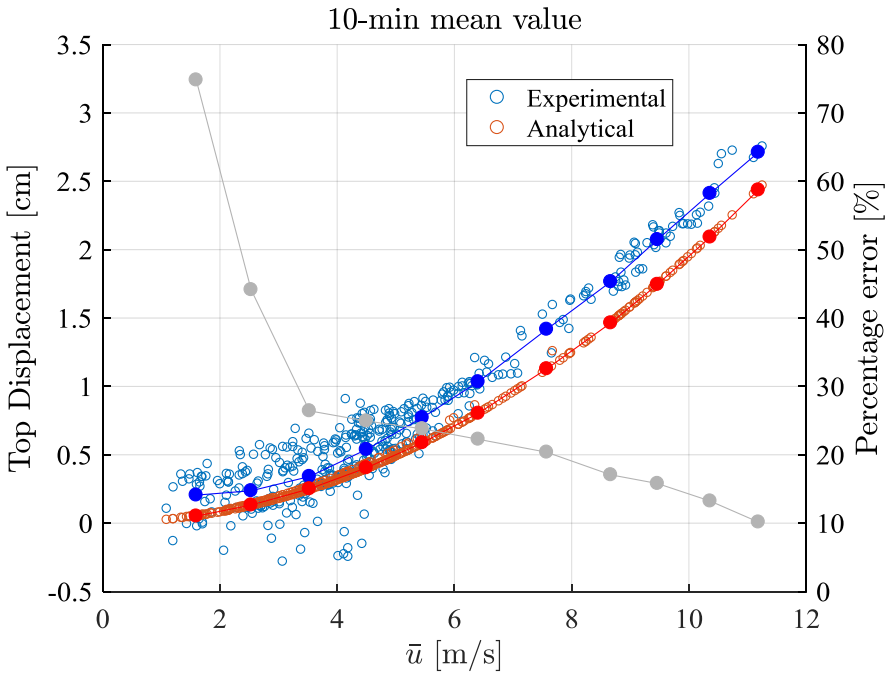

Figure 4.47. Comparison of alongwind mean displacements, wind acting in y-direction. *Accuracy level 0*: drag coefficient C_D from CNR-DT 207. MAPE=26.6%.

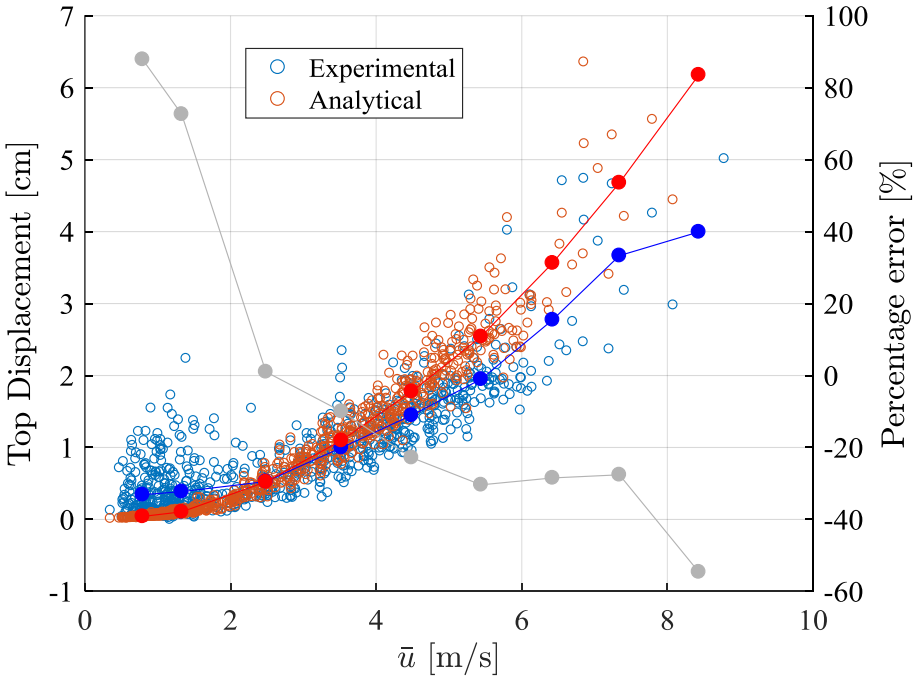

Figure 4.48. Comparison of alongwind maximum displacements, wind acting in x-direction. *Accuracy level 1*: aerodynamic damping from the reference model. MAPE=37.2%.

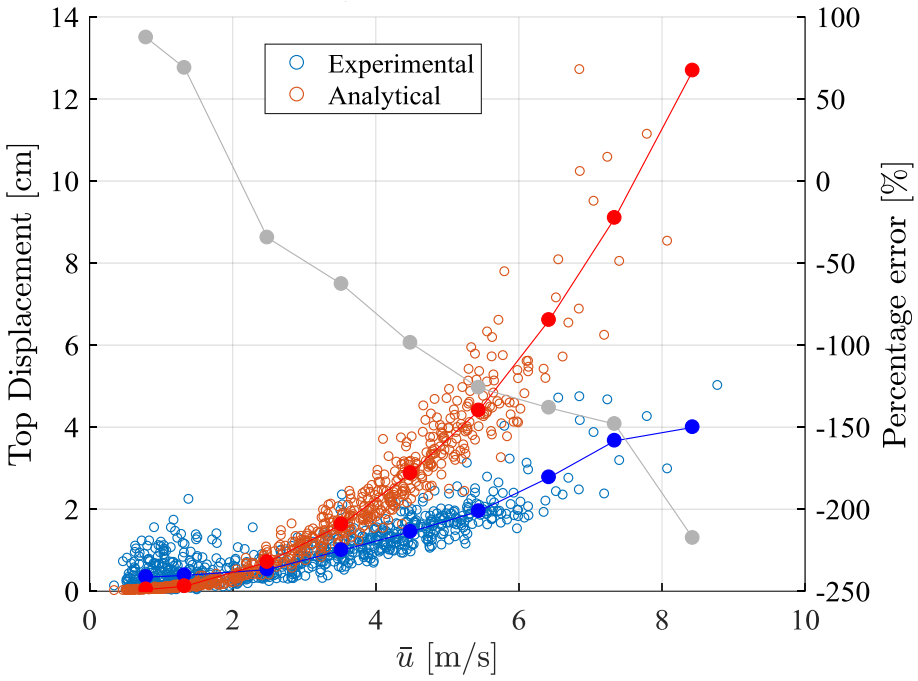

Figure 4.49. Comparison of alongwind maximum displacements, wind acting in x-direction. *Accuracy level 0*: aerodynamic damping from CNR-DT 207. MAPE=109%.

References

AASHTO (1985). Standard Specifications for Structural Supports for Highway Signs, Luminaires and Traffic Signals.

ASCE/SEI 7-02 (2002). Minimum design loads for buildings and other structures.

Bosch, H.R. Guterres, R.M. (2001). Wind tunnel experimental investigation on tapered cylinders for highway support structures. J. Wind Engng Ind. Aerodyn. 89, 1311–1323.

Breuer, M., Bernsdorf, J., Zeiser, T., Durst, F. (2000). Accurate computations of the laminar flow past a square cylinder based on two different methods: lattice-Boltzmann and finite-volume. Intl J. Heat Fluid Flow 21, 186–196.

Brincker, R., Zhang, L., Andersen, P. (2000). Modal identification from ambient responses using frequency domain decomposition. Proc. Int. Modal Analysis Conf. IMAC 18, 625–630, San Antonio, TX, USA.

Brincker, R., Zhang, L., Andersen, P. (2001). Modal identification of output-only systems using frequency domain decomposition. Smart Mater. Struct. 10, 441–445.

Brincker R., Ventura C. E. (2015). Introduction to operational modal analysis. John Wiley & Sons, Ltd.

Buresti, G. Giachi, M., Lombardi, G. (1987). Experimental investigation on the flow-induced load and wake characteristics of finite length triangular prisms. Proc. 7th Int. Conf. on Wind Engineering, Aachen, Germany.

CNR (2018). Guide for the assessment of wind actions and effects on structures - CNR-DT 207 R1/2018. Roma: National Research Council of Italy.

Coutanceau, M., Daefaye, J. R. (1991) Circular cylinder wake configurations: a flow visualization survey. Appl. Mech. Rev. 44 (6), 255–305.

Caracoglia, L., Jones, N.P. (2006). Wind-induced failures of highway light poles during winter storms, ASME Pressure Vessels and Piping Division (Publication) PVP 9, 197-206.

Carassale, L., Percivale, F. (2007) Frequency-domain output-only identification of linear structures subject to stationary excitation. Proc. 5th Int. Conf. On Computational Stochastic Mechanics, Rhodes, Greece, Millpress, Rotterdam.

EN 1991-1-4, 2005. Eurocode 1: Actions on Structures – Part 1.4: General Actions – Wind Actions. CEN, European Commitee for Standardization, Brussels, Belgium.

ESDU 79026 (1980). Mean fluid forces and moments on cylindrical structures: polygonal sections with rounded corners including elliptical shape. London, UK.

ESDU 84011 (2012). Wind speed profiles over terrain with roughness changes. London, UK.

ESDU 96030 (1998). Response of structures to vortex shedding. Structures of circular or polygonal cross section. London, UK.

Igarashi, T. (1997). Drag reduction of a square prism by the flow control using a small rod. J. Wind Engng Indus. Aerodyn. 69–71, 141–153.

James, W.D. Effects of Reynolds number and corner radius on two-dimensional flow around octagonal, dodecagonal and hexdecagonal cylinders, Ph.D.Dissertation, University of Iowa, 1976.

Khaledi, H.A., Andersson, H.I. (2011). On vortex shedding from a hexagonal cylinder. Phys. Lett. A 375, 4007–4021.

Li, Q.S., Xiao, Y.Q., Wu, J.R., Fu, J.Y, Li, Z.N. (2008). Typhoon effects on super tall buildings. J. Sound Vib., 313, 581–602.

Matsumoto, M., (1999). Vortex shedding of bluff bodies: a review. J. Fluids Struct. 13, 791–811.

Mehta, C.K. et al. (1990). Wind drag coefficients for octagonal cylinders, Department of Highways and Public Transportation, Texas Technical University.

Mills, R., Sheridan, J., Hourigan, K. (2003). Particle image velocimetry and visualization of natural and forced flow around rectangular cylinders. J. Fluid Mech. 478, 299–323.

Okajima, A. (1982). Strouhal numbers of rectangular cylinders. J. Fluid Mech. 123, 379–398.

Pagnini, L.C., Piccardo, G., Repetto, M.P. (2018). Full-scale behavior of a small size vertical axis wind turbine. Renew. Energy, 127, 41–55.

Roshko, A. (1955). On the wake and drag of bluff bodies. J. Aero. Sc. 22, 124–132.

Solari, G., Pagnini, L.C. (1999). Gust buffeting and aeroelastic behaviour of poles and monotubolar towers. J. Fluids Struct. 13(7-8), 877-905.

Tamura, Y., Suganuma, S. (1996). Evaluation of amplitude-dependent damping and natural frequency of building during strong winds. J. Wind Eng. Ind. Aerodyn. 59, 115-130.

Tamura, T., Miyagi, T. (1999). The effect of turbulence on aerodynamic forces on a square cylinder with various corner shapes. J. Wind Engng. Ind. Aerodyn. 83, 135-145.

Thompson, M.C., Leweke, T., Williamson, C.H.K. (2001). The physical mechanism of transition in bluff body wake. J. Fluids Struct. 15, 607–616.

Tian, X., Li, S. (2007). Scientific measurements of disturbance on the prototype stands in a low speed wind tunnel. Exp. Res. Aerodyn. 25(3), 1–6.

Tian, Z. W., Wu, Z.N. (2009). A study of two-dimensional flow past regular polygons via conformal mapping. J. Fluid Mech. 628, 121–154.

Van Hinsberg, N.P., Schewe, G., Jacobs, M. (2017). Experiments on the aerodynamic behaviour of square cylinders with rounded corners at Reynolds numbers up to 12 million. J. Fluids Struct. 74, 214-233.

Van Hinsberg, N.P., Schewe, G., Jacobs, M. (2018). Experimental investigation on the combined effects of surface roughness and corner radius for square cylinders at high Reynolds numbers up to 10^7. J. Wind Engng. Ind. Aerodyn. 173, 14-27.

Williamson, C.H.K. (1988). Defining a universal and continuous Strouhal–Reynolds number relationship for the laminar vortex shedding of a circular cylinder. Phys. Fluids 31 (10), 2742–2744.

Williamson, C.H.K. (1996). Vortex dynamics in the cylinder wake. Annual Review of Fluid Mechanics 28, 477–539.

Xu, S.J., Zhang, W.G., Gan, L., Li, M.G., Zhou, Y. (2017). Experimental study of flow around polygonal cylinders. J. Fluid Mech. 812, 251-278.

Yeung, W.W.H. (2010). On the relationships among Strouhal number, pressure drag, and separation pressure for blocked bluff-body flow. Trans. ASME J. Fluids Engng 132 (2), 021201.

Zdravkovich, M.M. (1997). Flow around Circular Cylinders, Volume 1. Oxford Science Publications.

Zhou, L., Cheng, M., Hung, K.C. (2005). Suppression of fluid force on a square cylinder by flow control. J. Fluids Struct. 21, 151–167.

5. Vertical slender structures with rotating masses

5.1 Introduction

The large interest attracted by the exploitation of wind energy (GWEC, 2016) has led to an extensive scientific literature on large wind turbines based on a well consolidated technology (e.g. Hau. 2103, Hansen, 2015). Turbines having a rated power of 8MW are now operational and the trend marks a steady growth in the size of the installations. At the same time, the increased attention in distributed power generation for smart cities as well as for green buildings has been accompanied by a large interest in micro and small wind turbines (Wood, 2011, Tummala et al., 2016, Liu et al., 2019).

However, this interest has not been accompanied by appropriate technological improvement so that small wind turbines still play a marginal role in the energy production and the low economic return does not pay back the use of very expensive and complicated calculations for their design (Bracco et al., 2018).

Actually, the behavior of small wind turbines is as complex as that of the large ones; vibratory phenomena may compromise the structural safety and reduce the effective lifetime. Since they operate close to the ground surface, small wind turbines are exposed to high turbulent fluctuations of the wind speed (Lubitz, 2014, Evans, 2017). The variable rotational speed may cause resonant conditions with the structural frequencies that can produce severe structural vibrations (Castellani et al., 2019, Wang et al., 2018). All these effects have a detrimental impact on power production (Danao et al., 2013, Battisti et al., 2018, Kosasih & Hudin, 2016) and on fatigue life (Liu et al., 2020, Mouzakis et al., 1999, Riziotis & Voutsinas, 2000, Tabrizi et al., 2017). However, given the limited dimensions of the rotor and the supporting shaft, structural verification are usually carried out with simplified procedures, disregarding the complex dynamic interaction of fixed and rotating parts as well as the turbulent action of the wind. As a result, frequent damages and collapses are observed, both to the blades and to the supporting structure. Figure 5.1 shows some examples of fatigue cracks recently detected in small size wind turbines.

Therefore, there is the need, from the one hand, to improve and further develop the technology for these specific applications, and, from the other, to carry out full-scale analyses in order to lead up to simplified, yet reliable, calculation procedures.

Extensive numerical analyses and wind tunnel experiments exist for the design and the parameter assessment of optimum small wind turbine rotors (see, e.g. Rolland et al., 2013, Bukala et al., 2015, Abdalrahman et al., 2017, Rezaeiha et al., 2017). However, detailed reports on full-scale results are quite scanty and mainly related to horizontal axis technology (Wright and Wood, 2004, Nagai et al., 2009). Few papers deal with dynamic characterization (e.g. Staino and Basu, 2013, Thresher et al., 2009) and definition of simplified calculation procedures of the structural response of small wind turbines (e.g. Gong and Chen, 2015, Verkinderen and Imam, 2015) which are supplied by specific guidelines limitedly to the horizontal axis technology (IEC, 2005).

Experimental studies are almost entirely related to large size wind turbines (e.g., Ozbeck and Rixen, 2013, Hu et al., 2015a, 2015b, Bajrić et al., 2018) while, at the best knowledge of the authors, structural monitoring on small wind turbines are not detailed in peered review papers. Reports on the subject are very few and applied to obsolete prototype. Among these, Carne et al. (1982) described

the modal testing of a rotating Darrieus-type wind turbine, comparing modal frequencies and shapes with values predicted over a wide range of rotational speeds.

Starting from these premises, the present chapter investigates the structural response of a real slender structure with rotating masses. It reports the results of the monitoring campaign launched in 2015 over a small size vertical axis wind turbine installed on the quay of the Savona Harbor (Northern Italy). In this case, both the monitoring chain and the input parameters were already defined. After a brief literature review about the structural design of small wind turbines, the calculation model is again applied to assess its suitability for parked turbines. Then, the effects of rotation on the modal properties are investigated, with the final aim (that remains as a perspective of the present work) of generalizing the calculation model to rotating-masses structures. The last part of the chapter discusses the fatigue assessment of the turbine. In particular, the study addresses issues related to stationary and non-stationary excitations, which are rarely dealt in literature on the basis of full-scale data. Great emphasis is given to the fatigue study, which becomes a dominant design loading for structures subjected to additional cyclic excitation besides the wind (like wind turbines).

a)

b)

Figure 5.1. Fatigue cracks and collapses recently detected in small size wind turbine: fatigue crack of the welding joint at the base of a horizontal axis wind turbine (a); fatigue collapse of bolted blade support of a vertical axis wind turbine (b). Courtesy Italian Institute of Welding.

5.2 Monitoring of a small wind turbine

5.2.1 Description of the case study

The experimental facility of Savona Harbor integrates solar energy-generating units with small size wind turbines for wind power production. In its original configuration it included a rooftop 6 kW vertical axis wind turbine (VAWT) and two 20kW turbines, having vertical and horizontal axis, respectively, installed on the harbor dam, just in front of the sea. The 6 kW VAWT was causing

persistent strong vibrations over the building roof and was dismantled soon after its installation. The two 20 kW turbines (Figures 5.2a, b) experienced severe problems due to atmospheric and environmental phenomena, such as coastal storms, lightings and gusty winds. Wind gusts and atmospheric turbulence caused many downtimes to the horizontal axis wind turbine. Especially, fatigue phenomena induced by mechanical stress caused severe cracks originating from the welding of the bottom stiffener flanges (Figure 5.2c). It has been therefore dismantled after three years of operation.

The VAWT has been refurbished in 2014, improving the control apparatus and the breaking system, and has been operational until a further interruption not attributable to the turbine itself when, in late 2018, an exceptional storm caused severe damage to the concrete dam. It is an H-rotor turbine having 8 m diameter, 5.8 m height and 5 aluminized steel and fiberglass blades. According to the power curve supplied by the manufacturer, the cut in wind speed is 3.5 m/s, the nominal wind speed is 12.5 m/s at the rated rpm equal to 48; the cut-out wind speed is 18 m/s.

It is supported by a 10.8 m high steel pole based on the concrete dam, at 4.5 m above sea level. Therefore the rotor center is approximately 18 m above the ground. The supporting pole is made up of two steel polygonal shafts, respectively 8 and 6mm thick, connected through telescopic slip joints. The base and top diameters are, respectively, 876 mm and 612 mm. The slenderness of the tower is ≈ 15, calculated as the ratio between height and an average diameter. The lower part of the pole is characterized by an inspection opening.

The bottom of the shaft (Figure 5.3 a, b, c) is welded to a 40mm plate; 10 welded plates, each 10 mm thick, stiffen the connection. The 40 mm plate is bolted to the foundation with a non-completed concrete cast that does not constitute a perfect clamped end.

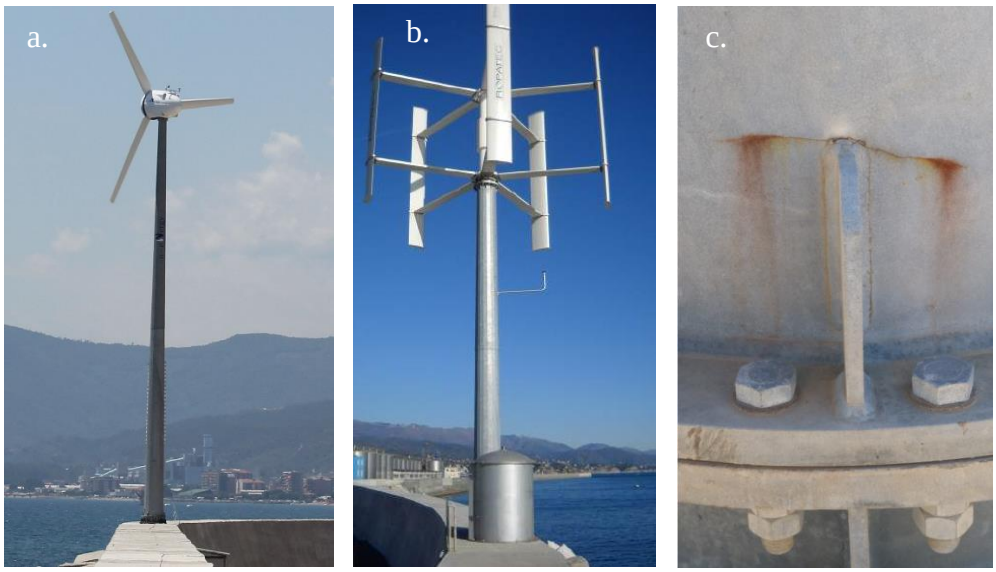

Figure 5.2. Horizontal axis (a) and vertical axis wind turbine (b) on the dam of the Savona Harbour; fatigue cracks at the base of the horizontal axis wind turbine (c).

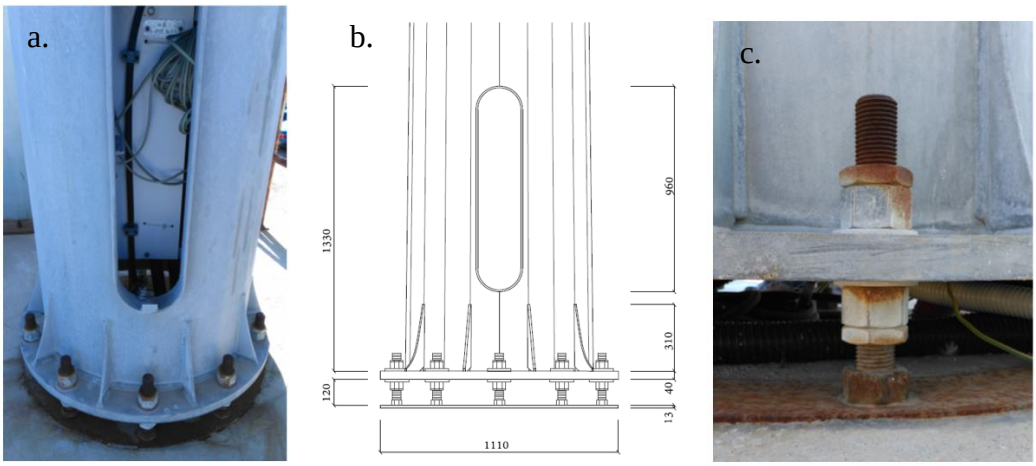

Figure 5.3. Base details with inspection opening (a, b) and bolted connection (c).

5.2.2 Monitoring equipment

The monitoring equipment is composed by anemometric, power and structural monitoring sensors (Pagnini et al., 2015, 2018). Wind speed at the site is recorded by a cup anemometer installed on the supporting pole (therefore partially sheltered) and by a three-axial sonic anemometer belonging to the network of the European Project "Wind and Ports" (Solari et al., 2012). It is installed on a flat roof at 12.5 m above the ground level, about 160 meters far from the turbine. It supplies high-resolution wind velocities, recording the three components of the wind with a frequency rate of 10 Hz.

Structural vibrations of the supporting pole are recorded by two Jewell LCA-100 type tri-axial servo-accelerometers, operating in the range ±2g with 100 μg resolution. They are positioned at the top (10.6 m from the base) and at an intermediate level (8.6 m). Eight mono-axial and one tria-xial strain gauges are placed at the base of the tower to investigate the static and quasi-static response of the structure. The former measure the nominal strain in at the pole bottom, the latter measures local stresses around the inspection door, close to the base, in the part of the tower characterized by critical structural details for fatigue. Positions of the sensors are reported in Figure 5.4, together with the numbering of the acquisition channels.

Sensors are cable connected to a data logger positioned inside a watertight booth at the foot of the turbine. The acquisition frequency of the sensors is set to 200 Hz; the acceleration signals are pre-conditioned by a low-pass analogical Butterworth filter set to 60 Hz. Power production, turbine rotational speed and wind velocity from the cup anemometer are recorded each 10 seconds.

As already mentioned, in this case the monitoring system was built before the beginning of this research project. However, at the end of 2017 the strain gauges have been renewed since the earlier ones were suffering strong thermal effects.

5.2.3 Numerical modelling

During previous studies, a finite element model of the wind turbine was also built. Blades, horizontal arms and the supporting pole have been simulated by equivalent frame elements (Figure 5.5a, b); the compliance of base joint is obtained by suitable spring elements calibrated through a fine 3D local model of the related detail, which instead has been realized within this research project (Figure 5.5c). The local model is built using solid elements, reproducing the tubular pole with front opening, stiffeners and welded base plate with anchor bolts, considered as clamped at the base.

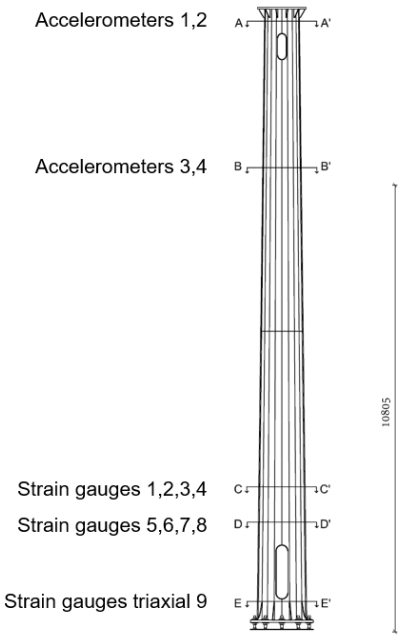

Figure 5.4. VAWT sensor positions.

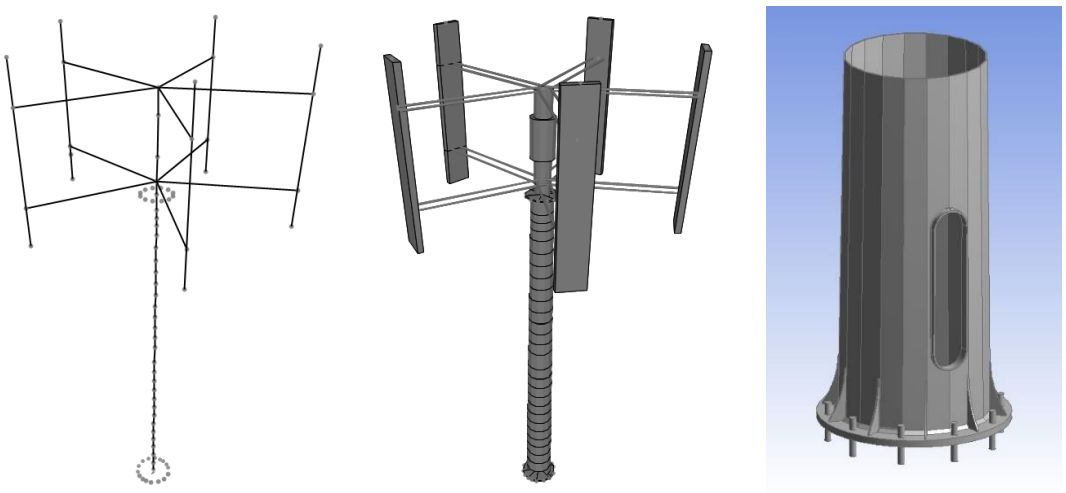

Figure 5.5. Finite element model of the wind turbine (a) and its extruded view (b). Local finite element model of the base joint (c).

5.3 Wind-induced response of the parked turbine

Wind-induced response of the parked turbine is evaluated by applying the calculation model with the same procedure used for the light tower. In this case, the input parameters required for the application were already available from previous studies.

In particular, the analysis of the wind field at the site was carried out by Pagnini et al. (2015). The local climate shows prevalent sectors almost orthogonal to the coastal line (Figure 5.6a). The most frequent direction, from the land, is characterized by large turbulence due to the complex orography behind the city of Savona. Some frequent sectors from the sea produce smooth wind. The presence of the Mediterranean Sea gives a prevalence of unstable atmospheric conditions. The roughness map of the site is reported in Figure 5.6b. The aerodynamic coefficients of the wind turbine instead were provided by the designer. The dynamic identification was carried out by Pagnini et al. (2018) and it is discussed in the following section.

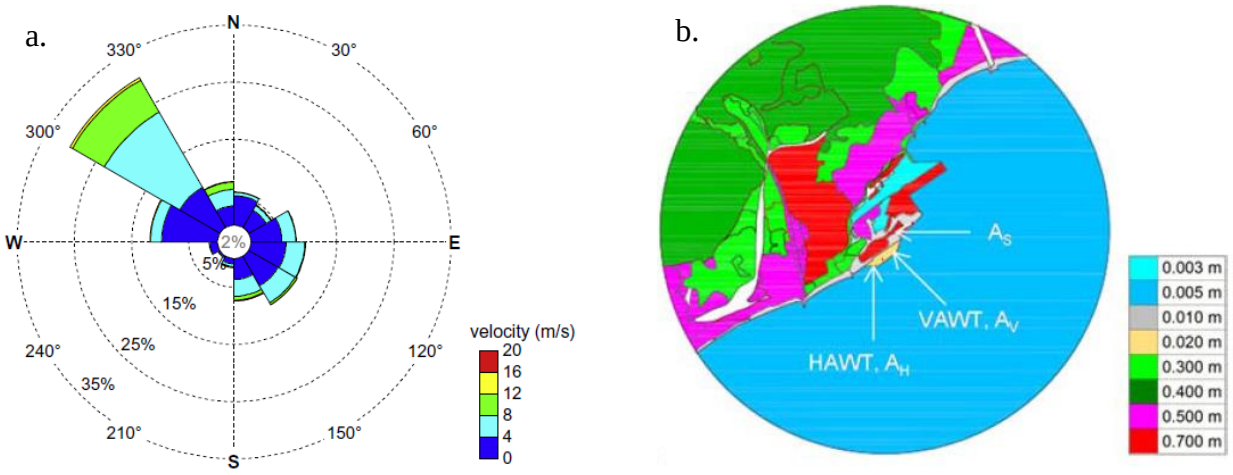

Figure 5.6. Wind rose (a) and roughness map (b) of wind turbine's site. From Pagnini et al. (2015).

5.3.1 Dynamic identification

Under the guidance of FEM outcomes, vibration modes and dynamic parameters in parked conditions were identified from the analysis of the acceleration records (Figure 5.7). The FEM results are summarized in Table 5.1.

The first vibration mode reproduces the principal bending mode of a cantilever beam. The fundamental frequency is n_1=1.47 Hz. The second vibration mode concerns flatwise bending of the horizontal arms supporting the blades, vibrating both in-phase and out-of-phase. Fundamental frequency is n_2=2.55 Hz; Mode No. 3 reproduces the torsional mode of the shaft. The fundamental frequency has been identified as n_3=7.43 Hz.

The structural damping has been estimated for the first (ξ_1) and the third vibration mode (ξ_3), which are the ones related to the supporting pole. Results obtained revealed that these damping values are evanescent in absence of wind and rotation (i.e., $\xi_1 \cong 0.1\%$, $\xi_3 \cong 0.22\%$). Damping increases with the wind speed, even in parked condition, due to the relevant aerodynamic contribution of the supporting pole and the blades, up to ξ_1=0.9% and ξ_3=1% at 48 rotations per minute (rpm), which is the maximum rotational velocity.

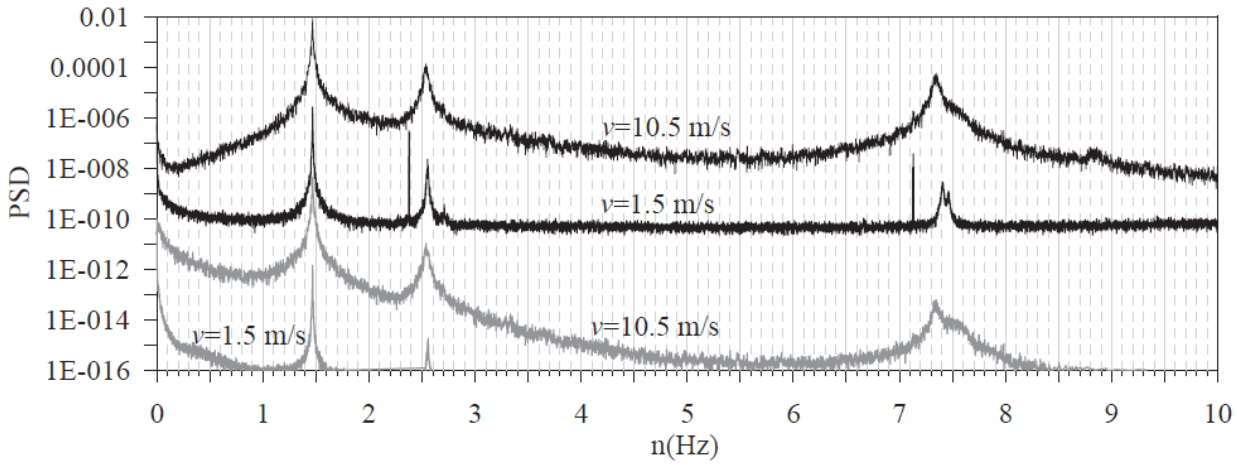

Figure 5.7. PSD of the top acceleration (black line) and base strain (grey line) in parked conditions. From Pagnini et al. (2018).

Table 5.1. Mode shapes and frequencies of the FEM. From Pagnini et al. (2018).

mode number	1	2		3
Description	tower bending	flatwise of blade holders		tower torsional
mode shape	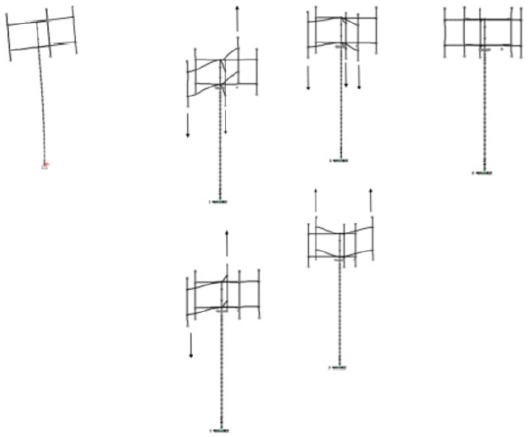			
frequency (Hz)	1.51	between	3.27–3.37	6.33

5.3.2 Full scale validation

As for the light tower, the response calculations are analysed against the full-scale measurements to assess the capability of the model to predict the actual wind-induced response. In particular, the validation is useful to assess the suitability of the calculation model for parked small wind turbines. Indeed, the model is not calibrated to take into account the presence of non-localized masses (the blades) and flexible sub-entities (the blade-supporting arms).

In this case, only one accuracy level has been considered, assuming as entry parameters the values defined in the previous studies. Therefore, only model bias is evaluated.

The comparison is still operated in terms of mean and maximum top displacements of the tower over time intervals of length T=10 minutes. The measured displacements have been obtained by combining strain and acceleration measurements according to the method defined in Section 2.5.

In this case, considering the polar symmetry of the structure and the few available time intervals where the turbine is parked, all wind directions are considered paying attention to separate land winds from sea winds. Therefore, suitable homogeneous stationary wind events have been extracted by imposing:

- 1-hour gust factor $G_{60} < 1.8$;
- standard deviation of wind direction $\sigma_\alpha < 15°$;
- mean wind direction $\bar{\alpha}$ from sea sectors ($270° < \bar{\alpha} < 360°$) or from land sectors ($60° < \bar{\alpha} < 210°$), see Figure 5.6a.

Bias of the prediction is estimated through the mean absolute percentage error (MAPE). Again, due to high noise levels at the low velocities, the first two or three bins are excluded from the bias calculation, depending on the considered case.

Figures 5.8/5.13 show the results of the validation. Every dot is representative of a 10-minutes interval, and the filled dots are the averaged values in the velocity intervals. The grey plot represents the percentage error of every velocity bin.

At first glance it is observed a great variability of the measured response. Despite it seems more evident for the land winds (Figures 5.8, 5.9, 5.12), where the number of available samples is uniform for every velocity bin, actually the sea wind responses are equally dispersed around their mean values (Figures 5.10, 5.11, 5.13).

In the case of sea winds, the variability of measured responses is uniformly large for every velocity bin. However, in terms of averaged values the comparison shows a good agreement between measurements and predictions (Figures 5.10, 5.11, 5.13), especially in the velocity intervals with lots of samples ($\bar{u}$<6 m/s). The large MAPE obtained for the alongwind mean response (83.9%, Figure 5.10) is mainly due to errors in a single velocity bin where only few samples are available.

Differently, as regards land winds, the variability increases largely with wind velocity. This result suggests that two or more different response trends are considered together, despite not being detected by the analytical predictions (Figures 5.8, 5.9, 5.12). This effect can be possibly attributed to the different atmospheric stability between day and night, or to the non perfect polar-symmetry of the structure. However, in terms of averaged values the discrepancy arises only at the highest velocities (Figures 5.9-5.12 are emblematic), where possibly only one response mechanism is present. In this respect, the next phase of the research will deal with the enhancement of the validation from a better separation of homogeneous wind events.

In the overall, the outcomes show a predictable greater error with respect to the first case study (Section 4.6). Indeed, the calculation model consider the localized masses as rigid and compact entities, while the rotor is flexible and distributed in space. However, considering the relevant uncertainties, these early results look very promising for a generalization of the model to small wind turbines.

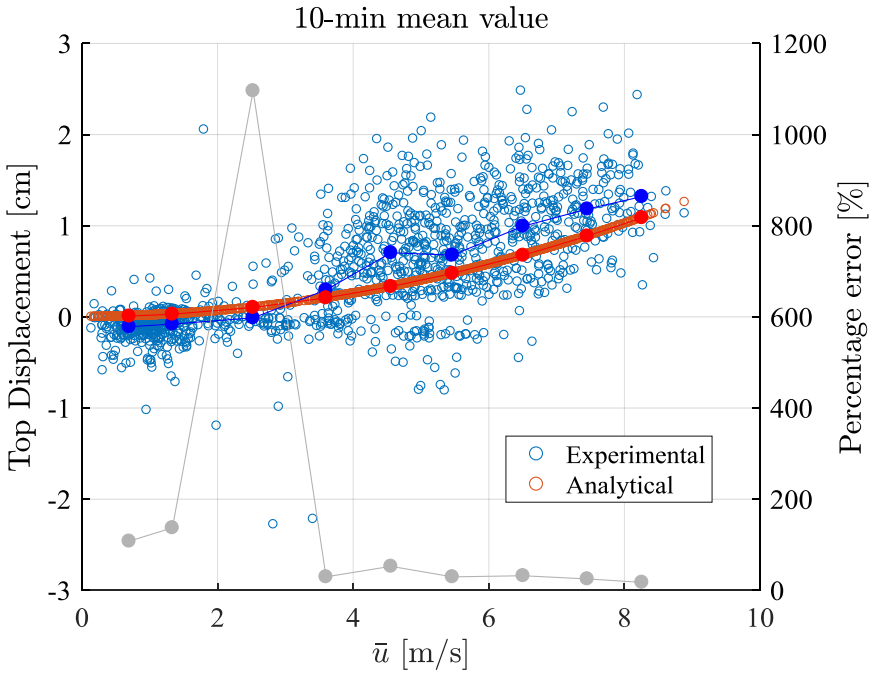

Figure 5.8. Comparison of alongwind mean displacements (parked conditions), wind blowing from the land. MAPE=31.1%.

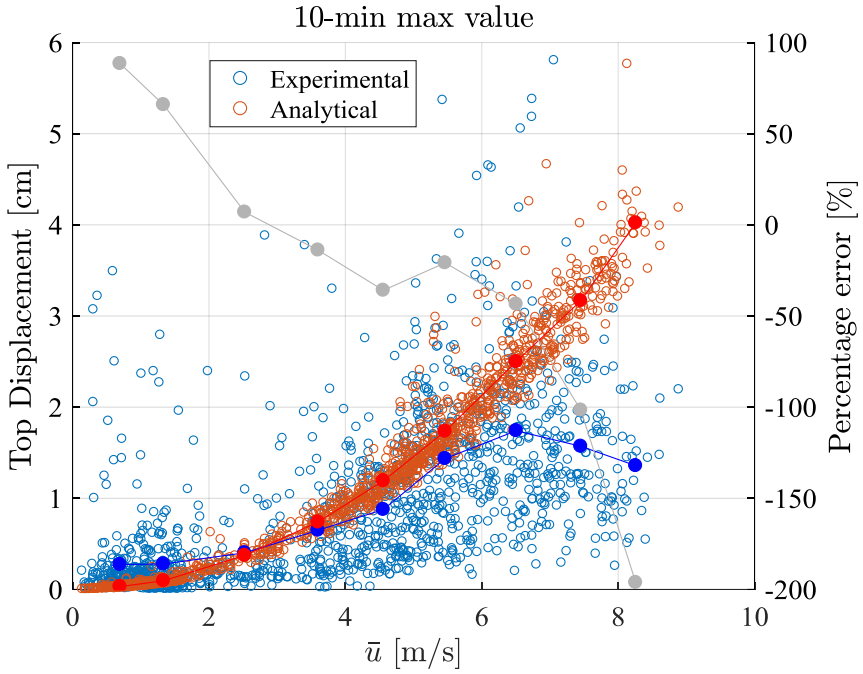

Figure 5.9. Comparison of alongwind maximum displacements (parked conditions), wind blowing from the land. MAPE=59.8%.

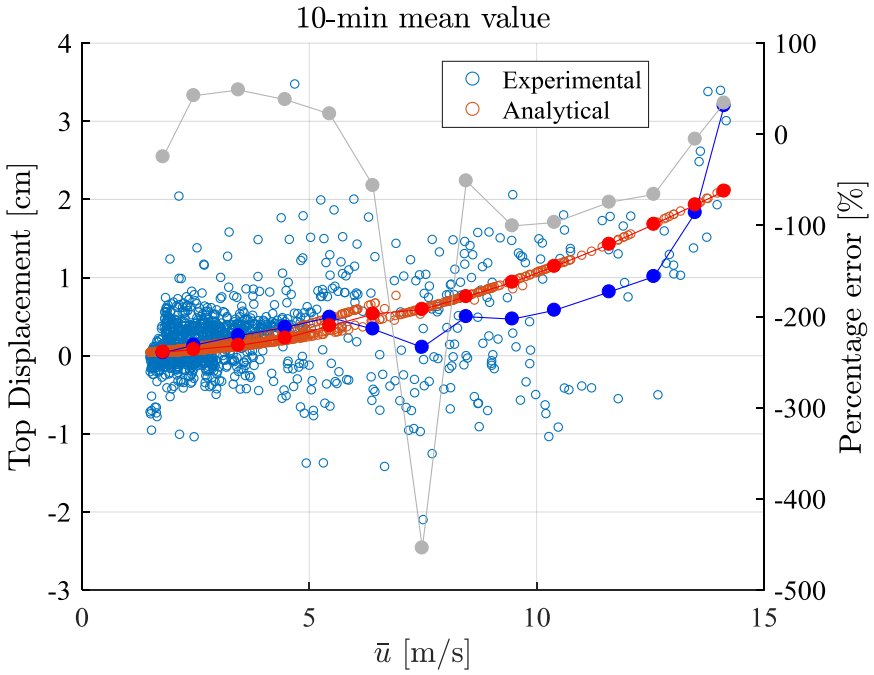

Figure 5.10. Comparison of alongwind mean displacements (parked conditions), wind blowing from the sea. MAPE=83.9%.

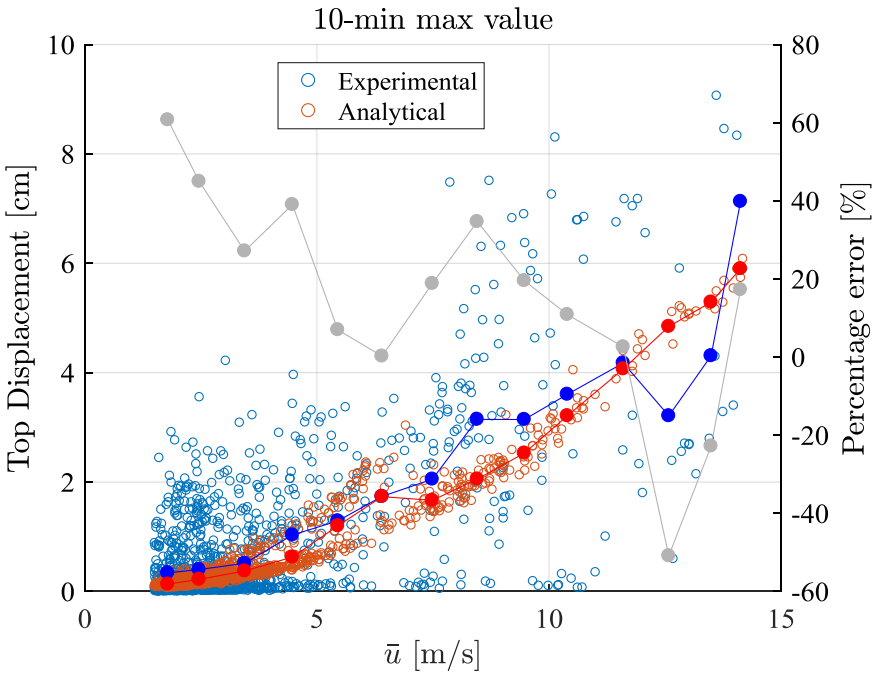

Figure 5.11. Comparison of alongwind maximum displacements (parked conditions), wind blowing from the sea. MAPE=23.7%

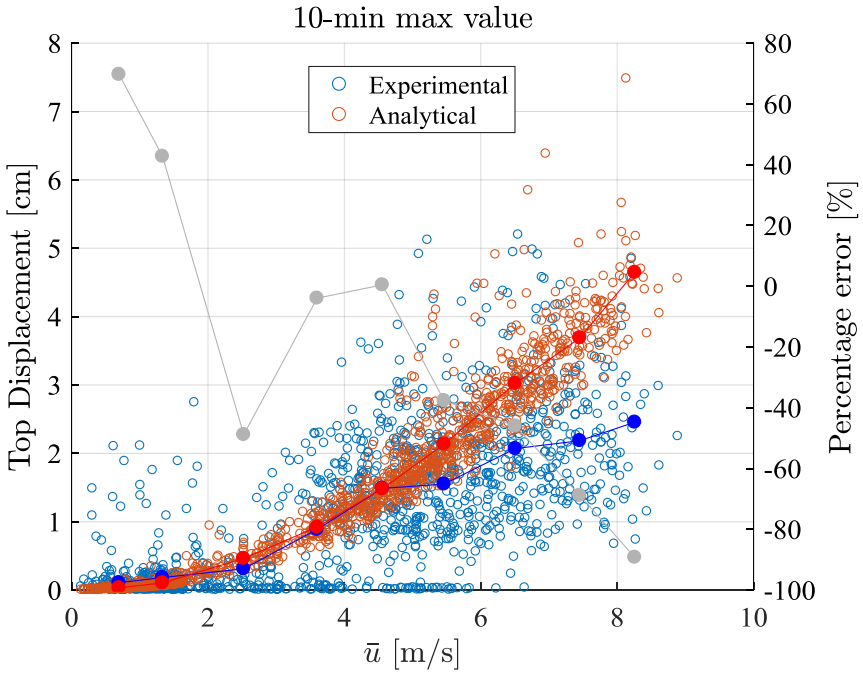

Figure 5.12. Comparison of crosswind maximum displacements (parked conditions), wind blowing from the land. MAPE=42.1%.

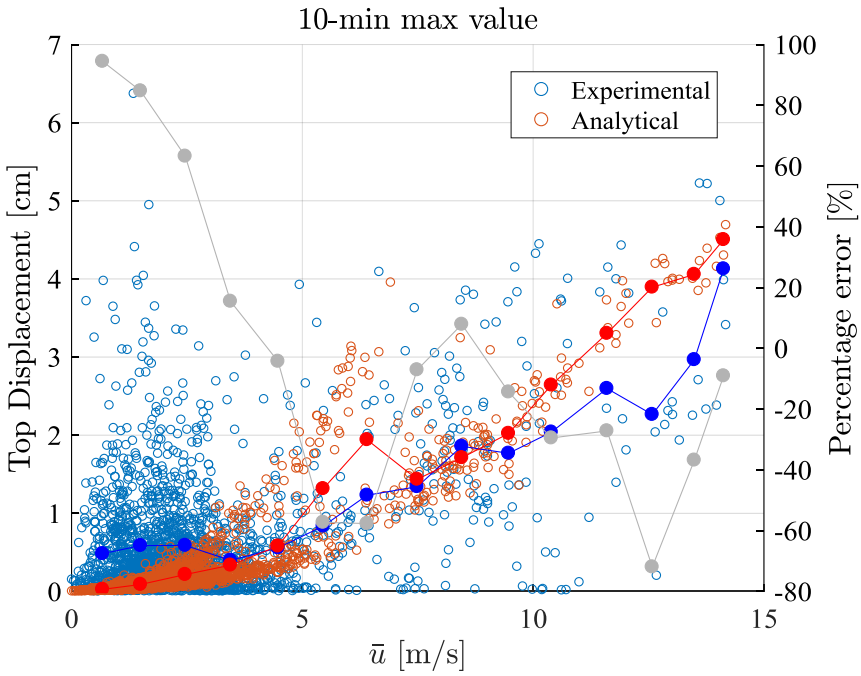

Figure 5.13. Comparison of crosswind maximum displacements (parked conditions), wind blowing from the sea. MAPE=28.2%.

5.4 Effects of rotation

After studying the wind turbine in parked conditions, the full-scale data have been devoted to the investigation of the dynamic behavior in rotating conditions. With respect to operative small wind turbines, this step constitutes a fundamental premise to generalize the calculation model of monotubular towers to the considered typology.

The investigation starts from the analysis of the harmonic content of the structural response. Figure 5.14 shows the PSD of three acceleration records with time length T=10 minutes. The first one (Figure 5.14a) has been recorded with the parked turbine; the second one (Figure 5.14b) with turbine rotating at 16 rotations per minute (*rpm*), the third one rotating at 48 *rpm* (Figure 5.14c).

5.4.1 Rotationally sampled spectrum

The first observed effect on the dynamic response regards the harmonic content of wind loading. As indicated by the blue arrows, peaks of the structural response are observed at frequencies that are multiple of the rotational frequency *P*, defined as:

$$P = \frac{rpm}{60} \quad [\text{Hz}] \tag{5.1}$$

In particular, peaks at 1*P* and 5*P* are observed for every rotational velocity, while at the maximum velocity (48 *rpm*) also a peak at 10*P* is visible.

These peaks are due to the fact that the wind loading on the wind turbine is “sampled” by the rotation of the rotor; the resulting spectrum is known as rotationally sampled wind spectrum (Murtagh et al., 2005). Due to the rotation of the blades, the spectral energy distribution of wind loading is altered, with variance shifting from the lower frequencies to peaks located at multiples of the rotational frequency.

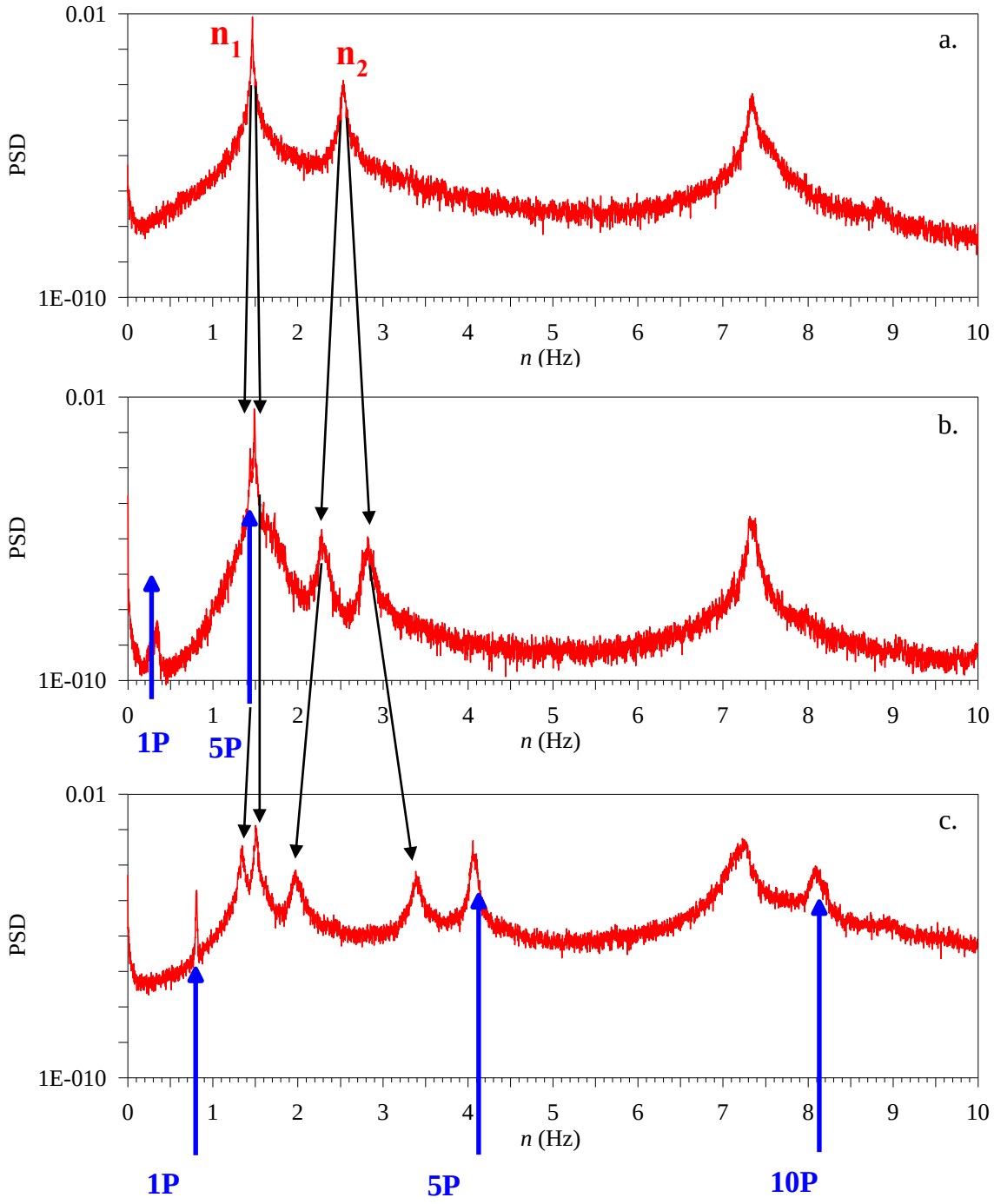

Figure 5.14. PSD of acceleration records. Turbine rotating at 0 rpm (a), 16 rpm (b) and 48 rpm (c).

Even if it is based always on the same principle, such effect can differently affect the harmonic content of the response whether the turbine is vertical or horizontal axis, and whether we are studying the response of a blade or the global effect on the supporting tower. For example, a blade of a horizontal axis turbine passes periodically from locations with higher mean wind velocity to locations with lower mean velocity, since it reaches different heights during the rotation. This effect clearly is not present in case of vertical axis.

Some studies have dealt with the quantification of the rotationally sampled spectrum of horizontal axis wind turbines. Kristensen and Frandsen (1982), following on from the work by Rosenbrock (1955), developed a simple model to predict the power spectrum associated with a rotating blade.

Murtagh et al. (2005) developed a method to calculate the alongwind response of the supporting tower taking into account such effect, following the work by Madsen and Frandsen (1984). Other significant works on this topic are by Hardesty et al. (1981) and by Sørensen (2002).

However, to the best of author's knowledge, no documented studies have reported how such phenomenon affects the harmonic loads on vertical axis wind turbines, neither from a quantitative nor from a qualitative viewpoint. The following paragraphs aim to address partially this issue, describing qualitatively the nature of such effect for this structural typology.

If we imagine even a constant wind speed with no harmonic content acting on the vertical axis wind turbine, it is clear that the wind loading varies with time, since the rotation changes the aerodynamic force coefficients of the rotor over time. The aerodynamic force coefficients become a function of time, and they are periodic: indeed, considering a reference position occupied by a blade at instant t_0, every time another blade passes through the reference position, the same configuration of the rotor is restored, with resulting same aerodynamic behavior. The period T is the time between two consecutive passages in the reference position, so it depends on the rotational velocity and the number N of the blades according to:

$$T = \frac{1}{NP} \quad [\text{s}] \tag{5.2}$$

The correspondent frequency is thus equal to NP, which in our case in 5P, that indeed is the frequency with the highest energy content among the peaks due to this effect (Figure 4.1b-c, PSDs are in logarithmic scale).

However, considering the small inequalities between the blades, the exact aerodynamic behavior of the rotor is replicated every time a complete rotation of the rotor occurs. Therefore a smaller harmonic content, with frequency 1P, appears.

Lastly, in a period that is half of T, it occurs that the rotor configuration is mirrored with respect to the reference one. If the blades' cross-section was doubly symmetric, neglecting the influence of the supporting arms and other nonlinear effects, the aerodynamic coefficient of the rotor would be equal to that of the reference configuration. Actually, blades' cross-section is not doubly symmetric but it is not far from being it. Therefore, this could be a reason for the peak at 10-P. However, the presence of peaks beyond 5P must still be deeply investigated.

These are the peaks that have been observed but, depending on the single case study, also other peaks at frequencies that depends on P could be observed, for example if there is greater similarity between non-consecutive blades, due to defects and imperfections of a particular blade.

5.4.2 Splitting of natural frequencies

As a second effect of rotation, a splitting of the frequencies of the first mode (bending mode of the tower) and second mode (bending mode of the blade arms) is observed in Figure 5.14.

The effect on the blade mode is well documented in literature (see Carne et al. 1982, Hansen 2007, Bir, 2010) and it is due to the fact that we are measuring in a fixed reference system (the one of the accelerometer) an effect of the vibration of a rotating component (the blade). Indeed, even from modal analysis it seems to be exclusively a rotor mode, actually it involves some small motions of the tower, otherwise it would not be detected by the accelerometer, and this motion of the tower is influenced by the position of the rotor (Figure 5.15).

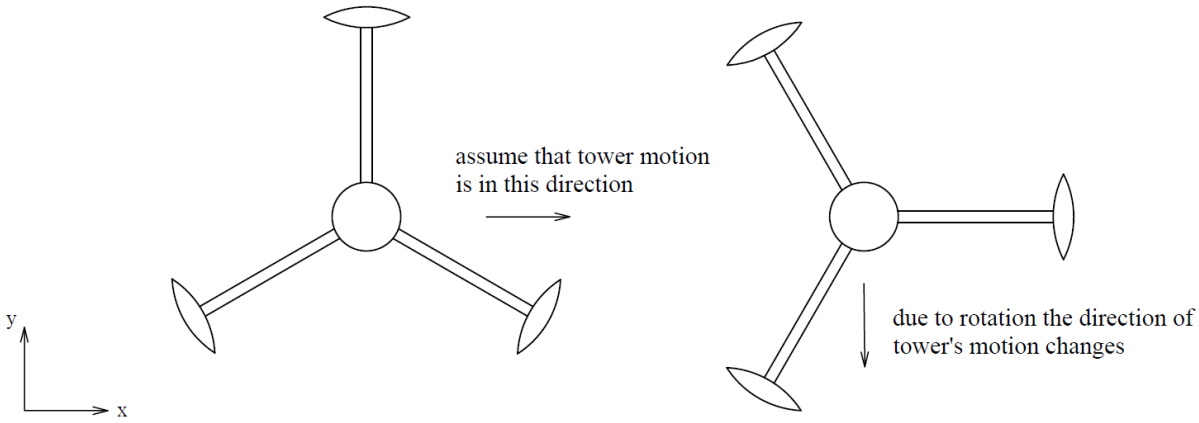

Figure 5.15. Effects of vibrations of rotating components on the supporting tower.

The sinusoidal displacement is therefore modulated by the rotation, leading to a split of the energy content at two frequencies that are symmetric to the standard one (of the parked turbine). Indeed, according to the *Werner formulas*, the displacement of the tower in x direction due to the considered mode is:

$$x(t) = A\cos(\omega_0 t)\cos(2\pi P t) = \frac{A}{2}\cos((\omega_0 + 2\pi P)t) + \frac{A}{2}\cos((\omega_0 - 2\pi P)t) \tag{5.3}$$

$$\omega_0 = 2\pi f_0 \tag{5.4}$$

where f_0 is the natural frequency of the considered mode. Therefore, it is clear that the harmonic content of the response concentrates at two frequencies that are equal to $f_0 - P$ and $f_0 + P$.

Instead, the splitting of tower's bending mode is rarely dealt in literature (McLaren et al., 2012) where it is possibly attributed to the gyroscopic effect. Therefore, the next section aims to investigate the causes of this effect by developing a simple analytical model of the free undamped vibrations of a 2-degree of freedom (2DOF) system.

5.4.3 Investigation of gyroscopic effect

In order to analyze the gyroscopic effects on tower's bending mode, the vertical axis wind turbine has been modeled as a 2DOF system (Figure 5.16), i.e. the rotor is considered as a point-like system able to move in the *xy* plane. Therefore, no vibrations of the rotating parts are investigated in this formulation and centrifugal forces are thus disregarded. The rotor mass *m* is subject to a rotational velocity Ω, intended as an angular velocity, and it is characterized by a mass moment of inertia *I*. The tower, with height *h*, contributes only to the stiffness of the system, equal to *k*, which is identical for every direction because of the polar-symmetry of the structure.

While vibrating, if *m* moves in the *x* direction (thus has a velocity $\dot{x}$), it tends to incline the rotation axis with an angular velocity $\dot{x}/h$. As a result, it undergoes a gyroscopic moment M_x in the *yz* plane that is equal to:

$$M_x = \frac{I\Omega\dot{x}}{h} \tag{5.5}$$

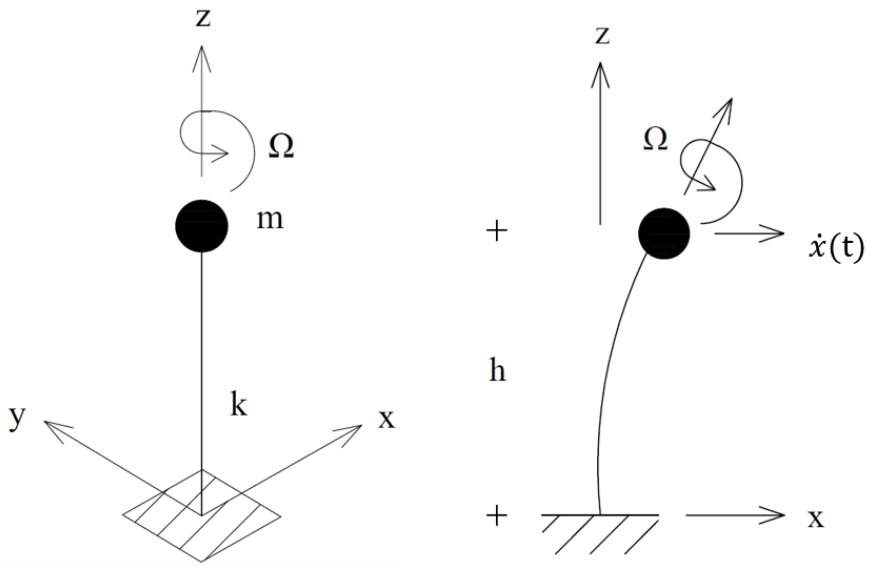

Figure 5.16. 2DOF model of the vertical axis wind turbine.

Which can be converted to a gyroscopic force F_y acting on m in y-direction:

$$F_y = \frac{I\Omega\dot{x}}{h^2} \tag{5.6}$$

The same effect occurs in y-direction. The equations of motion in the xy plane become:

$$\begin{cases} -kx + \dfrac{I\Omega}{h^2}\dot{y} = m\ddot{x} \\ -ky - \dfrac{I\Omega}{h^2}\dot{x} = m\ddot{y} \end{cases} \qquad \begin{cases} \ddot{x} - \eta\dot{y} + \omega_0{}^2 x = 0 \\ \ddot{y} + \eta\dot{x} + \omega_0{}^2 y = 0 \end{cases} \tag{5.7}$$

with $\omega_0 = \sqrt{k/m}$ circular frequency of the system in absence of rotation and $\eta = I\Omega/mh^2$.

Equation 5.7 describes the free undamped vibrations of the system. They are two coupled 2nd order differential equations, linear, homogeneous and with constant coefficients. To solve the system, the displacement are considered as characterized by two different frequency contributions, as observed from the measurements, with amplitude coefficients that recalls each other in the two directions:

$$\begin{aligned} x(t) &= A\cos(\omega_1 t) + B\sin(\omega_1 t) + C\cos(\omega_2 t) + D\sin(\omega_2 t) \\ y(t) &= B\cos(\omega_1 t) - A\sin(\omega_1 t) - D\cos(\omega_2 t) + C\sin(\omega_2 t) \end{aligned} \tag{5.8}$$

Imposing Eq. (5.8) into Eq. (5.7) we obtain:

$$\begin{cases} -A\cos(\omega_1 t)(\omega_1{}^2 - \eta\omega_1 - \omega_0{}^2) - B\sin(\omega_1 t)(\omega_1{}^2 - \eta\omega_1 - \omega_0{}^2) + \\ -C\cos(\omega_2 t)(\omega_2{}^2 + \eta\omega_2 - \omega_0{}^2) - D\sin(\omega_2 t)(\omega_2{}^2 + \eta\omega_2 - \omega_0{}^2) = 0 \\ -B\cos(\omega_1 t)(\omega_1{}^2 - \eta\omega_1 - \omega_0{}^2) + A\sin(\omega_1 t)(\omega_1{}^2 - \eta\omega_1 - \omega_0{}^2) + \\ +D\cos(\omega_2 t)(\omega_2{}^2 + \eta\omega_2 - \omega_0{}^2) - C\sin(\omega_2 t)(\omega_2{}^2 + \eta\omega_2 - \omega_0{}^2) = 0 \end{cases} \tag{5.9}$$

Therefore, the system is solved as long as:

$$\begin{aligned} \omega_1^2 - \eta\omega_1 - \omega_0^2 = 0 \\ \omega_2^2 + \eta\omega_2 - \omega_0^2 = 0 \end{aligned} \tag{5.10}$$

which leads to the definition of the circular frequencies of the system:

$$\begin{aligned} \omega_1 = \frac{\eta \pm \sqrt{\eta^2 + 4\omega_0^2}}{2} \\ \omega_2 = \frac{-\eta \pm \sqrt{\eta^2 + 4\omega_0^2}}{2} \end{aligned} \tag{5.11}$$

Since the circular frequencies are assumed to be positive values we finally obtain:

$$\begin{aligned} \omega_1 = \frac{\eta + \sqrt{\eta^2 + 4\omega_0^2}}{2} = \omega_0\sqrt{1+\left(\frac{\eta}{2\omega_0}\right)^2} + \frac{\eta}{2} \\ \omega_2 = \frac{-\eta + \sqrt{\eta^2 + 4\omega_0^2}}{2} = \omega_0\sqrt{1+\left(\frac{\eta}{2\omega_0}\right)^2} - \frac{\eta}{2} \end{aligned} \tag{5.12}$$

These are the circular frequencies of the 2DOF system with gyroscopic effect. It is straightforward to observe that, for Ω=0, which results in η=0, ω_1 and ω_2 coincides and are equal to ω_0. Moreover, it is interesting to highlight the effect of Ω on the calculated frequencies. It follows that:

$$\begin{aligned} \omega_1 - \omega_2 = \eta \\ \frac{\omega_1 + \omega_2}{2} = \omega_0\sqrt{1+\left(\frac{\eta}{2\omega_0}\right)^2} \end{aligned} \tag{5.13}$$

So, both the distance between the peaks and the central frequency increase with increasing the rotational velocity (Figure 5.17).

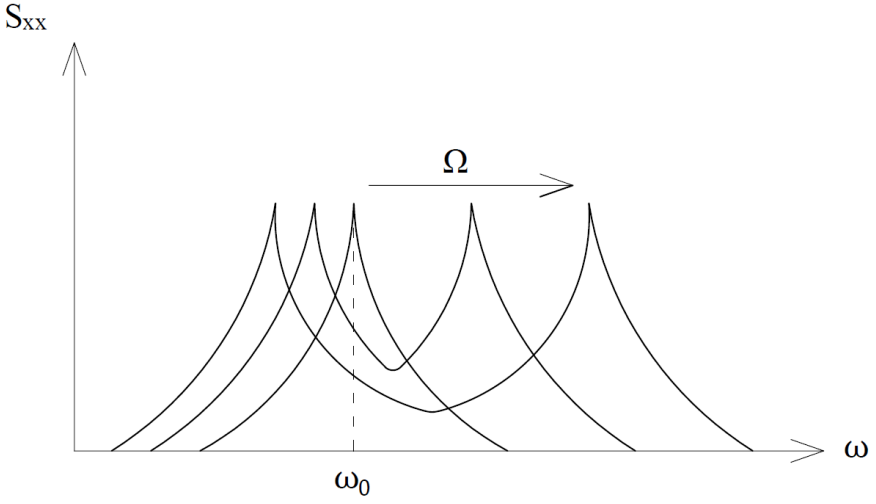

Figure 5.17. Effects of rotational velocity on the frequencies of the system with gyroscopic effect.

Finally, the initial conditions are imposed to obtain the amplitude of the sinusoids composing the displacements:

$$\begin{cases} x(0) = x_0 \\ \dot{x}(0) = \dot{x}_0 \\ y(0) = y_0 \\ \dot{y}(0) = \dot{y}_0 \end{cases} \tag{5.14}$$

and we obtain:

$$\begin{aligned} A &= \frac{\omega_2 x_0 - \dot{y}_0}{\omega_1 + \omega_2} \\ B &= \frac{\omega_2 y_0 + \dot{x}_0}{\omega_1 + \omega_2} \\ C &= \frac{\omega_1 x_0 + \dot{y}_0}{\omega_1 + \omega_2} \\ D &= \frac{-\omega_1 y_0 + \dot{x}_0}{\omega_1 + \omega_2} \end{aligned} \tag{5.15}$$

Again, when rotation is null, the coefficients coincide with the ones of the 2DOF system without gyroscopic effect.

The original analytical formulation carried out in this section confirms that the gyroscopic effect produces a splitting of the bending mode of the tower. In the next step, damping will be introduced and the formulation will be validated in full-scale. This represents the first step towards the development of a simplified model of the dynamic response of the wind turbine, through the generalization of the reference analytical model for fixed-masses systems (Solari and Pagnini, 1999) to rotating-masses systems, which remains as a perspective of the present work.

5.5 Fatigue assessment

Lastly, full-scale measurements from the wind turbine are used to apply standard fatigue calculation model for small wind-turbines (IEC 61400-2, 2013). This section discusses the response and fatigue damage of the supporting tower of the wind turbine subject to stationary and non-stationary excitation due to wind, turbine rotation, emergency stop and start. The aim of this section is to analyze a number of aspects that are usually disregarded in fatigue design verifications; in particular it highlights the fundamental role played by the non-stationary conditions and the errors committed when using conventional models of the load.

5.5.1 Literature review

The structural verification of small size wind turbine is regulated by the standard IEC 61400-2 (2013) which provides three ways to derive the structural loads: a simplified analytical model, numerical simulations and full-scale measurements. Usually the design is carried out according to the simplified model that allows the derivation of the structural loads considering simplified external conditions. Even if this procedure is allowed for the horizontal axis configuration, sometimes it is also applied to

the vertical axis, due to the lack of a well-established method for this technology. With regard to the fatigue analysis, which is in many cases the most severe limit state, the simplified load model assumes a constant load amplitude for the whole lifetime of the structure. This load range is provided on the basis of a number of input parameters that take into account the rotation of the blades only, disregarding wind induced vibration. Moreover, wind turbulence models supplied by the guidelines can be unsuited for use in urban sites and the fatigue loading may be greater than that predicted by the standard spectra (KC et al., 2019, 2020). Therefore, uncertainties arising from this approach are huge (Evans et al., 2018).

When using numerical simulations or full scale measurements, the fatigue analysis is based on the 'state approach', which decomposes the wind stochastic process into independent loading conditions characterized by given mean wind speed, mean wind direction and turbine operating condition. For each loading condition, the fluctuating part of the effect induced by the wind turbulence (Jang et al., 2015) is modeled by a stationary Gaussian process superimposed to the static part of the effect induced by the mean wind velocity. Generally, only few short-term simulations or few samples of load measurements are taken into account; the total damage related to the whole loading condition is obtained by extrapolating the results through the probability of the load occurrence.

Regardless of the procedure used to evaluate the structural loads (measurements or simulations), some questionable issues affect the use of the state approach in the evaluation of the fatigue damage. Firstly, since the state approach decomposes the wind process into a series of independent loading conditions, the low-frequency large-amplitude cycles related to the macro-meteorological fluctuation of the wind speed are completely disregarded as well as the transition cycles from two consecutive loading conditions, as highlighted by Sutherland (1999). Secondly, since the loading condition is extrapolated by a limited number of short-term time-history samples, the stochastic variability of the partial damage related to the samples strongly affects the total damage (Jia, 2014, Moriarty et al., 2004, Cao et al., 2018). Due to the strong non-linearity of the fatigue phenomenon, such uncertainties can compromise the reliability of the fatigue analysis. Sutherland (1999) demonstrated that the damage associated to the same loading condition, evaluated on the basis of different 10-min simulated time history samples, can vary by two orders of magnitude.

The non-stationarity and non-Gaussianity in wind load as well in the load due to operational conditions in wind turbines has remarkable effect on the response of main structures and sub-assemblies (Kwon et al., 2012, Gong & Chen, 2014). Non-stationarity can arise from transient wind phenomena (hurricanes, thunderstorms, tornadoes), turbulence, or from rotor emergency stop and start, yaw, blade pitch. (i.e. Zhou et al., 2014, Chen at al., 2020, Liu et al., 2020). Wind turbulence in complex terrain often exhibits non-Gaussian characteristics, with some isolated non-Gaussian wind events much higher than prediction (Tabrizi et al., 2017). Also for these reasons, fatigue represents a frequent failure type of wind turbine incidents. Working in the classical frequency domain, Capponi et al. (2017) investigated the rate of non-stationarity that can be relevant in the fatigue life performing experimental tests at different level of non stationarity showing that fatigue life significantly decreases. Experiments have been performed over an aluminium alloy specimen excited by a simulated signal. Authors quantify a non-stationarity index of the signal to detect when the fatigue problem can be analyzed with the classic frequency-domain approach. When the excitation is also non-Gaussian, the obtained fatigue life exhibits an even higher damage accumulation (Palmieri et al., 2017). Cianetti et al. (2017) supply a correction coefficient for the fatigue damage based on the kurtosis and the skewness of the input; Wolfsteiner (2017) proposes a procedure in which the non-stationary non-Gaussian fatigue load is expressed as a combination of stationary Gaussian signals. Li

et al. (2021) suggest a time history simulation method for calculating the dynamic stress of structures in resonance state under non-stationary condition.

Whatever method is used to carry out the fatigue analysis, a further source of uncertainty in the damage assessment arises when the similarity between the structural detail to be investigated and the ones classified by the technical standards is poor. In this case, the use of inappropriate detail for the resistance assessment may lead to neglect the effect of geometrical peculiarities in the fatigue fracture initiation and propagation, leading to unreliable estimation of the damage (Savaidis & Vormwald, 2000).

Starting from these premises, this final section of the thesis deals with the fatigue assessment of the supporting tower of the small wind turbine, under stationary and non-stationary events. Two recorded events, representative of the turbine behavior under stationary and non-stationary loading conditions, are selected and analyzed. After defining the fatigue resistance of the critical structural details, the fatigue damage associated to the two selected events is computed. The effects of fatigue resistance, non-stationarity and sample time length on the accumulated damage are quantified and discussed.

5.5.2 Wind field and structural behavior

The analysis of the structural response under different wind and operative conditions is carried out analyzing simultaneous measures of wind velocity, accelerations and strains.

Figure 5.18 shows the 10-min standard deviation of the measured strain at the bottom of the shaft (strain gauges n° 5-8) in the along-wind direction against the 10-min mean wind speed, $\bar{u}$. Data are divided into land (Figure 5.18a) and sea sectors (Figure 5.18b) according to the inflow wind direction. Red dots represent the strain measured when the turbine is rotating and dashed grey line represents the average value calculated over velocity bins 1 m/s wide. Blue dots represent the strain in parked condition, when the turbine is not operating (i.e., at low wind speed under the cut-in value, at high wind speed, gusts and downtimes); dotted grey line reports the average value calculated over velocity bins 1 m/s wide. The vertical dotted lines mark the cut-in and cut-out wind velocity declared by the producer. The diagram also underlines data related to large turbulence intensity, i.e. $I_u > 0.3$.

The figures highlight some relevant aspects related to the wind and the turbine behavior. The structural response is generally higher when the wind blows from the land, as the turbulence is higher with respect to sea sectors. In the range between the cut-in and the cut-out wind speed, the strain in the rotating turbine is higher with respect to strain in standstill condition, showing that the rotation induces a significant increase of the structural stress. The most notable effect is the sudden increase of strain at the start-up, that takes place at moderate low wind speeds, and when the turbine is stopped by the control system. This situation happens usually at moderate high wind speed (generally lower than the theoretical cut-out value represented in the diagrams) that, due to gusts, reaches the instantaneous cut-out value. These two situations may give rise to critical conditions for fatigue crack initiation and propagation.

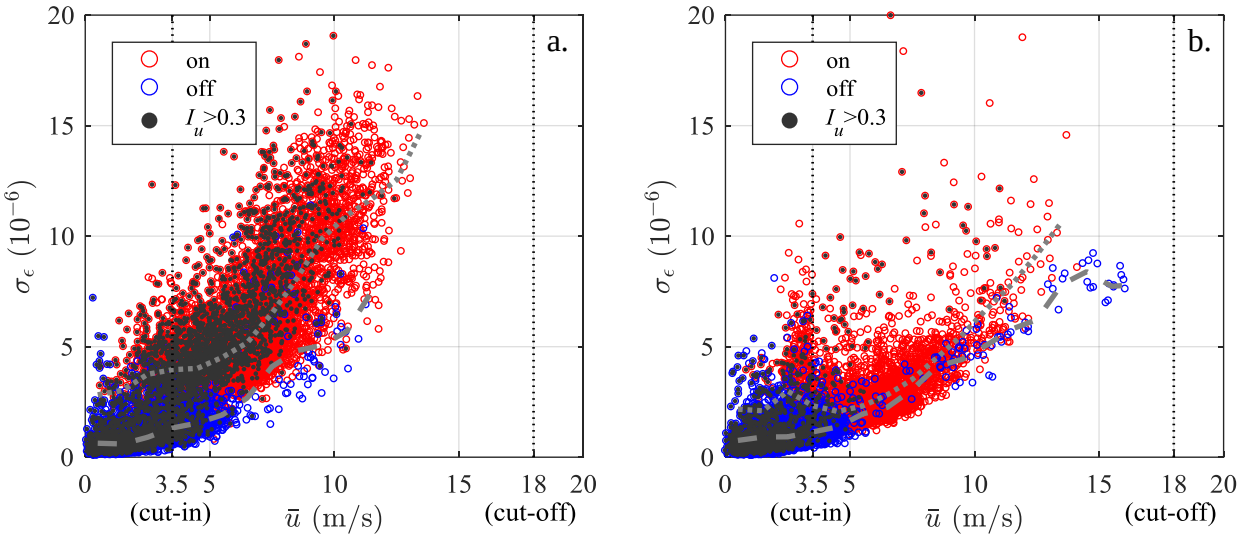

Figure 5.18. Standard deviation of structural strain at the bottom against mean wind speed coming from the land (a) and from the sea (b). Red and blue symbols respectively refer to operating and parked conditions, dotted and dashed grey lines represent the average value.

Considering all the available records, two possible situations can be outlined that may be significant with regard to the damage accumulation for fatigue. A critical condition is trivially represented by a strong persistent wind. Such condition is commonly taken into account considering structural response under stationary wind phenomena, usually represented by a stationary Gaussian turbulence process superimposed to a constant mean wind velocity. Another critical condition is the onset of very variable windy phenomena, in which low or moderate wind alternate suddenly with strong wind characterized by non-stationary conditions typical of thunderstorms and gust fronts. In this case, classical models of wind velocity and structural response are no longer suitable (EN 1991-1-4, 2005). The non-stationarity of the wind flow can induce frequent turbine stops and strong non-stationarity in the structural response.

In order to explore these critical conditions and their effects on fatigue damage, the structural response is analyzed locally by investigating two selected events that are representative of the turbine behavior.

The first event, herein referred to as Event n°1, occurred in 30 April 2018. Figure 5.19a shows the 24-hour recordings of the 10 mean wind speed $\bar{u}$ (thick line), the peak wind speed, u_p (grey line) and the wind direction (dashed line, referred to the right axis). Figure 5.19b shows the strain ε at bottom (strain gauges 1, 3, see Figure 5.4). Figure 5.19c shows the top acceleration a (accelerometers 1, 2).

Wind is quite strong all day long, persistently blowing from the South with moderate turbulence intensity and gusts. During the first time interval of the selected record, the wind speed is around 10 m/s and the turbine is generating power. At about 12.00, mean wind velocity and wind gusts grow up to 17 m/s and 25 m/s, respectively, causing the shutdown of the turbine (at 12:16) and, consequently, very large structural acceleration and strain peaks. The turbine starts rotating again from 15.37 p.m. to 15:42 p.m. and then stops. Large vibrations arise at the machine start up and shut down.

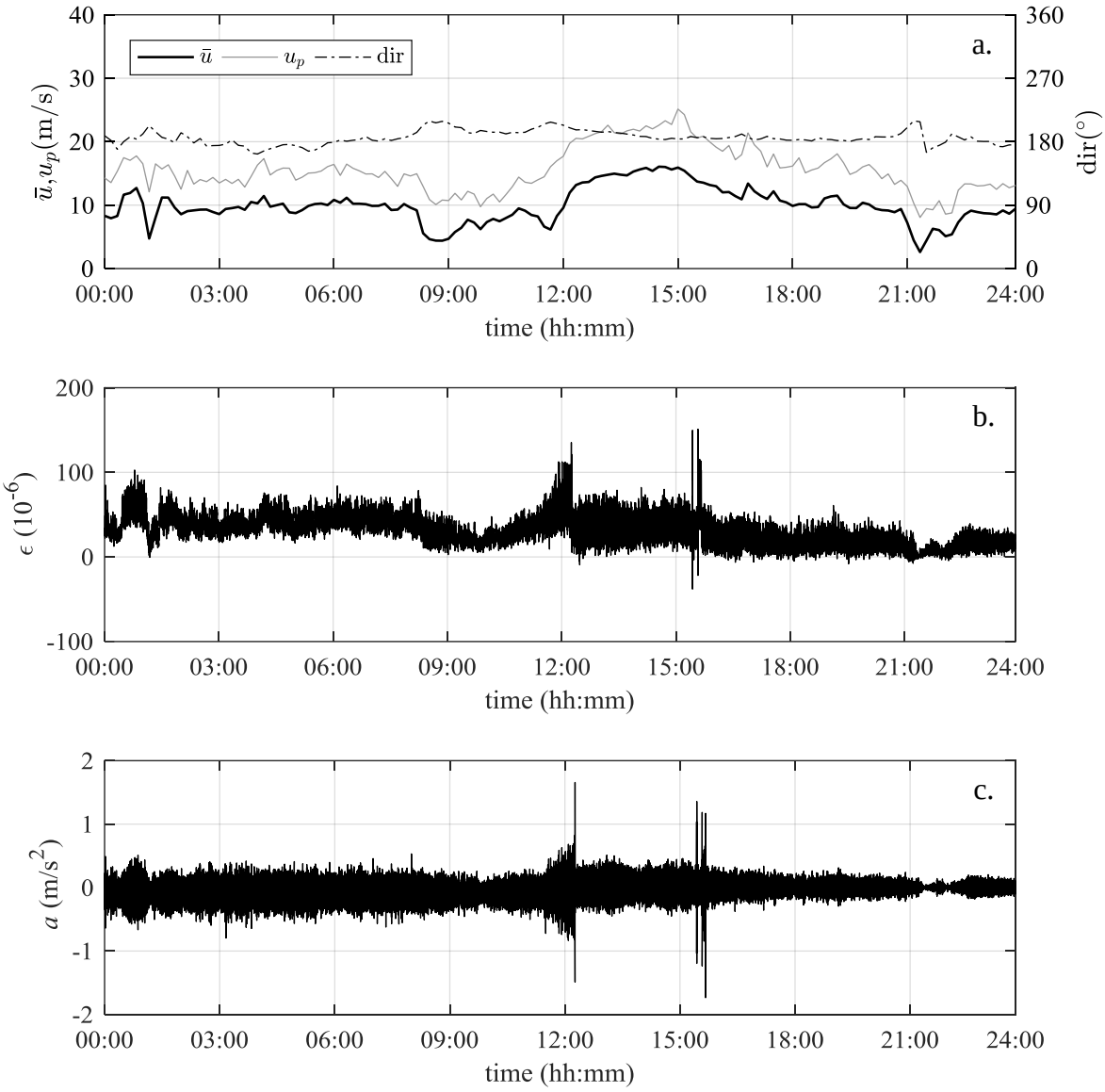

Figure 5.19. Time history of the wind speed (a), strain at bottom (b) and top acceleration (c) during 30th April 2018.

The second selected event, herein referred to as Event n°2, occurred in 3 May 2018 and it is characterized by a persistent moderate wind blowing from North at about 10 m/s. With the same meaning of symbols, Figure 5.20a,b,c shows the wind conditions, structural strain and acceleration. Despite some wind gusts exceeding 20 m/s, the turbine keeps rotating and producing power during all the time, experiencing fairly stationary structural vibrations induced by the wind and by the persistent rotation of the turbine.

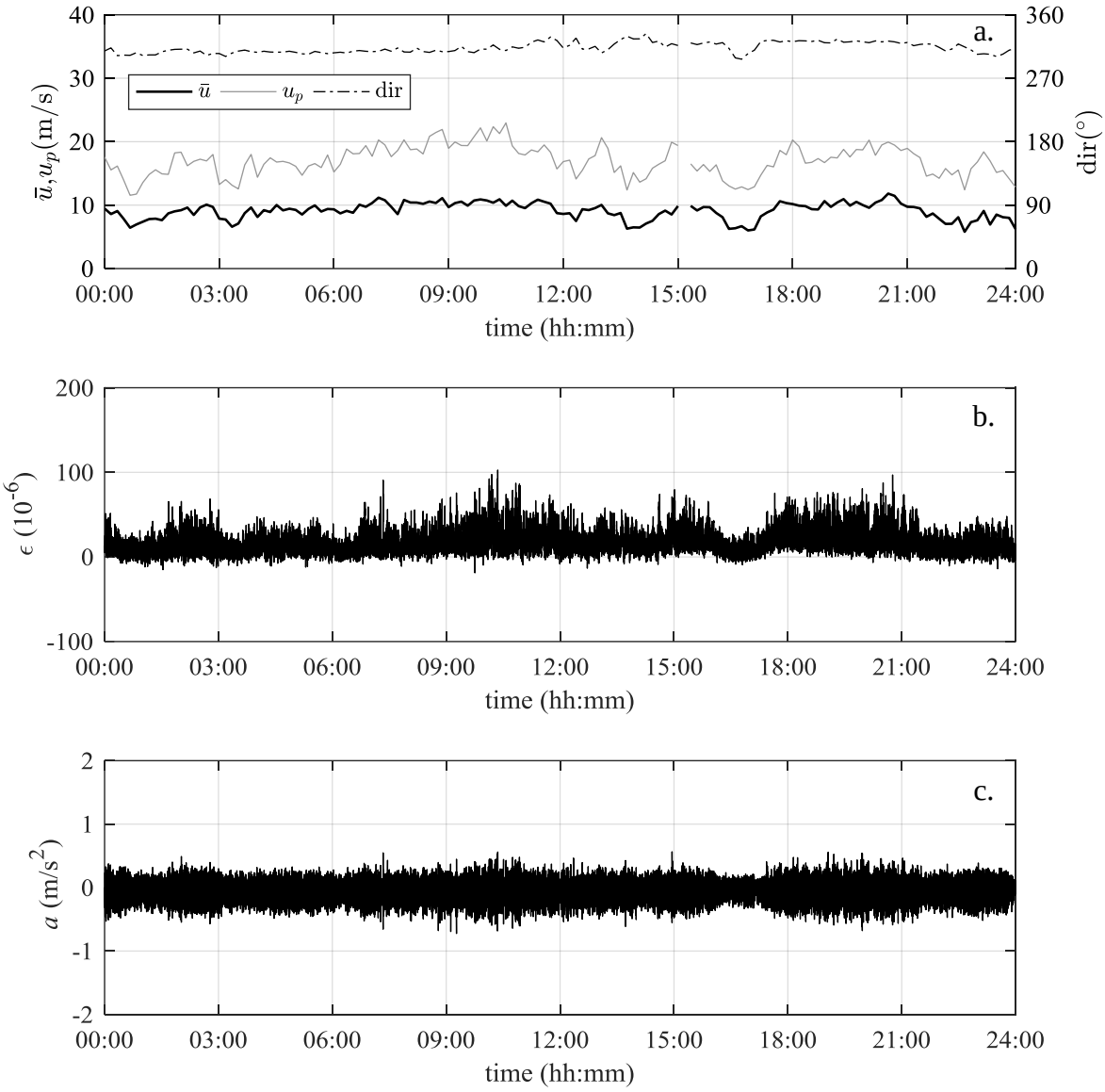

Figure 5.20. Time history of the wind speed (a), strain at bottom (b) and top acceleration (c) during 3rd May 2018.

Table 5.2 reports the average value over the whole day of the 10-min mean wind velocities, E[$\bar{u}$], of the standard deviation, E[σ_u], the absolute peak value $\hat{u}$; the average value of the 10-min mean strain, E[$\bar{\varepsilon}$], of the standard deviation, E[σ_ε], its peak value $\hat{\varepsilon}$; the average value of the 10-min standard deviation of the acceleration, E[σ_a] and its peak value $\hat{a}$.

Table 5.2. Mean, standard deviation and peak values of wind speed, strain and acceleration during the selected day.

	Wind velocity			Strain			Acceleration	
	E[$\bar{u}$] (m/s)	E[σ_u] (m/s)	$\hat{u}$ (m/s)	E[$\bar{\varepsilon}$] (10^{-6})	E[σ_ε] (10^{-6})	$\hat{\varepsilon}$ (10^{-6})	E[σ_a] (m/s^2)	$\hat{a}$ (m/s^2)
Event 1	10.0	1.3	25.1	31.7	7.6	151.0	0.08	1.66
Event 2	9.1	1.9	23.0	17.0	8.3	102.7	0.09	0.57

In summary, during Event 1, a local non-stationarity of the wind flow causes a strong non-stationarity of the response, with few large vibration cycles. During Event 2, a stationary wind flow produces an almost stationary response. Even if the mean and peak wind velocities of the two events are quite similar, the resulting response parameters in Event 1 are larger than in Event 2, both in mean and peak values.

The maximum strain corresponds to a peak stress value of 32 MPa in Event 1, of 22 MPa in Event 2. These values are widely lower than the yield strength of the material and are therefore well below the ultimate resistance.

5.5.3. Critical details and fatigue resistance

Fatigue is a local and progressive damage phenomenon, originating in critical structural points, referred to as critical details, where large local stresses arise, due to force distribution, geometrical features and local effects of welded and bolted joints.

The first step of the fatigue analysis is addressed to the identification of critical details and quantification of their fatigue resistance. Limiting the investigation to the shaft (the present study does not investigate the rotor components), details that are subject to local peak stress conditions are identified by a local FEM model of its lower part. The model has been built using hexahedral solid elements, reproducing the tubular pole with front opening, stiffeners, welded base plate with anchor bolts, considered as clamped at the base (Figure 5.21a).

To highlight the regions characterized by peak stress, a control horizontal displacement and a flexural rotation are applied at the top section of the FEM model, simulating stress condition induced by the flexural loading typical of wind.

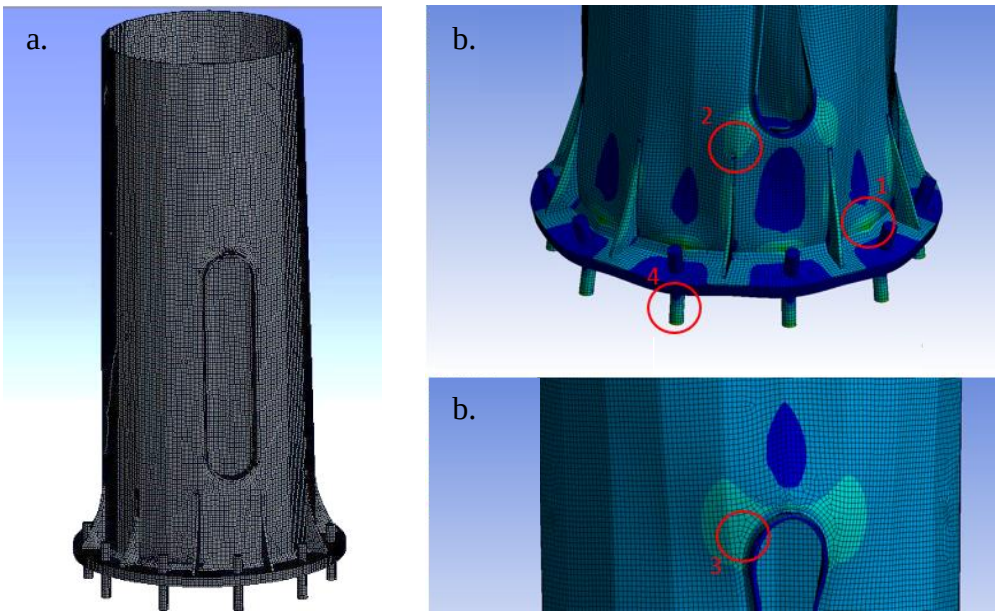

Figure 5.21. 3D local model (a) and stress representation with hot spot identification (b)

The following critical details are identified (Figure 5.21b):

- Joint 1: Welding joint between the base plate and the polygonal turbine tower, in the corner of the shell;

- Joint 2: Welding joint of the base plate, at top of stiffening ribs;
- Joint 3: Fillet welding joint around the opening;
- Joint 4: Anchor bolts of the base plate.

Among these, joints 1-3 are very typical of tubular supporting structures and have been the location of many detected damages and collapses (Caracoglia & Jones, 2006, Counsell et al., 2009, Simonović et al., 2008, Repetto & Solari, 2010, Repetto & Pagnini, 2017). Joint 4 is quite unusual and technically incorrect, because the gap between the foundation and the base plate, usually filled with mortar according to a proper execution mode, here it is left empty. Consequently, long and free anchor bolts are improperly subjected to flexural behavior that might be unsafe. Since structural details of this type should be avoided, Joint 4, even if critical, is not considered of general interest and it is not examined in the analyses that follow.

In accordance with the procedures usually adopted in standards and codes, the nominal stress approach characterizes the fatigue resistance of the critical joints by suitable S-N curves, representing the number of cycles, N, that leads to collapse under a stress time history of constant nominal stress range, S. International standards, such as Eurocode (EN 1993 1-9, 2005), International Institute of Welding (IIW) recommendations (Hobbacher, 2016), provide reference S-N curves for typical structural details, whose identifier value, FAT_{ref}, corresponds to the nominal stress range value (in MPa) producing fatigue collapse at $N=10^6$ cycles. Uncertainties in the choice of the appropriate S-N curve may lead to large spread over fatigue damage evaluation (Pagnini & Repetto, 2012).

Regretfully, due to the large variability of the existing structural joints, provisions do not cover all possible details. Therefore, when the reference structural details reported in guidelines do not meet the actual conditions, more refined methods should be applied. Among them, the Structural Hot Spot Stress (HSS) approach (Niemi et al., 2003) applies to welded joints to take into account geometric effects. The HSS value, s_{HS}, depends on the dimensional and loading properties of the component near the joint and includes all stress raising effects due to local geometric features of a structural detail, except those due to the local weld toe geometry. In this way, the non-linear peak stress caused by the local notch is excluded from the HSS (Figure 5.22).

The geometric stress is determined following the recent revision of the IIW recommendations on fatigue of welded components (Hobbacher, 2016). Accordingly, the HSS value is obtained by linear interpolation of the stress evaluated by the FEM model near the joints. The general expression is:

$$s_{HS} = a_1 \cdot s(p_1) + a_2 \cdot s(p_2) + a_3 \cdot s(p_3) \tag{5.16}$$

where $s(p_1)$, $s(p_2)$ and $s(p_3)$ are the stress value s evaluated at reference points p_1, p_2, p_3 in the vicinity of the joints; a_1, a_2 and a_3 are numerical coefficients, depending on the mesh characterization.

For FEM models with coarse mesh, characterized by element length greater than 0.4 t, where t is the plate thickness, a_1=1.5, a_2=-0.5, a_3=0; p_1 and p_2 are taken at a distance of 0.5 t and 1.5 t from weld toe, respectively.

For FEM models with fine mesh characterized by element length not larger than 0.4 t and pronounced non-linear stress increase towards the hot spot, a_1=2.52, a_2= -2.24, a_3=0.72; p_1, p_2 and p_3 are taken at 0.4 t, 0.9 t and 1.4 t from weld toe, respectively.

For FEM models with fine mesh characterized by element length not larger than 0.4 t, and moderate non-linear stress increase towards the hot spot, a_1=1.67, a_2= - 0.67, a_3=0; p_1 and p_2 are taken at 0.4 t and 1t from weld toe, respectively. This is the case adopted in the present work (Figure 5.22).

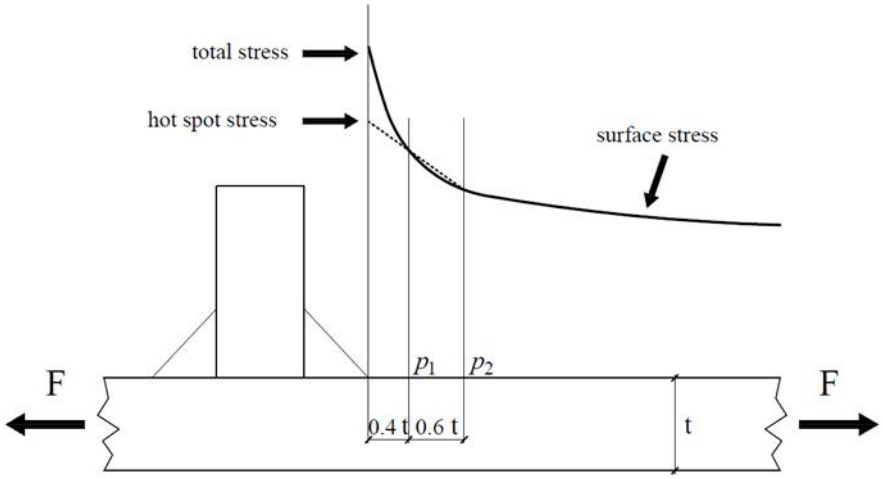

Figure 5.22. Definition of the structural hot spot stress adopted in the present work.

The HSS can be used to compute the actual FAT category of a structural joint, so that the nominal stress approach can be applied correctly.

The S-N curve of the joint under investigation, FAT_{assess}, can be calculated starting from a similar joint whose S-N curve, FAT_{ref}, is known. The procedure proposed by IIW requires the following steps:

1. select a reference detail, with known fatigue resistance FAT_{ref} , which is as similar as possible to the detail to be assessed, in terms of geometric and loading parameters;
2. establish a finite element model of the reference detail and of the detail to be assessed, adopting the same type of mesh according to the recommendations about FEM procedure to calculate HSS;
3. load the two FEM models according to the loading condition coherent with the reference curve definition;
4. estimate the HSS in reference and assessed detail models, $s_{HS,ref}$ and $s_{HS,assess}$ adopting Eq. (5.16) ;
5. calculate the fatigue class FAT_{assess} from FAT_{ref} as:

$$FAT_{assess} = \frac{s_{HS,ref}}{s_{HS,assess}} FAT_{ref} \tag{5.17}$$

Following this procedure, Table 5.3 synthetizes the results, reporting, for Joints 1-3, the reference fatigue curve class, FAT_{ref}, the FEM model of the reference detail together with the obtained value of $s_{HS,ref}$, the FEM model of the detail to be assessed together with the obtained value of $s_{HS,assess}$ and the fatigue curve class, FAT_{assess}.

Table 5.3. Resistance fatigue class (*FAT*) assessment for the three considered critical joints.

Joint	1	2	3
		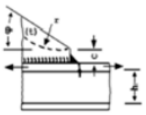	
FAT_{ref} (MPa)	40	71	63
	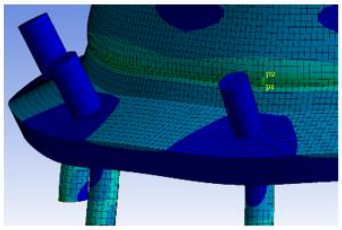	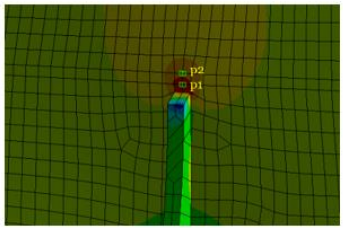	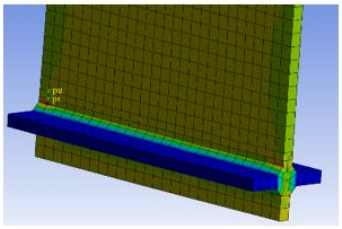
$s_{HS,ref}$ (MPa)	2.37	0.88	0.51
	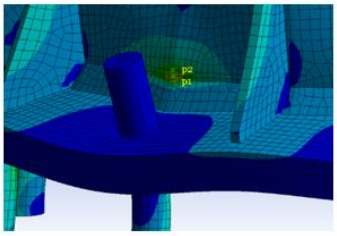	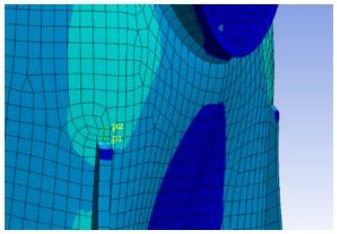	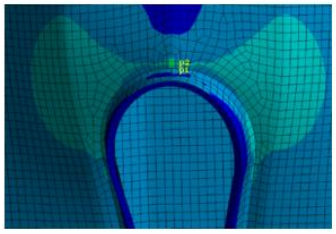
$s_{HS,assess}$ (MPa)	2.92	1.14	1.13
FAT_{assess} (MPa)	32	55	29

Figure 5.23 shows the reference and assessed fatigue resistance curves for the three critical joints together with the family of reference S-N curves proposed by Eurocode 3 (EN 1993 1-9, 2005). In particular, Joint 1 falls from FAT_{ref} = 40 to FAT_{assess}= 32, Joint 2 from FAT_{ref} = 71 to FAT_{assess} = 55 and Joint 3 from FAT_{ref} = 63 to FAT_{assess} = 29, showing that the resistance of the details considered is strongly reduced by the geometrical features. Consequently, Joints 1 and 3 fall under the lower fatigue curve proposed by Eurocode and IIW (*FAT* = 36). Such a serious reduction calls for further experimental analysis of this kind of joints, especially for Joint 1, which is extremely common in wind turbine supports and other widespread poles and towers. The greatest reduction is observed for Joint 3, for which the reference detail is quite different from the actual one, causing large uncertainties in the numerical evaluation of the final assessment.

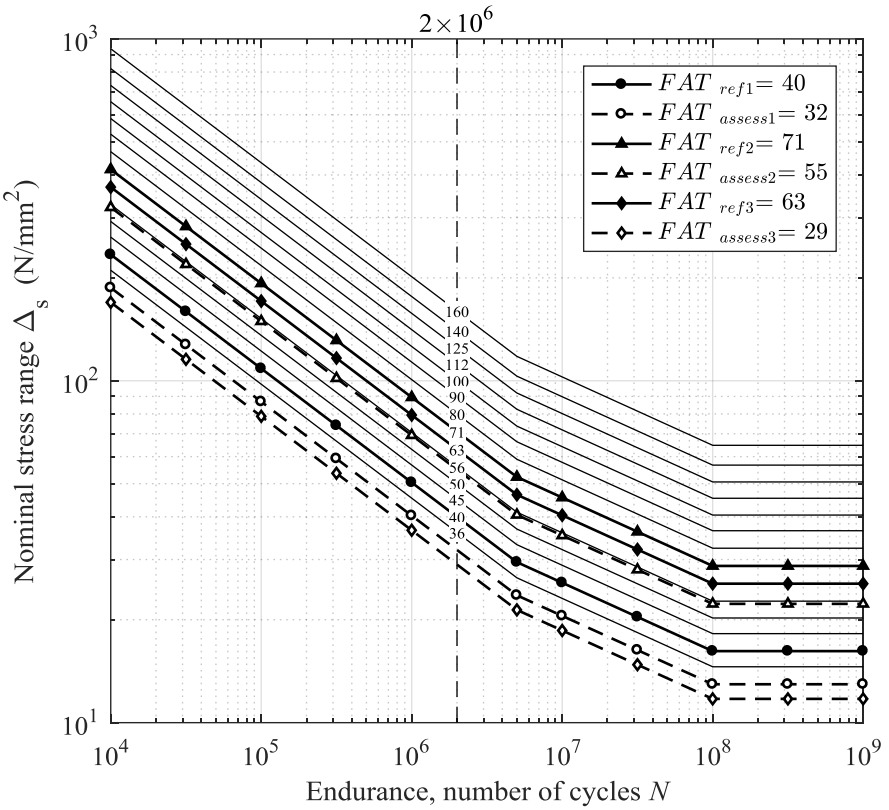

Figure 5.23. Resistance fatigue curve for the three considered critical joints.

5.5.4. Fatigue analysis

5.5.4.1 Fatigue damage evaluation

Fatigue damage on the three critical welded joints is investigated considering the two events described in section 5.6.2.

Starting from nominal stress time-histories, obtained multiplying the measured strain by the Young's modulus of steel, the load cycle histograms are obtained by applying the Rainflow cycle counting (Endo et al., 1967); the mean stress is accounted for by the Goodman relationship (Goodman, 1919). It results however negligible in the investigated case.

Figure 5.24 shows the load cycle histograms at the base of the turbine for the two events (red and grey lines), reporting the number of cycles in Log-Log scale, on varying the nominal stress amplitude. The histogram shows a decreasing trend, with a very large number of small amplitude cycles and small number of large amplitude cycles. In particular, for Event 1 (red line in Figure 5.24), some very large cycles occur when the turbine stops.

The fraction of damage induced by each block of cycles has been evaluated adopting the Palmgreen-Miner rule:

$$d_i = \frac{n(\Delta s_i)}{N(\Delta s_i)} \tag{5.18}$$

where $n(\Delta s_i)$ is the number of the cycles counted by the Rainflow algorithm with Δs_i nominal stress amplitude and $N(\Delta s_i)$ is the corresponding number of cycles to failure obtained from the resistance

curve. For each critical joint, it has been assessed adopting two different S-N curves that correspond, respectively, to the reference and the assessed *FAT* obtained with the HSS approach.

Figures 5.24 shows the adopted fatigue resistance curves superimposed to the cycle histograms. The horizontal lines represent the fatigue cut-off limit, i.e., the amplitude stress value below which stress cycles cannot produce damage. As this threshold is a function of the fatigue resistance, the *FAT* reduction causes a greater number of load cycles to be considered in the damage calculation.

Figures 5.25, 5.26 show the damage histograms for Events 1 and 2, respectively, for each critical joints and for the two values FAT_{ref} and FAT_{assess}. The damage histograms (grey solid bars) are represented in Log scale, on varying the amplitude of cycles in linear scale, superimposed to the cycle histogram (light gray empty bars). It is worth noting that the distribution of damage is strongly nonlinear with respect to stress amplitudes. The many cycles below the cut-off limit of the fatigue S-N curve (vertical dashed line in each diagram) do not produce structural damage. The cycles with amplitude greater than the cut-off limit induce a fatigue damage fraction proportional to the amplitude raised to the correspondent slope of the fatigue S-N curve.

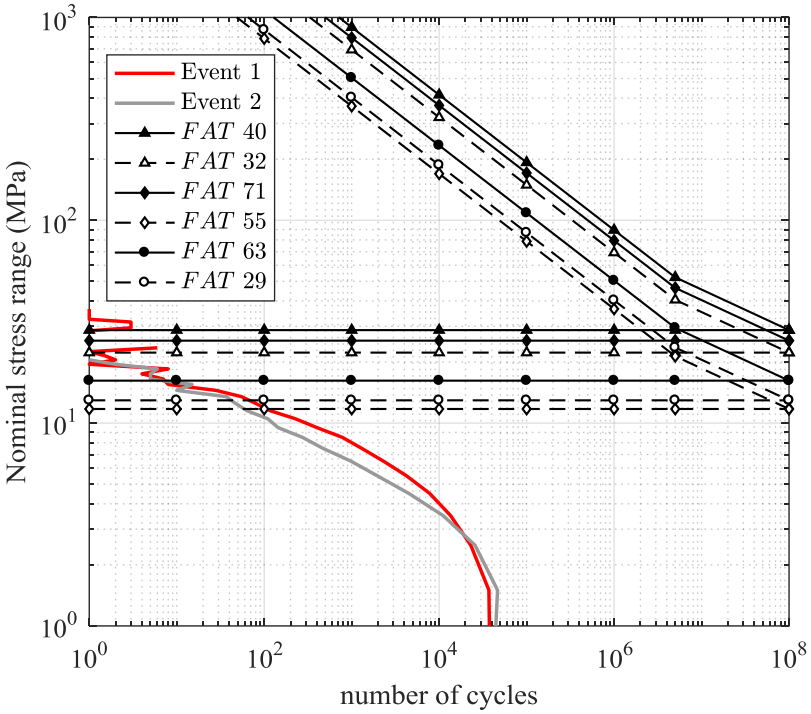

Figure 5.24. Load cycle histogram of Event 1 and Event 2 and related S-N curves for the critical joints.

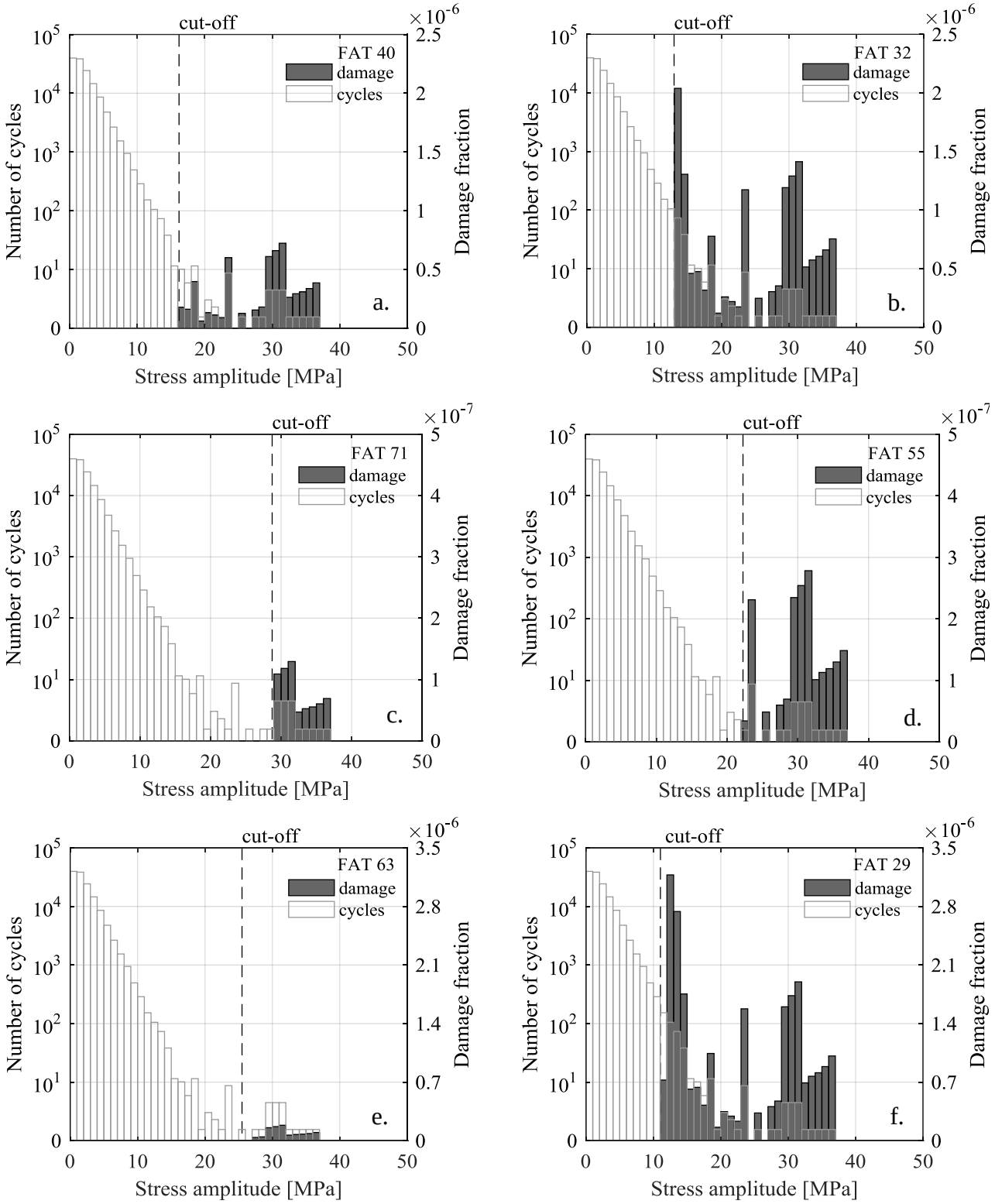

Figure 5.25. Wind induced fatigue damage during Event 1 in the critical Joint 1 (a,b), Joint 2 (c,d), Joint 3 (e,f)

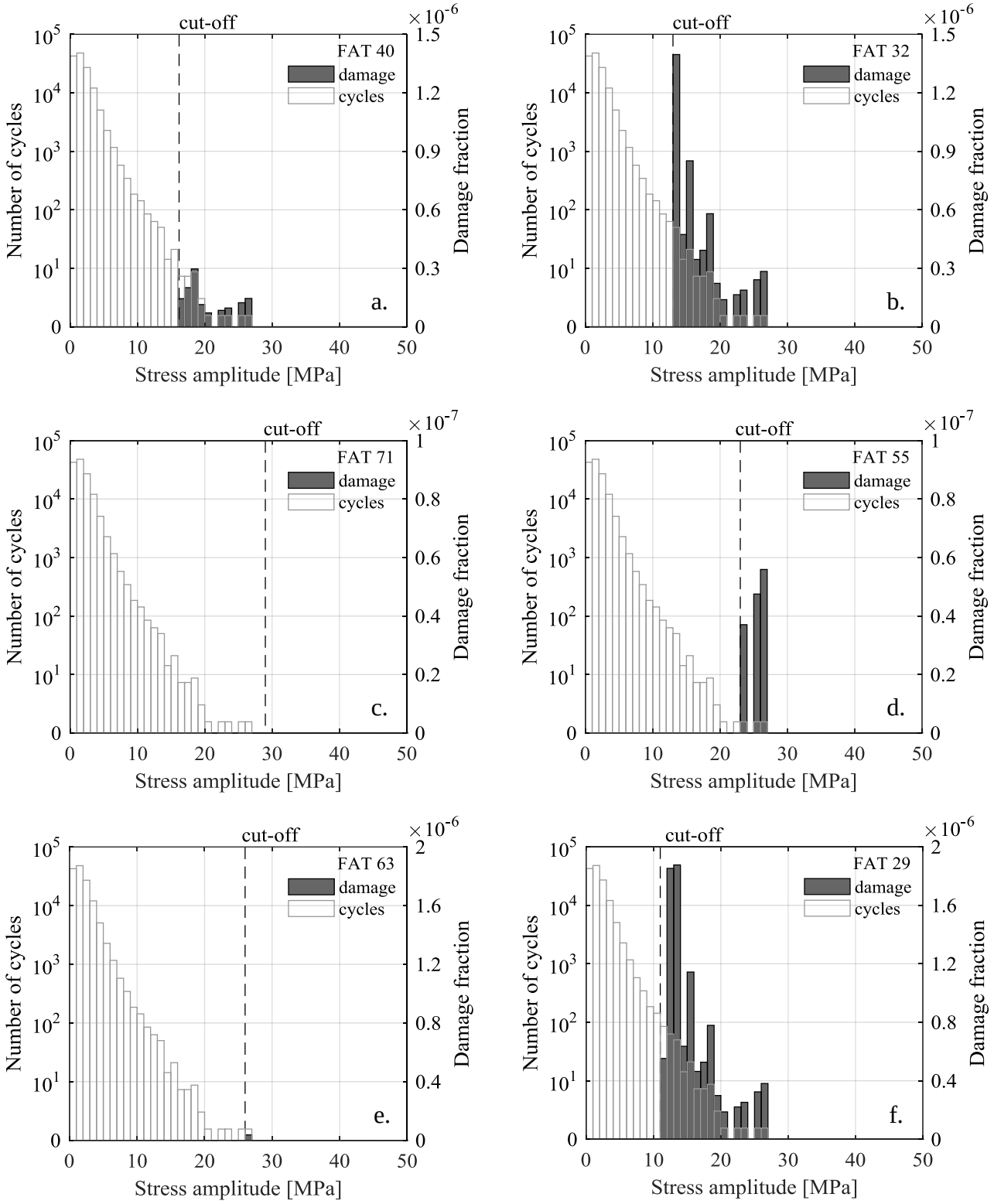

Figure 5.26. Wind induced fatigue damage during Event 2 in the critical Joint 1 (a,b), Joint 2 (c,d), Joint 3 (e,f)

Table 5.4. Accumulated fatigue damage D ($\times 10^{-5}$) in Joints 1-3 for Event 1 and Event 2.

D (10^{-5})	Joint 1			Joint 2			Joint 3		
	FAT_{ref}=40	FAT_{assess}=32	E(%)	FAT_{ref}=71	FAT_{assess}=55	E(%)	FAT_{ref}=63	FAT_{assess}=29	E(%)
Event 1	0.58	1.52	+162%	0.06	0.18	+200%	0.10	2.44	+2340%
Event 2	0.12	0.42	+250%	0	0.01	inf	0	0.75	Inf

Finally, the total damage accumulated during each event is evaluated using the linear damage accumulation law:

$$D = \sum_i d_i \tag{5.19}$$

Table 5.4 summarizes the daily fatigue damage, calculated for the two selected events, in the three considered Joints, with the reference and the assessed *FAT*; it also reports the error committed *E*, defined as:

$$E = \frac{D_{assess} - D_{ref}}{D_{ref}} \cdot 100 \tag{5.20}$$

where D_{ref} is evaluated using FAT_{ref}, D_{assess} is evaluated using FAT_{assess} S-N curves.

5.5.4.2 Effect of fatigue resistance

In both considered events, on decreasing the *FAT* category, the fatigue damage increases heavily (Figures 5.25, 5.26, Table 5.4). From the Hot Spot analysis, the estimated damage increases, for Event 1, by 162% for Joint 1, 200% for Joint 2, 2340% for Joint 3. For Event 2, damage increase is even more relevant, especially for Joints 2 and 3, for which the cycles are lower than the cut-off limit for the FAT_{ref} categories, partially higher for the FAT_{assess} categories (Figure 5.26 c/f). Assessment of Joint 3 is particularly critical, due to uncertainties in fatigue resistance. The use of the S-N curve related to *FAT*=29, as resulting from the HSS analysis, leads to the highest fatigue damage in the structure. Such results highlight, from one hand, the importance of a correct characterization of detail category of the joints and, from the other, the strong improvement in fatigue life from a careful detail design and manufacturing (Hobbacher, 2016). In these regards, experimental fatigue resistance analysis of the most common structural joints of turbines would lead to great benefits for economic and safe design.

5.5.4.3 Role of non-stationarity

Despite the two events described in section 5.6.2 are characterized by very close average wind speeds (see $\bar{u}$ in Table 5.2), the non-stationary nature of the first event, together with the effects induced by the sudden stop and the restart of the turbine, make the structural response very different from the second event. As shown in Table 5.4, marked differences can be found in the fatigue behavior and accumulated damage.

Concerning Event 1, the small number of large cycles due to turbine stop and start-up strongly affects the overall fatigue damage. By way of example, cycles with amplitude greater than 25 MPa constitute the 0.13‰ of the total and give rise to 44%, 52%, 85% of damage in Joint 3, 1, and 2, respectively (Figure 5.24, Table 5.4).

Stress cycles during Event 2 show a larger number of small amplitude cycles and a smaller number of large cycles, with respect to Event 1. Even in this case, due to damage non-linearity, the few large cycles are responsible of the induced damage, which is however significantly lower than the one obtained in Event 1 for any joints. In this case, cycles with amplitude greater than 25 MPa constitute the 0.02‰ of the total and give rise to 7%, 10%, 74% of damage in Joint 3, 1, and 2, respectively (Figure 5.24, Table 5.4).

5.5.4.4 Role of time-length

The variability of wind loading on structures is usually modelled by defining a series of wind loading conditions, each of them associated to a fixed incoming mean wind velocity. At the design stage, wind-induced fatigue damage associated to different loading conditions is usually computed over simulated or measured stationary stress time-histories of time length T_{th} between 10-min and 1 hour. Taken one stress time-history with length T_{th} associated to a given loading condition *lc*, the Rainflow counting is applied over T_{th}. The fraction of computed damage, $d_{th,lc}$ calculated for the time-history, is considered as representative of the whole loading condition. The total damage is then computed extrapolating the damage to the whole structural life, *T*, adopting the linear damage rule (Eq. 5.19) in the form (Repetto & Torrielli, 2017):

$$D(T) = \sum_{lc} d_{th,lc} \frac{T}{T_{th}} P_{lc} \tag{5.21}$$

where P_{lc} is the probability of occurrence of the loading condition *lc*; the value $T \times P_{lc}$ represents the effective time length of the loading condition *lc* in the whole structural life, *T*; the value $\Pi_{th,lc}=(T/T_{th})P_{lc}$ represents the number of time-histories of time length T_{th} corresponding to the effective time length of the loading condition *lc*. Such approach, referred to as 'state approach', can induce uncertainties over the final result, mainly due to two different reasons:

1) since 10 min – 1 h periods fall in the spectral gap of wind speed spectrum, the corresponding stress time histories could not include the fluctuations associated to the wind macro-meteorological peaks, representing daily, monthly, seasonal and annual fluctuations. These fluctuations, although responsible of few cycles, could become significant in the calculation of the fatigue life;

2) due to the randomness of wind loading and structural behavior, the conventional use of 10 min – 1 h load time history can be poor for a reliable estimate of fatigue damage. According to Eq. (5.21), the uncertainty connected with a single loading condition may propagate over the whole damage assessment, giving rise to possible overestimates or underestimates of the fatigue life. The uncertainties in the evaluation of $d_{th,lc}$ propagate into the total damage proportionally to $\Pi_{th,lc}$, which, on turn, depends on the effective time length of the operational condition *lc* and the time length T_{th}.

In order to analyze effect 1), the nominal stress time-history of Event 1 and 2 has been divided into time intervals of time length T_{th} (Figure 5.27). For each considered T_{th}, namely 1 day (whole event), 1 hour and 10 minutes, the Rainflow counting has been applied to every interval composing the event, and the total damage of the event has been obtained as the sum of the damages of its subparts. FAT=32 has been chosen as fatigue resistance. Table 5.4 summarizes the results, reporting also the error committed *E*, evaluated coherently with Eq. (5.20), where D_{ref} is evaluated using T_{th}=10 min, D_{assess} is evaluated using T_{th}=1 hour – 1 day time length intervals, respectively.

It is worth noting that the damage increases with the increasing of T_{th}. In particular, for Event 1, the values obtained using 10 minutes and 1 hour time intervals are almost the same (+7%); the value for

1 day is significantly higher (+ 253%). In this case, additional low-frequency large cycles are detected by the Rainflow evaluation only considering the whole events. Such effect, already detected in (Repetto & Torrielli, 2017) for stationary events, is here amplified due to the non-stationarity of the stress time-history. Considering Event 2, the increment of the damage with T_{th} is smaller because of the stationarity of the stress process, which includes few low-frequency cycles. However, an increment of about 38% is obtained considering T_{th}=1 hour, and of about 45% when T_{th}=1 day. Under this point of view, the common approach based on T_{th}=10-minute time-history may result under-conservative.

In order to analyze effect 2), the daily damage detected for the two considered events has been elaborated adopting a normalized representation already introduced by Sutherland (1999), Repetto & Torrielli (2017). Figure 5.28 shows the damage detected in Event 1 (a) and Event 2 (b) against the number of 10-minute segments used for the evaluation (herein referred as damage trajectories), normalized with respect to the "real" damage of the Event, computed considering the whole event time-history (i.e. the total number of 10-minute segments). The unity corresponds the correct damage estimation. For each event, the normalized damage trajectories have been obtained by the following procedure. For a given number of 10-minute segments, the average damage $d_{th,lc}$ of the considered set is computed; then, coherently with Eq. (5.21), the damage of the event has been extrapolated by multiplying the average damage $d_{th,lc}$ by the total number of 10-min segments that characterize the event. The sequential count (black dots) considers the 10-min segments in their chronological order, while the upper and lower bounds (grey dotted and dashed lines, respectively) are obtained considering sequential 10-min segments sorted according to the magnitude of their relative damage in descending and ascending order, respectively.

The sequential count trajectory shows the accuracy in the estimate of the mean damage as a function of the number of 10-min segments in the stress time series in its current shape. The upper and lower bounds quantify the maximum value of the over/under-estimation.

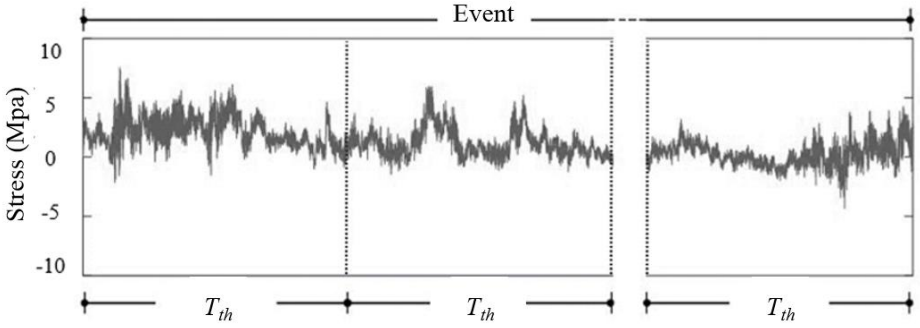

Figure 5.27. Partition of the event in T_{th} time length intervals.

Table 5.4. Daily fatigue damage in Joints 1 for different subdivision method

	Daily damage (10^{-5})				
	10 min	1 hour	*E* (%)	1 day	*E* (%)
Event 1	0.43	0.46	+7%	1.52	+253%
Event 2	0.29	0.40	+38%	0.42	+45%

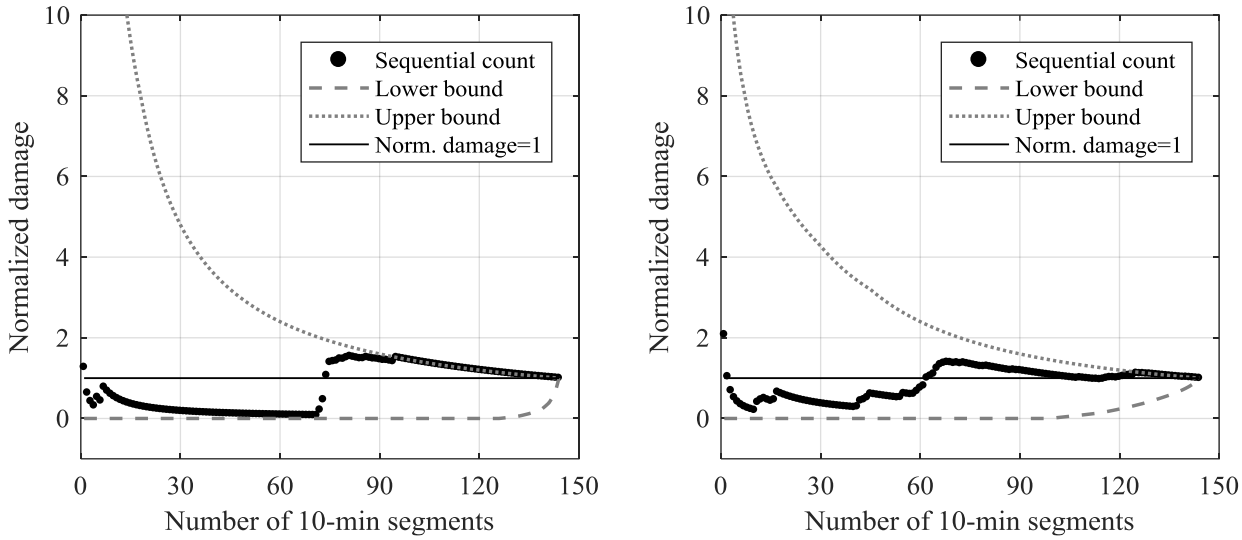

Figure 5.28. Normalized damage trajectories related to Event 1 (a) and Event 2 (b).

In each diagram, all three plots converge to the correct damage estimation of the event on growing the number of the segments adopted. The sequential trajectory leads to estimates with errors in the range (-92%) to (54%) and generally shows a non-monotonic trend, so that it is not possible to determine a priori if the analysis based on a limited number of 10 min segments leads to an under- or overestimate of the actual damage. The lower/upper bounds put in evidence errors of orders of magnitude, when only the less/more damaging 10-minute interval is considered as representative of the entire event. With regard to Event 1, the daily damage is almost completely concentrated in a precise instant, corresponding to the turbine stop, where the diagram exhibits a jump in the sequential count. As a consequence, the upper bound increases dramatically. Concerning Event 2, due to the almost stationary characteristic of the loading conditions, a quite random trend of the sequential count and less critical value of the upper/lower damage bounds are observed, even still quite large.

Such results call for a revision of the current fatigue procedure, aimed at a more refined definition of the load cases and of the corresponding time-history length to be considered for a reliable damage estimation (Agarwal & Manuel, 2009).

References

Abdalrahman, G., Melek, W., Lien, F.S. (2017). Pitch angle control for a small-scale Darrieus vertical axis wind turbine with straight blades (H-Type VAWT). Renew. Energy 114, 1353-1362.

Agarwal, P., Manuel, L. (2009). Simulation of offshore wind turbine response for long-term extreme load prediction. Eng. Struct. 31, 2236-2246.

Bajrić, A., Høgsberg, J., Rüdinger, F. (2018). Evaluation of damping estimates by automated Operational Modal Analysis for offshore wind turbine tower vibrations. Renew. Energy 116 (B), 153-163.

Battisti, L., Benini, E., Brighenti, A., Dell'Anna, S., Raciti Castelli, M. (2018). Small wind turbine effectiveness in the urban environment. Renew. Energy 129, 102-113.

Bir, G. S. (2010). User's guide to MBC3: Multi-blade coordinate transformation code for 3-bladed wind turbine. 1-24. UNLV Energy Collection.

Bogoevska, S., Spiridonakos, M., Chatzi, E., Dumova-Jovanoska, E., Höffer, R (2017). Data-driven diagnostic framework for wind turbine structures: a holistic approach. Sensors 17(4), 720.

Bracco, S., Delfino, F., Ferro, G., Pagnini, L.C., Robba, M., Rossi, M. (2018). Energy planning of sustainable districts: Towards the exploitation of small size intermittent renewables in urban areas. Appl. Energy 228, 2288–2297.

Bukala, J., Damaziak, K., Kroszczynski, K., Krzeszowiec, M., Malachowski, J. (2015). Investigation of parameters in fluencing the efficiency of small wind turbines. J. Wind Eng. Ind. Aerod. 146, 29-38.

Cao, Y., Zavala, V.M., D'Amato, F. (2018). Using stochastic programming and statistical extrapolation to mitigate long-term extreme loads in wind turbines. Appl. Energy 230, 1230-1241.

Capponi, L., Česnik, M., Slavič, J., Cianetti, F., Boltežar M. (2017). Non-stationarity index in vibration fatigue: theoretical and experimental research. Int. J. Fatigue 97, 9–19.

Caracoglia, L., Jones, N.P. (2006). Wind-induced failures of highway light poles during winter storms, ASME Pressure Vessels and Piping Division (Publication) PVP 9, 197-206.

Carne, T.G, Lobitz, D.W., Nord, A.R., Watson, R.A. (1982). Finite element analysis and modal testing of a rotating wind turbine. Technical Report SAND82-0345, UC-60, Sandia National Labs., Albuquerque, USA.

Castellani, F., Astolfi, D., Peppoloni, M., Natili, F., Buttà, D., Hirschl, A. (2019). Experimental vibration analysis of a small scale vertical wind energy system for residential use. Machines 7(2), 35.

Chen, J., Song, Y., Peng, Y., Nielsen, S.R.K., Zhang, Z. (2020). An efficient rotational sampling method of wind fields for wind turbine blade fatigue analysis. Renew. Energy 146, 2170-2187.

Cianetti, F., Palmieri, M., Slavič, J., Braccesi, C., Morettini, G. (2017). The effort of the dynamic simulation on the fatigue damage evaluation of flexible mechanical systems loaded by non-Gaussian and non stationary loads. Int. J. Fatigue 103, 60-72.

Counsell, S., Taplin, G., Thomas, M., Noyes-Brown, G. (2009). Fatigue analysis and repair of a high mast light pole. 7th Conf Austroads Bridg., Auckland, New Zeal., Melbourne, Victoria, 2009.

Danao, L.A., Eboibi, O., Howell, R. (2013). An experimental investigation into the influence of unsteady wind on the performance of a vertical axis wind turbine. Appl. Energy 107, 403–411.

EN 1991-1-4, 2005. Eurocode 1: Actions on Structures – Part 1.4: General Actions – Wind Actions. CEN, European Commitee for Standardization, Brussels, Belgium.

EN 1993-1·9, 2005. Eurocode 3: Design of steel structures -Part 1-9: Fatigue. CEN, European Commitee for Standardization, Brussels, Belgium.

Endo, T., Mitsunaga, K., Nacagawa, H. (1967). Fatigue of metals subject to varying stress-prediction of lives. Preliminary Proceedings if the Chugoku-Shikoku District Meeting, 1967, 41–44.

Evans, S.P., Bradney, D.R., Clausen, P.D. (2018). Assessing the IEC simplified fatigue load equations for small wind turbine blades: How simple is too simple? Renew. Energy 127, 24-31.

Evans, S.P., KC, A., Bradney, D.R., Urmee, T.P., Whale, J., Clausen, P.D. (2017). The suitability of the IEC 61400-2 wind model for small wind turbines operating in the built environment. Renew. Energy Environ. Sustain. 2, 31.

Gong, K., Chen, X. (2014). Influence of non-Gaussian wind characteristics on wind turbine extreme response. Eng. Struct. 59, 727–744.

Gong, K., Chen, X. (2015). Improved modeling of equivalent static loads on wind turbine towers. Wind Struct. 20 (5), 609-622.

Goodman, J., 1899. Mechanics Applied to Engineering, Longman, Green & Company, London.

GWEC, Global Wind Report Annual Market Update 2016, Global Wind Energy Council, Brussels, Belgium, 2016.

IEC 61400-12-1. (2005). Wind Turbines: Part 12.1-Power Performance Measurements of Electricity Producing Wind Turbines, International Electrotechnical Commission, Geneva, Switzerland.

IEC 61400-2. (2013) Wind Turbines: Small Wind Turbines. Geneva, Switzerland, International Electrotechnical Commission.

Hansen, M.H. (2007) Aeroelastic instability problems for wind turbines. Wind Energy 10, 551-577.

Hansen, M.O.L. (2015) Aerodynamics of Wind Turbines, Routledge, NY.

Hardesty, R.M., Korrel, J.A., Hall, F.F. (1981). Lidar measurement of wind velocity spectra encountered by a rotating turbine blade. NOAA Tech. Memo., Washington DC, USA.

Hau, E. (2013). Wind Turbines: Fundamentals, Technologies, Application, Economics, Springer-Verlag, Berlin, Germany.

Hobbacher, A. (2016) Recommendations for Fatigue Design of Welded Joints and Components. IIW doc. XIII-2460-13/XV-144013. Springer, Heidelberg, New York.

Hu, W.H., Thöns, S., Rohrmann, R.G., Said, S., Rücker, W. (2015a). Vibration-based structural health monitoring of a wind turbine system. Part I: resonance phenomenon. Eng. Struct. 89, 260-272.

Hu, W.H., Thöns, S., Rohrmann, R.G., Said, S., Rücker, W. (2015b). Vibration-based structural health monitoring of a wind turbine system. Part II: environmental/operational effects on dynamic properties, Eng. Struct. 89, 273-290.

Jang, Y.J., Choi, C.W., Lee, J.H., Kang, K.W. (2015). Development of fatigue life prediction method and effect of 10-minute mean wind speed distribution on fatigue life of small wind turbine composite blade. Renew. Energy 79, 187-198.

Jia, J. (2014). Investigations of a practical wind-induced fatigue calculation based on nonlinear time domain dynamic analysis and a full wind-directional scatter diagram. Ships Offshore Struct. 9, 272-296.

KC, A., Whale, J., Evans, S.P., Clausen, P.D. (2020). An investigation of the impact of wind speed and turbulence on small wind turbine operation and fatigue loads. Renew. Energy 146, 87-98.

KC, A., Whale, J., Urmee, T. (2019). Urban wind conditions and small wind turbines in the built environment: A review. Renew. Energy 131, 268-283.

Kijewski-Correa, T., Kwon, D.K., Kareem, A., Bentz, A., Guo, Y., Bobby, S., Abdelrazaq, A. (2013). SmartSync: An integrated real-time structural health monitoring and structural identification system for tall buildings. J. Struct. Eng. 139(10), 1675-1687.

Kosasih, B., Hudin H.S. (2016). Influence of inflow turbulence intensity on the performance of bare and diffuser-augmented micro wind turbine model. Renew. Energy, 87 154-167.

Kristensen, L., Frandsen, S. (1982). Model for power spectra of the blade of a wind turbine measured from the moving frame of reference. J. Wind Eng. Ind. Aerodyn. 10, 249–62.

Kwon, D.K., Kareem, A. (2019). Towards codification of thunderstorm/downburst using gust front factor: Model-based and data-driven perspectives. Eng. Struct. 199, 109608.

Kwon, D.K., Kareem, A., Butler, K. (2012). Gust-front loading effects on wind turbine tower systems. J. Wind Eng. Ind. Aerod. 104-106, 109-115.

Li, F., Wu, H., Wu, P. (2021). Vibration fatigue dynamic stress simulation under non-stationary state. Mech. Syst. Signal Pr. 146, 107006.

Liu, J., Lin, H., Zhang, J. (2019). Review on the technical perspectives and commercial viability of vertical axis wind turbines. Ocean. Eng. 182, 608–626.

Liu, X., Liang, S., Li, G., Godbole, A., Lu, C. (2020). An improved dynamic stall model and its effect on wind turbine fatigue load prediction. Renew. Energy 156, 117-130.

Lu, N.-Y., Hawbecker, P., Basu, S., Manuel, L. (2019). On wind turbine loads during thunderstorm downbursts in contrasting atmospheric stability regimes. Energies 12, 2773.

Lubitz, W.D. (2014). Impact of ambient turbulence on performance of a small wind turbine. Renew. Energy 61, 69-73.

Madsen, P.H., Frandsen, S. (1984). Wind-induced failure of wind turbines. Eng. Struct. 6(4), 281–287.

McLaren, K., Tullis, S., Ziada, S. (2012). Measurement of high solidity vertical axis wind turbine aerodynamic loads under high vibration response conditions. J. Fluids Struct. 32, 12-26.

Moan, T., Gao, Z., Ayala-Uragab, E. (2005). Uncertainty of wave-induced response of marine structures due to long-term variation of extratropical wave conditions. Mar. Struct. 18, 359–82.

Moriarty, P.J., Holley, W.E., Butterfield, S.P. (2004). Extrapolation of extreme and fatigue loads using probabilistic methods, Technical Report, NREL/TP-500-34421.

Mouzakis, F. Morfiadakis, E., Dellaportas, P. (1999). Fatigue loading parameter identification of a wind turbine operating in complex terrain. J. Wind Eng. Ind. Aerod. 82, 69-88.

Murtagh P., Basu B., Broderick B. (2005). Along-wind response of a wind turbine tower with blade coupling subjected to rotationally sampled wind loading. Eng. Struct. 27(8), 1209-19.

Nagai, B.M., Ameku, K., Roy, J.N. (2009). Performance of a 3 kW wind turbine generator with variable pitch control system. Appl. Energy 86, 1774-1782.

Niemi, E., Fricke, W., Maddox, S.J., 2018. Structural Hot-Spot Stress Approach to Fatigue Analysis of Welded Components - Designer's Guide. IIW International Institute of Welding, Springer, Singapore.

Oliveira, G., Magalhães, F., Cunha, Á., Caetano, E. (2018). Continuous dynamic monitoring of an onshore wind turbine. Eng. Struct. 164, 22-39.

Ozbek, M., Rixen, D.J. (2013). Operational modal analysis of a 2.5 MW wind turbine using optical measurement techniques and strain gauges. Wind Energy 16, 367-381.

Pagnini, L.C., Burlando, M, Repetto, M.P. (2015). Experimental power curve of small-size wind turbines in turbulent urban environment. Appl. Energy 154, 112-121.

Pagnini, L.C., Piccardo, G., Repetto, M.P. (2018). Full scale behavior of a small size vertical axis wind turbine. Renew. Energy 127, 41–55.

Pagnini, L.C., Repetto, M. P. (2012). The role of parameter uncertainties in the damage prediction of the alongwind-induced fatigue. J. Wind Eng. Ind. Aerod. 104–106, 227–238.

Palmieri, M., Česnik, M., Slavič, J., Cianetti, F., Boltežar, M. (2017). Non-gaussianity and non-stationarity in vibration fatigue. Int. J. Fatigue 97, 9–19.

Repetto, M.P., Pagnini, L.C. (2017). Fatigue life assessment of a vertical axis wind turbine. Proc. Int. Conf. on Wind Energy Harvesting, Winercost17, Coimbra.

Repetto, M.P., Solari, G. (2010). Wind-induced fatigue collapse of real slender structures. Eng. Struct. 32(12), 3888-3898.

Repetto, M.P., Torrielli, A. (2017). Long term simulation of wind-induced fatigue loadings. J. Wind Eng. Ind. Aerod. 132, 551-561.

Rezaeiha, A., Kalkman, I., Blocken, B. (2017). Effect of pitch angle on power performance and aerodynamics of a vertical axis wind turbine. Appl. Energy 197, 132-150.

Riziotis, A.V., Voutsinas, S.G. (2000). Fatigue loads on wind turbines of different control strategies operating in complex terrain. J. Wind Eng. Ind. Aerod. 85, 211-240.

Rolland, S.A., Thatcher, M., Newton, W., Williams, A.J., Croft, T.N., Gethin, D.T., Cross, M. (2013). Benchmark experiments for simulations of a vertical axis wind turbine. Appl. Energy 111, 1183-1194.

Rosenbrock, H.H. (1955). Vibration and stability problems in large turbines having hinged blades. Rep. C/T 113. Surry (Great Britain): ERA Technology Ltd.

Savaidis, G., Vormwald, M. (2000). Hot-spot stress evaluation of fatigue in welded structural connections supported by finite element analysis. Int. J. Fatigue 22(2), 85-91.

Shirzadeh, R., Devriendt, C., Bidakhvidi, M.A., Guillaume, P. (2013). Experimental and computational damping estimation of an off shore wind turbine on a monopole foundation. J. Wind Eng. Ind. Aerod. 120, 96-106.

Simonović, A.M., Stupar, S.N., Peković, O.M. (2008). Stress distribution as a cause of industrial steel chimney root section failure. FME Transactions 36(3), 119-125.

Solari, G., Pagnini, L.C. (1999). Gust buffeting and aeroelastic behaviour of poles and monotubolar towers. J. Fluids Struct. 13(7-8), 877-905.

Solari, G., Burlando, M., Repetto, M.P. (2020). Detection, simulation, modelling and loading of thunderstorm outflows to design wind-safer and cost-efficient structures. J. Wind Eng. Ind. Aerod. 200, 104142.

Solari, G., Repetto M.P., Burlando M., De Gaetano P., Pizzo M., Tizzi M., Parodi M. (2012). The wind forecast for safety management of port areas. J. Wind Eng. Ind. Aerod. 104–106, 266–77.

Staino, A., Basu, B. (2013). Dynamics and control of vibrations in wind turbines with variable rotor speed. Eng. Struct. 56, 58-67.

Sørensen, P. (2002). Wind models for simulation of power fluctuations from wind farms. J. Wind Eng. Ind. Aerodyn. 90, 1381–402.

Sutherland, H.J. (1999). On the fatigue analysis of wind turbines. SAND99-0089, Albuquerque (NM): Sandia National Laboratories.

Tabrizi, A.B., Whale, J., Lyons,T., Urmee, T., Peinke, J. (2017). Modelling the structural loading of a small wind turbine at a highly turbulent site via modifications to the Kaimal turbulence spectra. Renew. Energy 105, 288-300.

Thresher, R.W., Mirandy, L.P., Carne, T.G., Lobitz, D.W., James III, G.H. (2009). Structural dynamic behavior of wind turbines, in: D.A. Spera (Ed.), Wind Turbine Technology: Fundamental Concepts in Wind Turbine Engineering, American Society of Mechanical Engineers (ASME), New York, 605-662.

Tummala, A., Velamati, R.K., Sinha, D.K., Indraja, V., Hari Krishna, V. (2016). Review on small scale wind turbines, Renew. Sustain. Energy Rev. 56, 1351-1371.

Verkinderen, E., Imam, B. (2015). A simplified dynamic model for mast design of H Darrieus vertical axis wind turbines (VAWTs). Eng. Struct. 100, 564-576.

Wang Y., Lu W., Dai K., Yuan M., Chen S.-E. (2018). Dynamic Study of a Rooftop Vertical Axis Wind Turbine Tower Based on an Automated Vibration. Energies 11, 3135.

Wolfsteiner, P. (2017). Fatigue assessment of non-stationary random vibrations by using decomposition in Gaussian portions. Int. J. Mech. Sci. 127, 10–22.

Wood, D. (2011). Small Wind Turbines. Analysis, Design, and Application, Springer, London, UK.

Wright, A.K., Wood, D.H. (2004), The starting and low wind speed behavior of a small horizontal axis wind turbine. J. Wind Eng. Ind. Aerod. 92, 1265-1279.

Zhao, Y., Pan, J., Huang, Z., Miao, Y., Jiang, J., Wang, Z. (2020). Analysis of vibration monitoring data of an onshore wind turbine under different operational conditions. Eng. Struct. 220, 110071.

Zhou, H.F., Dou, H.Y., Qin, L.Z., Chen, Y., Ni, Y.Q., Ko, J.M. (2014). A review of full-scale structural testing of wind turbine blades. Renew. Sust. Energ. Rev. 33, 177-187.

6. Conclusions and perspectives

The present Ph.D. thesis has developed and applied a comprehensive structural-monitoring procedure tailored for the validation and the investigation in full-scale of the wind-induced response of vertical slender structures, with fixed and rotating masses.

Starting from a detailed review of the state of the art in the field of structural monitoring, and based on the experience gained during the Ph.D. activity in the experimental field, the present study has established a systematic and coded procedure to handle the long-term monitoring of vertical slender structures. In particular, the first main element of novelty is represented by an enhanced statistical characterization of the experimental database by including information of the stationarity of wind direction. In this way, data segments can be more accurately separated into homogeneous families to deal with them by models coherent with their physical reality. Moreover, a novel method has been developed to derive the structural displacements from a combination of accelerometric and strain measurements, based on the assumption of a structure vibrating only on its first bending mode. The application of the method to two real case studies has confirmed its validity for structures tending to point-like systems, such as light towers or wind turbines, which have a big lumped mass at the top. The suitability of this method to any vertical slender structure should be investigated.

The developed monitoring procedure has found practical application for two real structures: a light tower located in the operative area of the Harbor of La Spezia (Northern Italy), and a small vertical axis wind turbine installed on the quay of the Harbor of Savona (Northern Italy). The experimental activity has addressed several different issues. The main conclusions and perspectives of each main subject of the thesis are here reported.

Polygon Aerodynamics

The study of the hexadecagonal cross-section without ancillaries has proved that the lift, which is usually neglected for such sectional shapes, can be up to 40% of the drag for a particular angle of attack where the section is not symmetric (James, 1976). This result have a great impact both for the evaluation of the crosswind response and for the prediction of galloping instability. Doubling the corner radius, such effect is strongly mitigated. This result proves that lift force should be taken into account in the structural design of poles and towers, since such effect evanishes only in the contemporary presence of a high side number and a high corner radius.

The study of the effect of Reynolds number on the aerodynamic coefficients has confirmed the few results from literature (James, 1976, ESDU, 1980): both the crisis of the drag and the growth of Strouhal number have been observed in the critical Reynolds range. With regard to the lift coefficient, there are no references about its evolution in the critical range. The results have highlighted the high instability of the lift in the critical regime; this is significant of what can occur also in full-scale; even small perturbations (an obstacle, a tree, etc.) can affect the direction of the lift force. In the overall, it is timely to observe that, unfortunately, the Reynolds range covered in the experimental campaign is too low to describe the supercritical range. If possible, it would be interesting in the next future to conduct the investigation of the aerodynamic properties of polygonal cylinders at high *Re.*

The presence of the ancillaries can considerably affect the aerodynamic behavior. The welding is capable of increasing the drag at least of the 20%, while the lift can reach +- 0.8 for the most critical

flow direction. The results indicate that even little ledges can cause the lift to be comparable to the drag. The ladder has its main effect on the drag. When it is behind the shaft, it does not change the aerodynamic behaviour. When it is perpendicular to the flow, it greatly increases the exposed area, with a 60% increase of C_D. When it is upstream, it produces a sort of equivalent Reynolds effect, with a 35% reduction of the drag. It is thus difficult to predict the aerodynamic contribution of the ladder, which is able to modify deeply the loading even without changing the exposed area.

The evaluation of the galloping coefficient has highlighted the high sensitivity of the hexadecagonal section. No mean flow directions can be excluded from the possibility of galloping occurrence, since for every angle it exists a flow condition in which the necessary condition for the instability is met.

Perspectives of this study include dynamic tests to evaluate the response to vortex shedding and galloping, and angular non-stationary aerodynamic tests, to simulate the thunderstorm loading.

Dynamic identification

Under the guidance of the FEM outcomes, modal frequencies and mode shapes of the light tower have been identified. In particular, the results have shown the presence of several modes below 10 Hz involving torsional motions of the top platform. In addition, the frequencies of the first bending modes in the two principal directions have shown no perceivable variations as a function of the amplitude of oscillation.

The evaluation of damping ratios has been carried out for the first bending modes using OMA techniques in both frequency and time domain (Brincker and Ventura, 2015, Pagnini et al., 2018). Damping values turned out to be essentially made by the aerodynamic contribution, as the dissipative capacity is almost evanishing at the low wind velocities. The OMA techniques have been intersected with the estimation provided by the reference calculation model for comparison. For one principal direction (aligned with the ladder), the results have shown a very good agreement between measurements and predictions. In particular, both methods have detected the non-linear trend of damping due to the drag crisis in the critical Reynolds range; to the best of author's knowledge, no scientific works have ever reported such effect. In the orthogonal direction, the experimental values almost replicate what has been obtained for the other direction, despite the aerodynamic contribution of the ladder. The result points out a symmetric behavior of the structure as far as the aerodynamic contribution to damping is concerned. In the next phase of the research, additional techniques with different approaches will be used (Yuen, 2010) to improve the reliability of damping estimation.

Full-scale validation of the response

With regard to the light tower, the outcomes of the comparison between measured and calculated response have shown a small error of the reference calculation model. In particular, the model is able to predict excellently the mean alongwind response, while it slightly overestimates the maximum response at high velocities. The discrepancy between calculations and predictions increases as regards the crosswind response. However, as a further source of uncertainty, the lift derivative has been put to zero since no reliable quantification was obtained in the wind tunnel tests. In the overall, the results validate the goodness of the model for the considered structural typology. In particular, the validity of the engineering simplifications of the CFS is confirmed (Solari and Pagnini, 1999).

The analysis of parameter bias has proved that damping is the parameter that mostly spread uncertainties in the wind-induced response, being considerably underestimated by current standard

and codes. Such results highlight that a sound damping evaluation is crucial for the correct evaluation of the structural response. Moreover, disregarding the actual dissipative contribution of localized masses may lead to significant overestimate of the wind-induced actions and effects.

The calculation has been also applied for the small wind turbine in parked conditions, to assess the suitability of the model for the considered structural typology. A great variability of the measured response has been observed at a first glance. This effect can be possibly attributed to the different atmospheric stability between day and night, or to the non perfect polar-symmetry of the structure. However, in terms of averaged values, there is good agreement between measurements and predictions, with the discrepancy arising only at the highest velocities. In this respect, the next phase of the research will deal with the enhancement of the validation from a better separation of homogeneous wind events. In the overall, the comparison shows a predictable greater error with respect to the light tower. Indeed, the calculation model consider the localized masses as rigid and compact entities, while the rotor is flexible and distributed in space. However, considering the relevant uncertainties, the results look very promising for a generalization of the model to small wind turbines.

Rotation-induced modal properties

The first effect of rotation on the dynamic response that has been observed regards the harmonic content of wind loading. Peaks of the structural response have been observed at frequencies that are multiple of the rotational frequency. These peaks are due to the fact that the wind loading on the wind turbine is "sampled" by the rotation of the rotor; the resulting spectrum is known as rotationally sampled wind spectrum (Murtagh et al., 2005). No documented studies have reported how such phenomenon affects the harmonic loads specifically on vertical axis wind turbines, neither from a quantitative nor from a qualitative viewpoint. Therefore, as a perspective, a model of the rotor will be tested in the wind tunnel for a quantification of the relevant wind spectrum.

As a second effect of rotation, a splitting of the frequencies of the first mode (bending mode of the tower) and second mode (bending mode of the blade arms) has been observed. The effect on the blade mode is well documented in literature (Carne et al. 1982, Hansen 2007) and it is due to the fact that we are measuring in a fixed reference system (the one of the accelerometer) an effect of the vibration of a rotating component (the blade). Instead, the splitting of tower's bending mode is rarely dealt in literature (McLaren et al., 2012) where it is possibly attributed to the gyroscopic effect. The analytical formulation carried out in this study has confirmed that gyroscopic forces produce a splitting of the bending mode of the tower. In the next step, damping will be introduced and the formulation will be validated in full-scale. This represents the first step towards the generalization of the reference analytical model for fixed-masses systems (Solari and Pagnini, 1999) to rotating-masses systems, which remains as a perspective of the present work.

Fatigue assessment

The analysis of the structural response in both parked and rotating condition has shown a very complex behavior, due to site turbulence, rotor aerodynamic loading, stop and start conditions and to other non-stationary wind-induced phenomena. The most notable registered effect is the sudden increase of stress at the rotor start-up and at the rotor stop operated by the control system. Due to gusts, these situations happen usually at wind speeds lower than the theoretical cut-in and cut-out values, giving rise to very critical conditions for fatigue crack initiation and propagation.

Fatigue resistance of structural joints widely used in common applications is still uncertain, giving rise to huge variations in fatigue damage evaluations. Results obtained highlight, from one hand, the importance of a correct characterization of detail category of the joints in verification stages and, from the other, the strong improvement in fatigue performance of the turbine deriving from a careful detail design and manufacturing (Hobbacher, 2016). In these regards, experimental fatigue resistance analysis of the most common structural joints of turbines would lead to great benefits for economic and safe design.

Although the two events investigated are quite similar in terms of mean value and standard deviation of wind speed and response, the non-stationary event produces a small number of very large cycles that result in much greater fatigue damage with respect to the damage induced by the stationary one. As a matter of fact, few intense events can produce crack initiation and strongly reduce fatigue life of the turbine. This suggests the importance of including in the fatigue analysis a careful characterization of the load non-stationarity that can induce large stress in the turbine, due to rotor operational conditions, non-stationary incoming wind, such as thunderstorm phenomena and tornadoes (Lu et. al, 2019), thermal atmospheric stability (Repetto, 2011) or other exceptional events.

The daily fatigue damage associated to the two measured events has been used as a benchmark to compare the standard state approach analysis, which is usually adopted in design using simulated or measured stationary stress time-histories of time length between 10-min and 1 hour. The investigation highlights two main source of uncertainties. Firstly, 10 min – 1 h time histories cannot include large low-frequency fluctuations associated to the wind macro-meteorological peaks and to other non-stationary effects, leading to under conservative damage estimations, especially for the non-stationary event. Secondly, due to randomness of wind phenomenon and structural behavior, the use of 10 min – 1 h time history to represent a loading condition may lead to large uncertainties on the final damage assessment, when the fatigue estimated by few 10 min time histories is extrapolated to the whole wind loading. In this case, it is not possible to determine a priori if the analysis based on a limited number of 10 min segments leads to an under- or overestimate of the actual damage. The lower/upper bounds obtained put in evidence errors of orders of magnitude in damage estimation, when only the less/more damaging 10-minute interval is considered as representative of the entire event. Such a result calls for a revision of the current fatigue procedure, aimed at a more refined definition of the load cases and of the corresponding time-history length to be considered for a reliable damage estimation (Agarwal & Manuel, 2009).

In the overall, the results obtained by experimental and numerical analysis confirm the limits of current standard methods for small wind turbine design. Future work should be addressed to formulate standard procedures able to reproduce properly the complex wind turbine loading, response, resistance and cumulative damage.

Future developments

While these efforts lay the foundations for the development of the monitoring activity, the monitoring program will be enhanced by an expansion of the instrumentation suite and structures monitored.

In particular, a new light tower, 35 m high, will be monitored in the Harbor of Genoa, in close proximity of a LiDAR-Scanner, supplying a continuous reconstruction of the 3D wind field. In this respect, the full-scale measurements will be used to validate new calculation methods of the dynamic response to thunderstorm outflows.

Moreover, in the next months a reinforced concrete bridge will be monitored through the use of IoT sensors and 5G communication, supplying in real-time the structural health. In this way, the monitoring activity will address issues not included in the present work.

References

Agarwal, P., Manuel, L. (2009). Simulation of offshore wind turbine response for long-term extreme load prediction. Eng. Struct. 31, 2236-2246.

Brincker R., Ventura C. E. (2015). Introduction to operational modal analysis. John Wiley & Sons, Ltd.

Carne, T.G, Lobitz, D.W., Nord, A.R., Watson, R.A. (1982). Finite element analysis and modal testing of a rotating wind turbine. Technical Report SAND82-0345, UC-60, Sandia National Labs., Albuquerque, USA.

ESDU 79026 (1980). Mean fluid forces and moments on cylindrical structures: polygonal sections with rounded corners including elliptical shape. London, UK.

Hansen, M.H. (2007) Aeroelastic instability problems for wind turbines. Wind Energy 10, 551-577.

Hobbacher, A. (2016) Recommendations for Fatigue Design of Welded Joints and Components. IIW doc. XIII-2460-13/XV-144013. Springer, Heidelberg, New York.

James, W.D. Effects of Reynolds number and corner radius on two-dimensional flow around octagonal, dodecagonal and hexdecagonal cylinders, Ph.D.Dissertation, University of Iowa, 1976.

Lu, N.-Y., Hawbecker, P., Basu, S., Manuel, L. (2019). On wind turbine loads during thunderstorm downbursts in contrasting atmospheric stability regimes. Energies 12, 2773.

McLaren, K., Tullis, S., Ziada, S. (2012). Measurement of high solidity vertical axis wind turbine aerodynamic loads under high vibration response conditions. J. Fluids Struct. 32, 12-26.

Murtagh P., Basu B., Broderick B. (2005). Along-wind response of a wind turbine tower with blade coupling subjected to rotationally sampled wind loading. Eng. Struct. 27(8), 1209-19.

Pagnini, L.C., Piccardo, G., Repetto, M.P. (2018). Full-scale behavior of a small size vertical axis wind turbine. Renew. Energy, 127, 41–55.

Repetto, M.P. (2011). Neutral and non-neutral atmosphere: Probabilistic characterization and wind-induced response of structures. J. Wind Eng. Ind. Aerod. 99, 969–978.

Solari, G., Pagnini, L.C. (1999). Gust buffeting and aeroelastic behaviour of poles and monotubolar towers. J. Fluids Struct. 13(7-8), 877-905.

Yueng, K-V. (2010). Bayesian Methods for Structural Dynamics and Civil Engineering. John Wiley & Sons Ltd.

List of Acronyms

ADC	Analog to Digital Converter
CFD	Computational Fluid Dynamics
CFS	Closed-Form Solution
DOF	Degree Of Freedom
EFDD	Enhanced Frequency Domain Decomposition
ESF	Equivalent Static Force
FDD	Frequency Domain Decomposition
FEA	Finite Element Analysis
FEM	Finite Element Model
FTP	File Transfer Protocol
GEF	Gust Effect Factor
GGF	Generalized Gust Factor
GPS	Global Positioning System
GRF	Gust Response Factor
HAWT	Horizontal Axis Wind Turbine
IFT	Influence Factor Technique
LAN	Local Area Network
LCA	Load Controller Assembly
LDV	Laser Doppler Vibrometer
LRC	Load Response Correlation
MAC	Modal Assurance Criterion
MAPE	Mean Absolute Percentage Error
MEMS	Micro Electro Mechanical Systems
OMA	Operational Modal Analysis
PE	Percentage Error
PSD	Power Spectral Density
PV	Photo-Voltaic
SDOF	Single Degree Of Freedom
SHM	Structural Health Monitoring
SMT	Surface Mount Technology
TPS	Terrestrial Positioning System

UPS	Uninterruptable Power Supply
VAWT	Vertical Axis Wind Turbine
WT	Wind Tunnel

List of Symbols

a	acceleration
a_G	galloping coefficient
A_k	reference area of the *k-th* mass
A_{ref}	reference area of the model for wind tunnel tests
b	reference size of the cross-section
C_D	mean drag force coefficient
C_L	mean lift force coefficient
C'_D, C'_L	first angular derivatives of C_D, C_L
D	diameter of the cross-section or total damage
d	fraction of damage
FAT	fatigue resistance class
f_s	sampling frequency
f_v	Nyquist frequency
f_{sh}	vortex shedding frequency
f_T	turbulence factor
f_{comb}	frequency for combination of spectra
G_{10}, G_1, G_{60}	gust factor of U over 10 minutes, 1 minute, 60 minutes
G_x, G_y	gust response factor in x, y direction
g_x, g_x	peak coefficient of the response in x, y direction
h	height of the structure
I_{10}, I_{60}	turbulence intensity of U over 10 minutes, 60 minutes
I_u , I_v	turbulence intensity of u, v
I	mass moment of inertia
k_{10}, k_{60}	kurtosis of U over 10 minutes, 60 minutes
L_u , L_v	turbulence integral length scale of u, v

m_{x1}, m_{y1}	modal mass of the first vibration mode in the *xz*, *yz* plane
m	mass
n_{x1}, n_{y1}	frequency of the first vibration mode in the *xz*, *yz* plane
n_i	frequency of the *i-th* vibration mode
$\bar{o}$	time average of a general recorded quantity
P	rotational frequency
rpm	rotations per minute
r	corner radius of the cross-section
Re	Reynolds number
St	Strouhal number
$S_{\ddot{x}\ddot{x}}$	PSD of the recorded accelerations
S_{xx_acc}	PSD of the displacements derived from acceleration records
S_{xx_est}	PSD of the displacements derived from strain records
S_{xx_comb}	PSD of the combined displacements
s_{HS}	Hot Spot stress
T	time length or structural life
U	wind speed vector
$\bar{\mathbf{U}}$	mean wind speed vector
U'	turbulent fluctuation vector
U	magnitude of wind speed vector
$\bar{u}$	magnitude of mean wind speed vector
$\hat{U}$	1 second peak wind velocity
U_{m10}, U_{m60}	time average of U over 10 minutes, 60 minutes
U_{m1}	maximum mean wind velocity averaged over 1 minute
u, v, w	wind velocity components in the structural axes x, y and z
u_A, v_A, w_A	wind velocity components recorded in the anemometric axis (x_A, y_A and z_A)
u_*	shear velocity
z_0	roughness length
z_m	value of z below which $\bar{u}$ is taken as constant
α	direction of wind speed vector, or angle of attack of the flow
α_{m10}	mean wind direction over 10 minutes

γ_{10}, γ_{60}	skewness of U over 10 minutes, 60 minutes
δ_{x1}, δ_{y1}	logarithmic decrement of damping of the first vibration mode in the *xz*, *yz* plane
ξ_{x1}, ξ_{y1}	critical damping ratio of the first vibration mode in the *xz*, *yz* plane
ε	strain
Ω	rotational velocity
ρ	air density
$\sigma_{\alpha 10}$	standard deviation of wind direction over 10 minutes
υ_x, υ_y	expected frequency of the response in *x*, *y* direction
ψ_{x1}, ψ_{y1}	continuous mode shape of the first vibration mode in the *xz*, *yz* plane
ω	circular frequency